Signal processing for ground penetrating radar

Maida, Aminu Wada

Award date:
2007

Awarding institution:
University of Bath

Signal Processing for Ground Penetrating Radar

Aminu Wada Maida

A thesis submitted for the degree of Doctor of Philosophy

University of Bath

Department of Electrical & Electronic Engineering

April 2007

ProQuest LLC
789 East Eisenhower Parkway
P.O. Box 1346
Ann Arbor, MI 48106-1346

Acknowledgements

First and foremost I would like to thank the Almighty for his love and guidance and for the great opportunity he has given me in life to study at the University of Bath.

I would like to express my gratitude, to my supervisors Dr Stephen Pennock and Dr Peter Shepherd. The time and effort they have put into the project has helped steer me in the right direction. I would also like thank other members of staff in the Department of Electronic and Electrical Engineering for their support and time they spend making sure all students have the necessary resources to carry out their projects.

Also I would like to thank the Petroleum Technology Development Fund in Nigeria for their sponsorship. And lastly, I am grateful to my parents, family members and friends for their support, patience and sponsorship over the years.

Abstract

Ground penetrating radar (GPR) is a fast growing technology for remote sensing applications. GPR finds uses in various fields from engineering applications, to archaeology and forensic science.

The use of Frequency Modulated type GPR for buried utility line location presents a number of signal processing challenges due to the signal propagation environment. In particular the large bandwidth required for the resolution of closely located utility lines often leads to high material attenuation losses, leading to weak measured signals.

This thesis covers work carried out in developing a signal processing technique that deals with the unwanted side lobe problems encountered with Frequency Modulated GPR systems that use signal processing based on the Discrete Fourier Transform (DFT). The technique is based on superimposing and averaging multiple DFT analyses from the same data set. The technique aims to improve DFT signal analysis by reducing side lobe levels without broadening the main lobes hence maintaining resolution. Results from applying the technique to simulated GPR data have shown it to have the ability to detect targets otherwise undetectable through standard DFT analysis, at the same time providing significant side lobe reduction and minimal loss in resolution. In addition, the technique has been applied to experimental data from a representation of a GPR system and real Frequency Modulated GPR data, again showing improved target detection capabilities, minimal resolution loss, significant side lobe reduction and minimal error in position detection. The technique is also shown to have negligible computational requirements.

The thesis also contains a general review of GPR technology, including its history, various applications and the science behind its operation.

Chapter 1: Introduction

1.1 The Buried Utility Line Location Problem

Overhead utility lines are fast becoming a thing of the past especially in urban areas. Most utility lines are currently buried beneath our cities, making the urban underground an extensive network of utility lines which include phones, gas, electricity, water, cable TV, sewage pipes, street lighting, traffic signals, etc.

As cities grow, more construction is carried out, new utility lines are installed and existing ones maintained. This usually requires excavation in and around the vicinity of already existing buried utility lines, making them vulnerable to damage. Currently maps showing the layout of buried utility lines are often non-existent or inaccurate. This lack or inaccuracy, of information often leads to ruptured water pipes or severed electrical conduits with subsequent structural damage, disruption to daily life and commerce and in the worst case injury to personnel and bystanders. Over the years several costly accidents have occurred worldwide due to the inability to determine correctly the presence of already existing utility lines [1, 2]. The costs of damages, insurance and restoration when utility lines are damaged provide a powerful motivation for the development of technologies for buried utility line detection.

1.2 Existing Methods for Buried Utility Line Detection

There currently exist several methods of detecting buried utility lines that have been used with varying degrees of success. These methods generally fall into two categories; destructive methods and non-destructive methods. The destructive methods involve some form of planned and careful excavation in the vicinity where buried utility lines are thought to be present. However, there still exists a high degree of risk associated with a destructive

approach depending on the amount of information available prior to excavation. On the other hand, non-destructive methods, also known as geophysical methods, measure the ground response from introducing a wave/signal into the ground and/or utilize a physical property of the buried object that is different from the surrounding ground. Table 1.1 summarises a few geophysical methods for detecting buried objects.

Method	Mode of Operation	Disadvantages
Seismic	Vibrations introduced into ground typically via explosives	Safety issues using explosives. Explosions can be very loud
Nuclear	Radiation e.g. gamma rays introduced into ground	Use of hazardous material
Thermo graphic	Measurement of Temperature field variation	Can only detect utility lines that affect ground temperature e.g. steam pipes
Electromagnetic	Electromagnetic waves introduced into the ground using antennas	Possible interference from other radio equipment such as mobile phones. Measured response can be very weak in certain conditions

Table 1.1 Non-destructive methods for detecting buried utility lines

Of all the methods listed in Table 1.1 the Electromagnetic method otherwise known as Ground Penetrating Radar (GPR) is the most attractive method and has been the most favoured method for utility line detection. Ground Penetrating Radar refers to a range of electromagnetic techniques used for the detection of objects beneath or within an opaque structure. Development of GPR systems for utility line detection started in the early 70's. One of the first of such GPR systems was the Terrascan designed by the Ohio State University in collaboration with Columbia Gas System Service Corporation and Microwave Associates [3]. Subsequently, over the years a lot of research has been carried out into the use of GPR for detecting buried utility lines [4-7].

GPR for utility line detection has two major drawbacks. The first (as mentioned in Table 1.1) is that the measured response is often weak in certain propagation media, which leads to difficulty in signal analysis. The second limitation concerns the density of the utility lines in urban areas. The highly dense and extensive network of utility lines often makes it difficult to clearly image the utility lines. Also, another issue concerning the use of GPR is the fact that as a radio wave emitter, GPR is subject to licensing and control [8]. The signal analysis problem in GPR systems due to weak measured responses in a dense network of utility lines is the general problem area this research project aims to address.

1.3 Aims of Research

Typically utility lines are buried within a metre or two of the surface with a wide variation of sizes and can be metallic or non-metallic. The common feature of all utility lines is that they are long and cylindrical which can be used as an advantage in GPR system design. Also, as mentioned earlier, the utility lines tend to occur in a dense and extensive network, which means the detection method requires a high resolution capability to detect and resolve the often closely located utility lines.

This research project addresses the resolution and detection limitations encountered by Frequency Modulated Continuous Waveform (FMCW) GPR systems that rely on the Discrete Fourier Transform (DFT) signal analysis. The aim was to develop a novel and improved signal processing routine that will improve DFT-based signal analysis for FMCW GPR systems by reducing side lobe levels in the DFT spectrum with minimal loss in resolution.

1.4 Report Outline

This report contains work carried for the entire duration of the project, consisting of an extensive literature survey on the field of GPR systems, electromagnetic wave propagation and signal processing for FMCW GPR systems. The report also contains the theory and

discussion on a novel signal processing technique as well as results from applying the technique to simulated and measured data.

The layout of the report is as follows; in this chapter the background to the problem of buried utility line location has been introduced and some approaches to locating buried utility lines have been presented with their limitations highlighted. In Chapter 2 a general overview of the field of GPR is presented. The various applications and types of GPR systems are presented as well as the science behind GPR operation. In Chapter 3 the theory of FMCW GPR operation is presented along with some commonly used signal processing techniques for beat spectrum analysis in FMCW systems. Chapter 4 contains the theory behind a novel signal processing technique developed for FMCW beat spectrum analysis. In Chapter 5 results from applying the novel signal processing technique to measured and simulated data are presented and discussed. Finally Chapter 6 concludes the report and is followed by a list of referenced documents and appendices. Each of the chapters end with a brief conclusion of the material covered in it. In addition, conference papers presented as a result of this research project are contained in the appendices

Chapter 2: Overview of Ground Penetrating Radar

2.1 Ground Penetrating Radar History and Uses

Ground Penetrating Radar (GPR) refers to a range of electromagnetic techniques used for the detection of objects beneath the Earth's surface or within an opaque structure. GPR uses electromagnetic fields to probe lossy dielectric material such as soil. Changes in the materials electrical properties cause a reflection of the propagating electromagnetic wave. These changes can be at the boundary between layers of dielectric material or between dielectric material and buried objects.

A history of GPR as a technique for buried object detection is given in [9] , whereas a history of the major developments in the product life cycle of GPR systems is given in [10]. The first attempt at using electromagnetic waves to probe the ground occurred at the beginning of the 20^{th} century in Germany [11]. Six years later patents by Loeimbach and Lowy [12, 13] describe the first use of electromagnetic signals to locate a buried object. However, it was not until over half a century later that GPR systems became commercially available. In 1974 Geophysical Survey Systems Inc was formed becoming the first company to manufacture GPR systems for commercial sales [14]. Today several companies manufacture a wide range of GPR systems and related products for various applications (see [15]).

The development of GPR technology is driven by it applications. A GPR system is built depending on the needs of its application. The system's range of operating frequency, antenna type and modulation scheme depend on a number of factors including the

requirements of depth penetration and resolution, available signal processing hardware/software, shape and size of targets being sought, transmission properties of the intervening medium and cost limits. Over the years, GPR systems have found many applications within ground probing as the following list of some major GPR applications indicates:

- Buried Objects Detection: The location of buried objects using GPR systems is probably the largest area of GPR application. GPR systems have been used for the detection of various buried objects, which include landmines and unexploded ordinance [16, 17], buried pipes and cable [2, 7, 18]. GPR systems have also been successfully used in locating victims of snow avalanches [19, 20].

- Civil engineering: GPR systems have found use in various civil engineering applications. In road structure surveys, GPR has been used to measure layer thickness, detect subsurface defects and evaluate base course quality [21, 22]. GPR Systems have also been used to access the condition of bridges prior to maintenance work [23, 24]. Also work accessing the benefits and limits of using GPR systems to perform railway track inspections has shown promise [25, 26].

- Archaeological studies: GPR systems have proved to be a valuable tool in archaeology. GPR surveys can be used to provide detailed survey information that has been provided in the past by extensive excavation, but without the high cost of excavation, the dangers of vandalism, and without disturbing sensitive areas. GPR Surveys have been used to create a complete map of an ancient buried village [27], uncover ancient roads [28] and update old maps in the Cathedral of Valencia, Spain [29] to mention a few.

- Geophysics: In the field of Geophysics GPR systems have been used for various purposes such as mapping mineral resources [30], investigation of geological structures around faults [31] and imaging\estimation of ground water level [32, 33]. GPR has also found use in space exploration, where a GPR system was integrated into the Mars 96 balloon mission to image Martian Permafrost [34].

2.2 Ultra-wideband GPR Systems

In GPR applications for detecting buried object such as utility lines, cables and landmines there is a need for high resolution to distinguish closely located targets, different target types and show the detailed structure of the targets. To achieve high resolution, it is desirable that the transmitted waveform has a large bandwidth [35]. Radar systems, which use high bandwidth signals, are referred to as Ultra Wideband Radars. Ultra wideband GPR systems have been built using a variety of high-resolution waveforms based on different modulation schemes [36] and can be broadly categorised into three main three main categories, namely: Short Pulse (Impulse), Frequency Modulated Continuous Wave (FMCW) and Stepped Frequency.

2.2.1 Short Pulse Radar

The majority of current GPR systems are short pulse or impulse radars. The radar transmits an impulse with a width ranging typically between 200ps to 15ns. The return signal is proportional to the target range and the spectrum of the return signal contains information about the target. Impulse radars have the disadvantage of low transmitted pulse energy due to the very narrow width; hence peak transmitting power has to be high to attain reasonable resolution. Also the high instantaneous bandwidths of the pulses mean that an A/D converter with a high sampling rate is required to record the received signal.

2.2.2 Frequency Modulated Continuous Waveform Radar

FMCW radars use a voltage-controlled oscillator to transmit a continuously changing carrier frequency on a repetitive basis. The received signal is mixed with a sample of the transmitted signal to produce a difference frequency. The difference frequency is dependent on the delay between the transmitted signal and received signal and hence the target range. The typical FMCW sweep time ranges from 1ms to 100ms, giving high pulse

energy with low transmission power. In addition FMCW radars have the advantage of wider dynamic range and lower noise than the other methods. However, FMCW systems have the disadvantages of being complicated and needing a very stable VCO, as non-linearity in the frequency sweep leads to spectral widening of the difference frequency, hence degrading the resolution of the system. FMCW radars are particularly suitable for locating shallow targets that require high resolution.

2.2.3 Stepped Frequency Radar

There are two forms of the Stepped Frequency radar. The first is Stepped Frequency Continuous Wave (SF-CW) radar, which has an operating principle similar to that of the FMCW radar. Instead of a linear frequency sweep, the system steps through a number of discrete frequencies in a staircase fashion. The SF-CW base band signal, which is extracted from its return signal, can be viewed as a discrete version of the FMCW difference signal and will contain exactly the same target information. This form of stepped frequency radar has the advantage that the operating frequencies can be adjusted to suit the materials and targets under investigation. The second form is the more complex Synthesised Pulse radar. In the Synthesised Pulse radar the amplitudes and phases of each individual frequency are weighted on transmission in order to synthesise the desired pulse waveform. This form has the advantage of being able to take into account the frequency characteristics of the antenna, but has the disadvantage of needing to maintain accurate phase relations between the individual frequencies which is difficult to achieve in real time.

2.3 Ground Penetrating Radar Theory

In conventional radar systems any design or analysis begins with the radar equation. The radar equation is used to calculate the received power levels after the radar signal is reflected by a target [37]. For GPR, the radar equation describes how the transmitted signal is changed due to:

1. Transmitter and receiver properties (gain, antenna beam patterns, frequency dependence)
2. Exponential material attenuation loss
3. Spreading loss
4. Scattering (reflection, refraction and diffraction) due to change of dielectric properties

The material attenuation loss is due to the propagation of the GPR signal in lossy dielectric media and is modelled using electromagnetic theory, whereas the scattering of the GPR signal is modelled using geometrical optics theory. The spreading loss is conventionally related to the inverse fourth power of the range to the target. The range to the target is determined by the propagation path of the GPR signal, which is in turn modelled using the geometry of GPR signal scattering. The transmitter and receiver properties are dependent on the type of antennas used and are chosen to suit the intended application. In this section the theory necessary to derive the radar equation for GPR systems is presented.

2.3.1 Propagation of Waves in Media

The propagation of electromagnetic waves is determined by Maxwell's equations [38]. For a linear isotropic homogeneous medium with permeability μ, permittivity ε and conductivity σ, Maxwell's equations are represented as

$$\nabla \times \mathrm{E} = -\mu \frac{\partial \mathrm{H}}{\partial t} \tag{2.1}$$

$$\nabla \times \mathrm{H} = \sigma \mathrm{E} + \varepsilon \frac{\partial \mathrm{E}}{\partial t} \tag{2.2}$$

$$\nabla \times \mathrm{E} = 0 \tag{2.3}$$

$$\nabla \times \mathrm{H} = 0 \tag{2.4}$$

where H is the magnetic field vector and E is the electric field vector.

The second order differential equations (2.5) and (2.6), otherwise known as the wave equations are derived through a combination of the equations (2.1) to (2.4):

$$\nabla^2 \mathrm{E} = \mu\sigma \frac{\partial \mathrm{E}}{\partial t} + \mu\varepsilon \frac{\partial \mathrm{E}}{\partial t^2} \tag{2.5}$$

$$\nabla^2 \mathrm{H} = \mu\sigma \frac{\partial \mathrm{H}}{\partial t} + \mu\varepsilon \frac{\partial \mathrm{H}}{\partial t^2} \tag{2.6}$$

The solutions to (2.5) and (2.6) represent propagating waves. The particular solutions where points of constant phase are infinite planes normal to the direction of propagation are known as plane waves. In the far field region of an antenna, electromagnetic waves can be approximated by plane waves.

For a propagating wave due to a sinusoidal time varying field, the wave equations (2.5) and (2.6) are represented in phasor form as:

$$\nabla^2 \hat{\mathrm{E}} = j\omega\mu(\sigma + j\omega\varepsilon)\hat{\mathrm{E}} \tag{2.7}$$

$$\nabla^2 \hat{\mathrm{H}} = j\omega\mu(\sigma + j\omega\varepsilon)\hat{\mathrm{H}} \tag{2.8}$$

where ω is the frequency of the wave.

The propagation constant of the propagation media, γ is defined as:

$$\gamma = \sqrt{j\omega\mu(\sigma + j\omega\varepsilon)} \tag{2.9}$$

The propagation constant can be written as a sum its real and imaginary parts:

$$\gamma = \alpha + j\beta \tag{2.10}$$

where the attenuation constant, α and phase constant, β determine the attenuation and phase of the wave respectively.

Now consider an electromagnetic wave propagating in the z direction with perpendicular magnetic and electric fields as shown in Figure 2.1 [39]. Expanding (2.7) results in:

$$\frac{\partial^2 \hat{\mathrm{E}}}{\partial z^2} = \gamma^2 \hat{\mathrm{E}} \tag{2.11}$$

The solution to (2.11) is (2.12), which describes the wave propagation of Figure 2.1

$$E(z,t) = \mathrm{E}_o.e^{-\gamma z}.e^{j\omega t} = \mathrm{E}_o.e^{-\alpha z}.e^{j(\omega t-\beta z)} \tag{2.12}$$

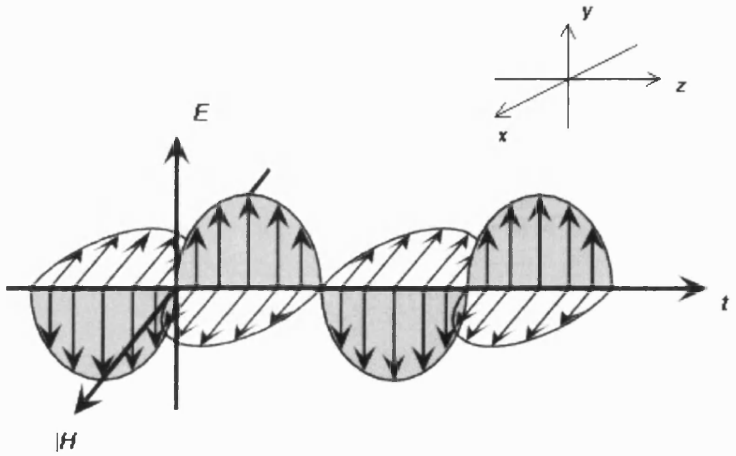

Figure 2.1 Propagation of electromagnetic waves [39]

For a perfect dielectric medium with no losses (i.e. $\sigma = 0$), the propagating wave is described by

$$E(z) = E_o e^{-j\beta z} \tag{2.13}$$

where the phase constant, β is:

$$\beta = \frac{\omega}{\sqrt{\mu\varepsilon}} \tag{2.14}$$

and the velocity of propagation v is:

$$v = \frac{1}{\sqrt{\mu\varepsilon}} \tag{2.15}$$

The refractive index of the medium n is:

$$n = \sqrt{\mu\varepsilon} \tag{2.16}$$

and the intrinsic impedance of the medium Z is:

$$Z = \sqrt{\frac{\mu}{\varepsilon}} \tag{2.17}$$

In the case of lossy media (i.e. $\sigma \neq 0$), the propagating wave is described by equation (2.12). For most lossy media of interest the magnetic response is weak and need not be considered as a complex quantity. However, the permittivity is replaced by the complex permittivity

$$\varepsilon_c = \varepsilon' - j\varepsilon'' \equiv \varepsilon - j\frac{\sigma}{\omega} \tag{2.18}$$

The propagation constant then becomes

$$\gamma = \alpha + j\beta = j\omega\sqrt{\mu\varepsilon'\left(1 - j\frac{\varepsilon''}{\varepsilon'}\right)} \tag{2.19}$$

where α and β are given by

$$\alpha = \omega\left[\frac{\mu\varepsilon'}{2}\left(\sqrt{1+\left(\frac{\varepsilon''}{\varepsilon'}\right)}-1\right)\right]^{1/2} \tag{2.20}$$

$$\beta = \omega\left[\frac{\mu\varepsilon'}{2}\left(\sqrt{1+\left(\frac{\varepsilon''}{\varepsilon'}\right)}+1\right)\right]^{1/2} \tag{2.21}$$

and the velocity of propagation is

$$v = \frac{\omega}{\beta} \tag{2.22}$$

The ratio $\varepsilon''/\varepsilon'$ is known as the material loss tangent as it is a measure of the power loss in the media

$$\frac{\varepsilon''}{\varepsilon'} = \tan\delta \tag{2.23}$$

Most materials of interest, including soils, snow and man made materials such as concrete fall under this category.

2.3.2 Electromagnetic Properties of Lossy Media

The determination of the electromagnetic properties of lossy media remains largely experimental [40-43]. Typical lossy media such as soils and concrete are complicated mixtures of various materials. Various workers have attempted to model the dielectric properties of soils [44, 45] and concrete [46]. At microwave frequencies, the permittivity of soil is to a large extent dependent on its moisture content. At such frequencies the dielectric losses in soils are due to relaxation of the free form of water [44].

Material	**Conductivity, σ (S/m)**	**Relative Permittivity, ε_r (F/m)**
Air	0	1
Asphalt: dry	10^{-3} - 10^{-2}	2 - 4
Asphalt: wet	10^{-2} - 10^{-1}	6 -12
Concrete: dry	10^{-3} - 10^{-2}	4 - 10
Concrete: wet	10^{-2} - 10^{-1}	10 - 20
Sand: dry	10^{-7} - 10^{-3}	4 - 6
Sand: Saturated	10^{-4} - 10^{-2}	10 - 30
Soil: sandy dry	10^{-4} - 10^{-2}	4 - 6
Soil: sandy wet	10^{-2} - 10^{-1}	15 - 30
Soil: loamy dry	10^{-4} - 10^{-3}	4 - 6
Soil: loamy wet	10^{-2} - 10^{-1}	10 - 20
Soil: clayey dry	10^{-4} - 10^{-1}	4 - 6
Soil: clayey wet	10^{-1} - 1	10 - 15

Table 2.1 Typical range of dielectric characteristics of various materials measured at 100MHz

In the previous section, we have seen how the electromagnetic properties of lossy media are related to the propagation of electromagnetic waves [Equations (2.12) to (2.23)]. The losses due to material attenuation are given as a function of permittivity in (2.20). Equation (2.20) suggests that attenuation will increase exponentially as the frequency of the wave increases. But at the same time the complex permittivity (equation (2.18)) is a function of frequency. Results in [41] show that the permittivity of soil increases with frequency whereas conductivity decreases as frequency increases. However, both the permittivity and conductivity were found to increase with increasing moisture content. Similar results are reported for concrete [46]. Table 2.1 shows some typical values of electrical properties of some materials measured at 100MHz [9].

2.3.3 GPR Signal Scattering

The geometry of scattering for incident plane waves on a multi-layer dielectric is shown in Figure 2.2. At each dielectric boundary some energy is reflected due to a change in intrinsic impedance. Geometrical optics can be used to model the propagation path of the waves and the ratios of energy reflected and transmitted.

The relationship between the angles of incidence, reflection and refraction and the refractive indices are given by Snell's Law [47]. Fresnel's Law describes the ratios of transmission coefficient and reflection coefficient at the dielectric boundary in terms of the angles of incidence and refraction and the intrinsic impedances of the dielectrics. At the dielectric boundary $(1,2)$ in Figure 2.2, equations (2.24) and (2.25) must hold according to Snell's Law.

$$\theta_1 = \theta_3 \tag{2.24}$$

$$\frac{Sin\theta_1}{Sin\theta_2} = \frac{n_1}{n_2} \tag{2.25}$$

The Fresnel reflection and transmission coefficients depend on the polarization of the incident waves. At the dielectric boundary (1,2) the reflection and transmission coefficients are given by (2.26) and (2.27) respectively for parallel polarized waves and by (2.28) and (2.29) for perpendicular-polarized waves:

$$R_{\parallel}^{(1,2)} = \frac{Z_2 Cos\theta_1 - Z_1 Cos\theta_3}{Z_1 Cos\theta_3 + Z_2 Cos\theta_1} \tag{2.26}$$

$$T_{\parallel}^{(1,2)} = \frac{2Z_1 Cos\theta_1}{Z_1 Cos\theta_1 + Z_2 Cos\theta_3} \tag{2.27}$$

$$R_{\perp}^{(1,2)} = \frac{Z_1 Cos\theta_1 - Z_2 Cos\theta_3}{Z_1 Cos\theta_1 + Z_2 Cos\theta_3} \tag{2.28}$$

$$T_{\perp}^{(1,2)} = \frac{2Z_1 Cos\theta_1}{Z_1 Cos\theta_3 + Z_2 Cos\theta_1} \tag{2.29}$$

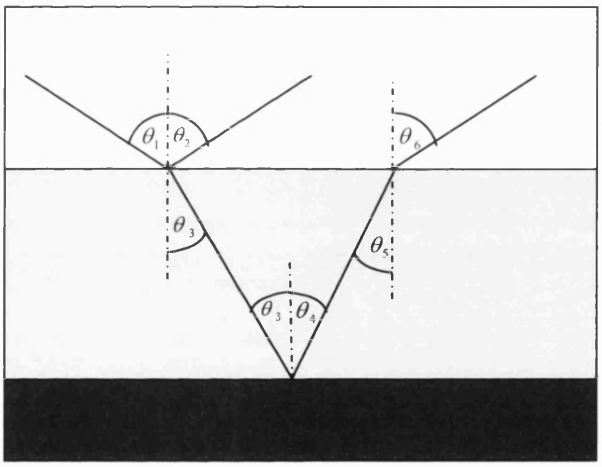

Figure 2.2 Geometry of scattering of a 3 layer dielectric

The reflection coefficient and transmission coefficient are related as shown in (2.30):

$$T = 1 + R \tag{2.30}$$

Therefore the two-way scattering loss that will be suffered by the wave in Figure 2.2, that originates in medium 1 and is reflected at boundary (2, 3), is given as

$$L_s = T^{(1,2)} R^{(2,3)} T^{(2,1)} \tag{2.31}$$

The scattering loss for a wave incident on an infinite target i.e. medium 3 in Figure 2.2 has been derived. However, when considering a target embedded within a multi layer dielectric, the radar cross-section (RCS) of the target, σ has to be taken into account. The RCS of a target is a measure of the target's ability to reflect signals in the direction of the receiver and is dependent on the wavelength of the radar signal.

The RCS for a complex shaped target is usually difficult to obtain, but for simpler shapes such as cylinders, cones and spheres a single value for their RCS can be calculated. Formulae for the RCS of a few simple shapes are given in [37].

After adjusting for the target's RCS, the scattering loss suffered by a wave reflected by a target is given as

$$\begin{aligned} L_s' &= \sigma L_s \\ &= \sigma T^{(1,2)} R^{(2,target)} T^{(2,1)} \end{aligned} \tag{2.32}$$

where $R^{(2,target)}$ is the reflection coefficient for the wave propagating in Medium 2, which the target reflects. The target is also in Medium 2.

2.3.4 The GPR Equation

The effects of all the losses due to scattering, material attenuation, antenna properties and spreading discussed and described in the previous sections are represented in the GPR equation as:

$$P_r = P_t G_t G_r \left(\frac{\lambda}{4\pi r_a r_b} \right)^2 \sigma \alpha'_{r_a + r_b} L_s \tag{2.33}$$

where

P_r is the received power

P_t is the transmitted power

G_r is the gain of the receiving antenna

r_a is the range from the transmitter to the target

r_b is the range from the target to the receiver

G_t is the gain of the transmitting antenna

$\alpha'_{r_a+r_b}$ is the material attenuation loss suffered due to the total propagation distance

$r_a + r_b$

λ is the wavelength of propagating wave

σ is the target radar cross section

and L_s is the scattering loss.

2.3.5 GPR Performance

As mentioned in section 2.3, the design of a GPR system depends on its intended use. When a GPR system is being designed a range and resolution performance requirement is normally specified depending on the type of targets and the environment in which the targets are located. The range performance refers to the depth to which the system is expected to detect targets where as the resolution performance refers to the ability of the system to correctly resolve separated targets.

The range performance is governed by the losses suffered by the signal in the propagation medium where as the resolution is governed by the GPR signal bandwidth. Therefore to improve resolution performance in GPR applications we could consider increasing the signal bandwidth of the GPR signal [35]. However, for lossy media like most soils, material attenuation loss (determined by the attenuation constant (2.20)) tends to be very high and rises rapidly with frequency [45, 48] (see also section 2.3.1and 2.3.2). This means that higher resolutions might not necessarily be achieved through the use of a larger bandwidth signal as the higher frequency signal could be severely attenuated, hence limiting the penetration depth of the signal.

Table 2.2 shows some typical values of material attenuation loss measured at 100MHz and 1GHz [9]. Table 2.2 shows that an increase in frequency leads to an increase in material

attenuation, hence any gain in resolution performance from increasing the frequency of operation will be at the expense of the systems range performance.

Material	Loss at 100 MHz /dbm^{-1}	Loss at 1GHz/dbm^{-1}
Clay(moist)	5-300	50-3000
Loamy soil (moist)	1-60	10-600
Sand (dry)	0.01-2	0.1-20
Ice	0.1-5	1-50
Fresh water	0.1	1
Sea water	100	1000
Concrete (dry)	0.5-2.5	5-25
Brick	0.03-2	3-20

Table 2.2 Typical material attenuation losses at 100 MHz and 1GHz [9]

In applications such as buried utility line location high resolution is required to resolve the normally closely located utility lines and provide detailed structure if required. However, the range performance is less stringent as most utility lines are located within a metre, or two, of the surface of the ground. This means that large bandwidth signals such as the FMCW are more suitable for this type of application.

On the other hand, in applications such as media layer thickness investigations the resolution performance requirement is usually less stringent as the target is a large planar surface (i.e. the media to media interface). In such cases a high range performance is required as a strong response is required from the target to achieve accurate results, hence making high frequency signals less suitable.

2.4 Conclusion

In this chapter a brief introduction to the field of GPR has been presented. The history of GPR as a technique was traced. Some examples of its major applications were listed followed by a discussion on the classification of GPR systems based on waveforms employed. This was followed by an analysis of electromagnetic theory and geometrical optics for GPR which were used to derive the GPR equation. Finally some performance considerations in GPR design were discussed.

Chapter 3: Frequency Modulated Continuous Wave GPR

3.1 FMCW System

Figure 3.1 shows a functional representation of a typical Linear FMCW GPR system [49]. The signal is generated by a Voltage Controlled Oscillator (VCO), which produces a continuously changing carrier frequency. At the receiver end, the received signal is mixed with a sample of the transmitted signal in the mixer, followed by filtering to produce the beat signal. The beat signal is sampled and fed into the signal processing hardware where signal-processing techniques are applied to extract target information including the range.

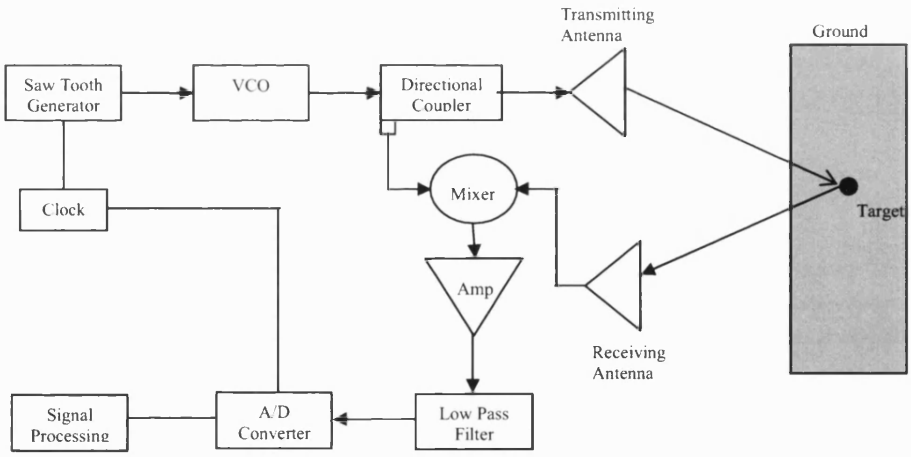

Figure 3.1 Typical FMCW system

3.2 FMCW Signal Analysis

In this section a mathematical description of an FMCW radar signal is presented. Figure 3.2 shows the time-frequency relation of the waveform transmitted by a typical FMCW radar, the frequency changes linearly over a range of Δf Hz starting at frequency f_0 over the time interval T_s, repeating every T_r.

The instantaneous frequency of the transmitted signal is given as:

$$f_{tr}(t) = f_0 + \frac{\Delta f}{T_s} t \tag{3.1}$$

where the phase of the signal is:

$$\begin{aligned} \phi &= 2\pi \int_0^t f(t)\,dt \\ &= 2\pi \left(f_0 t + \frac{\Delta f}{2T_s} t^2 \right) \end{aligned} \tag{3.2}$$

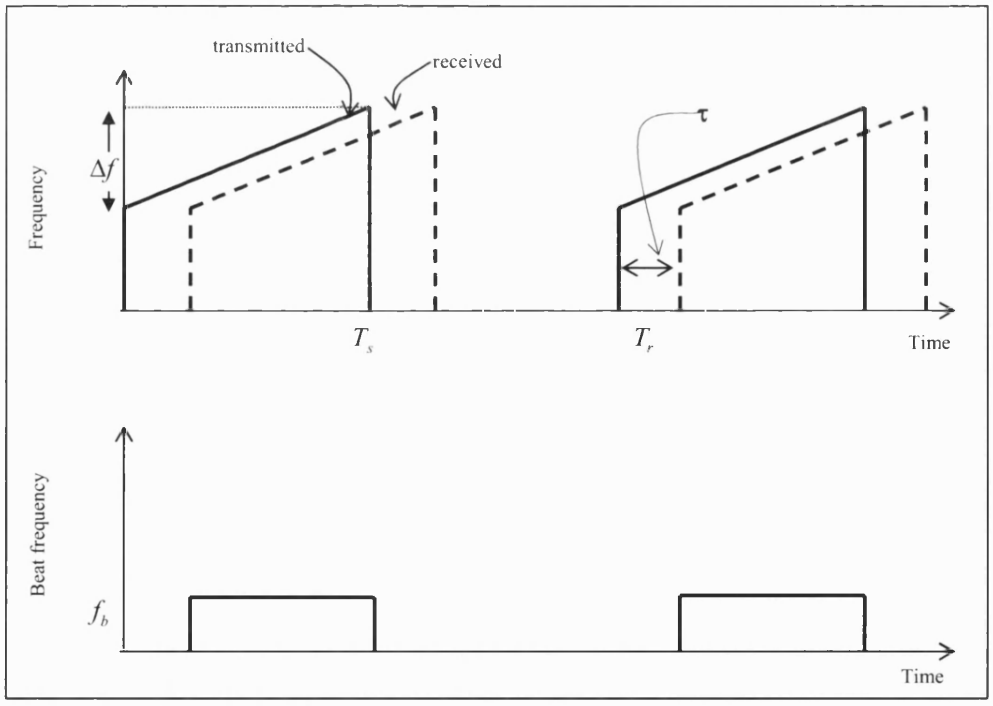

Figure 3.2 FMCW radar principle

Figure 3.2 also shows the time–frequency relation of the reflected signal. The time delay τ represents the time it takes the signal to travel to and from the target, with the instantaneous frequency of the received signal is given as:

$$f_{rec}(t) = f_0 + \frac{\Delta f}{T_s}(t-\tau) \tag{3.3}$$

The difference between the transmitted and received instantaneous frequencies also known as the beat frequency, f_b is given as:

$$\begin{aligned} f_b &= f_{tr}(t) - f_{rec}(t) \\ &= \frac{\Delta f}{T_s}\tau \end{aligned} \tag{3.4}$$

From the beat frequency f_b, the 2-way distance to the target, r is calculated using the following formula:

$$r = \frac{vT_s}{2\Delta f} f_b \tag{3.5}$$

where v is the signal velocity

Using equations (3.1) and (3.3), the time waveforms of the FMCW radar transmitted and received signals time are given as (3.6) and (3.7) respectively:

$$S_{tr}(t) = A\cos\left[2\pi\left(f_o + \frac{M}{2}t\right)t\right] \tag{3.6}$$

$$S_{rec}(t) = AA'\cos\left[2\pi\left(f_o + \frac{M}{2}(t-\tau)\right)(t-\tau)\right] \tag{3.7}$$

where

A	Amplitude of transmitted signal,
A'	Attenuation of received signal due to total path loss,
f_o	Centre frequency in sweep,
$M = \Delta f / T_s$	Modulation rate,
t	Time,
τ	Time delay,

Δf Sweep width,

T_s Sweep time.

At the receiver, the received signal is mixed with the original transmitted signal, which produces difference terms, one of which has frequency f_b (Figure 3.2), the *beat frequency*. The mixed signal is then low pass filtered to extract the beat frequency term, represented as:

$$S_b(t) = AA'cos\left[2\pi\left(f_o\tau + M\tau t - \frac{M}{2}\tau^2\right)\right] \tag{3.8}$$

The coefficient $M\tau$ with respect to time is the beat frequency, f_b i.e.

$$f_b = M\tau \tag{3.9}$$

The beat frequency is then determined using spectral analysis techniques such as the Fourier transform. Taking the Fourier transform of the beat signal (3.9) with respect to the sweep time gives (3.10), which is in the form of a *sinc* (*sin x/x*) function with a peak at the beat frequency f_b.

$$S_b(f) = \frac{AA'T_s}{2}\exp(2\pi f_o\tau)sinc\left[\pi(f - f_b)T_s\right] \tag{3.10}$$

A multi target beat signal model is then derived by applying superimposition (given that the radar system is a linear system). Equation (3.11) gives the received signal due to reflection by N targets, i.e. a sum of the reflections due to N individual targets with the corresponding beat signal and Fourier beat spectrum given as (3.12) and (3.13) respectively.

$$S_{recN}(t) = \sum_{i=1}^{N} AA_i'cos\left[2\pi\left(f_o + \frac{M}{2}(t-\tau_i)\right)(t-\tau_i)\right] \tag{3.11}$$

$$S_{bN}(t) = \sum_{i=1}^{N} AA_i'cos\left[2\pi\left(f_o\tau_i + M\tau_i t - \frac{M}{2}\tau_i^2\right)\right] \tag{3.12}$$

$$S_{bN}(f) = \sum_{i=1}^{N} \frac{AA_i'T_s}{2}\exp(2\pi f_o\tau_i)sinc\left[\pi(f - f_{b\,i})T_s\right] \tag{3.13}$$

3.3 Beat Spectrum Analysis

Extracting target distance information requires some form of spectral analysis of the beat signal. In early work with FMCW systems, the frequency spectrum of beat signal data was calculated using a spectrum analyser [50]. More recently it has been done using signal processing techniques such the Fourier Transform via FFT algorithms running on computers or DSP hardware [49, 51, 52]. The FFT though computationally efficient suffers from spectral leakage leading to unwanted side lobes and has a restricted resolution due to the finite nature of the burst of the beat signal (discussed in detail in section 4.2). Other spectral analysis techniques such as system modelling and eigen-analysis based methods have also been used for beat spectrum analysis in FMCW radars.

The modelling approach to estimating the spectrum of an FMCW radar beat signal has been used in [53], with results showing that the method could be used to achieve better frequency resolution than using an FFT algorithm. The main lobes of the spectrum were narrower and side lobes levels were significantly lower than those obtained using an FFT algorithm.

In [54] a comparison of some spectral estimation methods for FMCW radar beat signals was carried out. Auto-Regressive (AR) modelling, a type of system modelling spectral analysis, Multiple Signal Classification (MUSIC) algorithm, an eigen-vector based method and a maximum likelihood method were compared at various signal-to-noise ratios (SNR) on a simulated data set. Results showed that the MUSIC algorithm and AR modelling methods were the better performers, being able to resolve to a high degree at low SNR. However, overestimating the number of sinusoids for the MUSIC algorithm at low SNR introduced a significant number of false peaks.

The MUSIC algorithm has been used in experimental GPR measurements where the number of targets are known a priori [55]. In [56] a combined method is proposed which combines the received signal level of an FFT spectrum and the resolution capabilities of the MUSIC algorithm to improve resolution. However, the method is tested on experimental data with the number of targets known a priori.

Sections 3.3.1 and 3.3.2 provide brief summaries of Modelling and Eigen vector approaches to spectral estimation.

3.3.1 System Modelling

The system modelling method is based on assuming a time series model for the data. The estimated spectrum is then a function of the model. It uses the fact that real discrete signals can be represented by the filter linear difference equation:

$$y[n] = -\sum_{k=1}^{p} a_k y[n-k] + \sum_{k=0}^{q} b_k x[n-k] \tag{3.14}$$

where $x[n]$ and $y[n]$ are the input and output sequences respectively.

In transfer function form, (3.14) becomes:

$$H(z) = \frac{\sum_{k=0}^{q} b_k z^{-k}}{1 - \sum_{k=1}^{p} a_k z^{-k}} \tag{3.15}$$

The next step is to determine the model parameter i.e. coefficients a_k and b_k , that will produce an impulse response that is the same as the beat signal data, i.e. the input sequence $x[n]$. The frequency spectrum is then computed by evaluating the model around a unit circle i.e. using the following substitution

$$z = e^{jw}[\omega = 0 : 2\pi] \tag{3.16}$$

.

The model can fall under the following categories based on its poles and zeros:

1. All poles model, also known as the Autoregressive (AR) model.
2. All zeros model, also known as the Moving Average (MA) model
3. Zeros and Poles model, also known as the Autoregressive Moving Average (ARMA) Model.

The all poles model has the advantage of having sharper peaks and the coefficients can be estimated by solving a set of linear coefficients, whereas estimates of the coefficients of the MA and ARMA models require the solution of non-linear equations.

One of the drawbacks to this approach to spectral analysis is choosing the optimal number of coefficients to be used. If too few are chosen a poor spectrum will result whereas if too many are chosen then instability and false peaks can occur. A comparison of various methods of computing the coefficients of the AR (all poles) model is given in [57].

3.3.2 Eigen Vector Methods

The more complex eigen-analysis methods are based on the eigen analysis of the auto correlation matrix or covariance matrix of the data. The eigen decomposition of the correlation or covariance matrix is separated into a signal vector subspace and a noise vector subspace. Because vectors in a eigen decomposition are orthogonal to each other, this means that theoretically the signal subspace vectors will be orthogonal to the noise subspace vectors. Therefore any linear combination of the noise subspace vectors with a signal subspace vector will equal zero. This is the basis of the eigen analysis approach to spectral estimation. The basic structure of any eigen analysis frequency estimator function is in the form of the reciprocal of a weighted linear combination of the possible signal subspace vectors with the separated noise subspace vectors [58], as shown in (3.17).

$$\frac{1}{\sum_{k=M+1}^{p} \alpha_k \left| e^H(f) v_k \right|^2} \tag{3.17}$$

Where

α_k is the weighting factor

v_k for $k = M+1$ to p are the noise subspace vectors

$e(f)$ is a sinusoidal vector:

$$e(f)=\begin{bmatrix} 1 \\ sin(2\pi fT) \\ sin(2\pi(2f)T) \\ \vdots \\ sin(2\pi MfT) \end{bmatrix} \tag{3.18}$$

$e^H(f)$ is the Hermitian transpose of $e(f)$

When the frequency matches the frequency of one of the frequency components of the signal subspace vectors, equation (3.17) will have an infinite value. In practice due to estimation errors in the function, sharp peaks at frequency locations of sinusoids or narrowband components will appear. If the number of sinusoids is known, the separation is done by selecting the largest eigen values up to the known number of sinusoids. However, as this is part of the problem in the first place an alternative means is required. This can be done by examination of the relative magnitudes of the eigen values of the eigen decomposition of the auto correlation matrix or the singular values of the singular value decomposition (SVD) of the data matrix subspace. Examples of frequency estimator function include the MUSIC (Multiple Signal Classification) and EV (Eigen vector) algorithms and are given as (3.19) and (3.20) respectively [58].

$$P_{music}(f)=\frac{1}{e^H(f)\left(\sum_{k=M+1}^{p} v_k v_k^H\right)e(f)} \tag{3.19}$$

$$P_{EV}(f)=\frac{1}{e^H(f)\left(\sum_{k=M+1}^{p} \frac{1}{\lambda_k} v_k v_k^H\right)e(f)} \tag{3.20}$$

Where λ_k for $k = M+1$ to p are corresponding eigen values for the noise subspace vectors.

Ultimately the performance of this of approach to spectral estimation depends on how well the signal and noise subspace vectors are separated. Also this approach to spectral estimation does not yield the true distribution of power in the signal spectrum. The relative

sizes of the peaks are not an indication of the relative strengths of the frequency components of the original data and the original data sequence cannot be recovered by inverse Fourier transforming the spectrum produced through this approach. Therefore this approach can only be used to identify presence of targets but the magnitude values of the peaks cannot be used to extract further target information.

Figure 3.3 shows the DFT and MUSIC spectrums of a real signal with components at 5 kHz and 5.5 kHz and relative strength of 4 to 1 respectively. Figure 3.3 shows the DFT spectrum failing to resolve apart the two frequency components whereas the MUSIC algorithm detects and resolves apart the two frequencies correctly when the correct signal dimension of 2 is used (i.e. M=2 in the frequency estimator function, (3.19) or (3.20)). However, when the dimension is set to 1 the MUSIC algorithm detects the stronger frequency at 5 kHz only and when the dimension is set to 3 a third false frequency component appears in the spectrum.

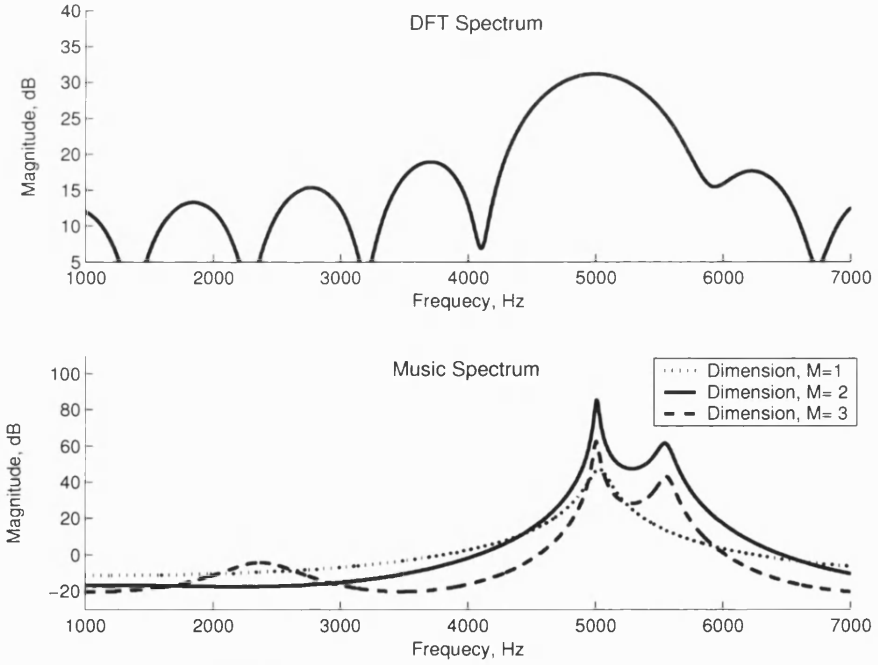

Figure 3.3 DFT and MUSIC spectrums of signal with components at 5 kHz and 5.5 kHz

This highlights the need for an accurate choice of model order selection to achieve an accurate MUSIC spectrum as it tends to find the number of frequency components it has been set up to find. In GPR applications determining the number targets with no prior knowledge of the targets is part of the problem and in GPR applications such as buried utility line or mine detection failing to detect a target can have dire consequences.

3.4 Target Detection

After spectral analysis, extraction of target information is required. It could be as simple as reading the frequency index of peaks in the beat spectrum but due to clutter, noise, soil attenuation (and side lobes when using DFT) not every peak in the spectrum necessarily corresponds to a target, hence the need for more clever detection schemes.

Various detection schemes have been used to detect the presence of targets in FMCW radar beat signals. The detection schemes based on thresholding, correlation, template matching and pattern matching using neural networks are discussed in the next three sections.

3.4.1 Thresholding

The simplest detection scheme is based on the thresholding technique. Thresholding involves comparing data to a reference level and only investigating data that exceeds the reference. After thresholding the beat signal spectrum, any remaining peaks are considered to be beat frequencies due to reflections from targets. However, this technique is inadequate especially when dealing with multi target scenarios. The major difficulty is choosing an appropriate threshold value or threshold function. This value should be chosen to be above the noise values but at the same time has to take into account the effects of rapid signal decay due to losses suffered by targets (see section 2.3) and when using a Fourier transform spectrum such as the DFT the unwanted side lobes have to be taken into account. In some cases rather than using a threshold function, a filter function is applied to

the spectrum to compensate for the attenuation [51]. Again this requires accurate modelling of the soil attenuation (see section 2.3).

3.4.2 Correlation

In conventional radar systems the ability to detect a target is a function of the signal-to-noise ratio (SNR) at the receiver input, the larger the SNR the greater the possibility of successful target detection. When the noise power is not dependent on the noise impulse response, but rather on the gain of the receiver (such as white noise) the best SNR is achieved by maximising the response of the signal term. To achieve this, a matched filter is used [59]. Applying the matched filter is equivalent to taking the cross correlation between the received signal and the transmitted, hence the name correlation receiver. The frequency domain representation of the matched filter is

$$H(f) = S^*(f) \tag{3.21}$$

where $S^*(f)$ is the complex conjugate of the signal of interest.

The corresponding time domain representation is a time-reversed version of the signal of interest

$$h(t) = s(-t) \tag{3.22}$$

Because the data to be processed in an FMCW radar is in the frequency domain (i.e. the beat signal spectrum), the correlation receiver in this context is equivalent to taking the cross correlation between the expected target response (see equation (3.10)) and the beat signal spectrum.

$$R(f) = S_b(f) * B(f) = \int_0^{\psi_{max}} S_b(\psi) B(\psi + f) d\psi \tag{3.23}$$

Where $B(f)$ is the beat signal spectrum

ψ_{max} is the maximum frequency in the beat signal spectrum

The output of the correlation receiver (3.23) can be represented in a form, which is easily implemented by using the relationship of the Fourier transform of a correlation function as:

$$R(f) = FT\left[s_b(t) \times b(t)\right] \tag{3.24}$$

where FT is the Fourier Transform operator.

Therefore the beat signal data need not be converted to its frequency domain representation immediately. The ease with which such a receiver is implemented is its major advantage. However, the noise contained in GPR signals is not usually white noise but rather some correlation does exist between noise values (i.e. the noise is coloured). Results obtained by Carr et al. [50] showed that applying a correlation receiver to a beat signal spectrum degrades resolution and increases side lobe levels.

3.4.3 Template Matching

The template matching technique involves the use of optimisation methods to match a function to the beat signal spectrum. The basic form of this technique assumes that the shape or template of the target response is always the same. The template is described as a function and the beat spectrum is then modelled as a sum of the template functions at different positions with different amplitudes. The expression for such a model is given as [60]:

$$r(\omega) = \sum_{j=1}^{P} A_j^2 W\left(\omega - \Omega_j\right) \tag{3.25}$$

where

$r(\omega)$ is the model return

A_j^2 is the amplitude of the jth template

$W(\omega)$ is the template function

Ω_j is the position of the jth template.

This method was first used at Queen Mary University London [50]. The beat signal spectrum was first low pass filtered to remove unwanted high frequency components and smooth the data. A non-linear optimization routine was then used to fit the model to the beat signal spectrum data by minimizing an error function. The resulting position variables gave the position of each target and the amplitude variables gave the relative strength of the response from each target. Results showed that closely spaced targets and targets masked by side lobes of stronger targets could be detected. A follow up to this work was carried out to enhance the detection scheme to detect target types [61]. Targets with simple shapes were classified as a library of template functions; optimization was then used to get a match with one of the template functions in the library. The results showed that some target types could be detected but the method was unreliable in some instances. The main drawback to this method of target detection is the complex nature of the optimization techniques.

3.4.4 Pattern Matching using Neural Networks

A Neural Network is an information processing paradigm that is inspired by the way biological nervous system such as the brain works. The network is composed of a large number of highly interconnected processing elements (neurones) working in unison to solve specific problems [62]. Neural networks are mainly used for pattern recognition and data classification applications. Just like the brain a neural network has the ability to learn, which is done by providing the network with a training set that is representative of the type of pattern it is trying to match. Typically for GPR systems that use neural networks, the network is trained to recognize certain expected distinctive features of the reflected signal of a target [5]. Neural networks have also been used to detect hyperbolic signatures that indicate the presence of a target from a set of continuous GPR scans [63-65]. The main drawback to this approach is complexity and choosing a training set that is truly representative of the targets being sought.

3.5 FMCW GPR for Buried Utility Location

FMCW has often been used in GPR systems for buried utility line location as its bandwidth provides the necessary resolution performance [51, 66]. As discussed earlier in section 3.3, FMCW systems often rely on the DFT for signal analysis. The DFT, though computationally when implemented using a Fast Fourier Transform (FFT) [67], has a limited resolution and unwanted side lobes in the computed spectrum which, when combined with high frequency attenuation in soils (see section 2.3), can severely degrade the performance of an FMCW GPR system. In particular unwanted side lobes in the DFT beat spectrum from strong targets can obscure main lobes of weaker targets in their vicinity or can be mistaken as false targets. The next chapter addresses this problem in depth with a technique for improving DFT spectral analysis being proposed.

Another factor that limits the resolution performance of FMCW systems is when there is non linearity of the frequency sweep. Non linearity in the VCO frequency sweep leads to spectral widening of the beat signal spectrum, hence degrading system resolution [68, 69]. Several signal processing techniques have been proposed for correcting non-linearity effects in the VCO [70-72].

3.6 Conclusion

In this chapter the theory of FMCW radar has been presented, with a mathematical model for its operation derived. The eigen analysis and system modelling approaches to beat spectrum analysis were analysed and finally some target detection schemes were discussed.

Chapter 4: Improving Fourier based FMCW Beat Spectrum Analysis

4.1 Discrete Fourier Transform

The Discrete Fourier Transform (DFT) is undoubtedly the most used transform in digital signal processing. The DFT is used to calculate the spectrum of signals defined over finite discrete domains (rather than continuous). The Discrete Fourier transform of a signal is given by the expression:

$$X[k]=\sum_{n=0}^{N-1}x[n]\mathrm{e}^{-j2\pi n\frac{k}{N}} \quad k=0,1\ldots N-1 \tag{4.1}$$

where $x[n], \quad n=0\ldots N-1$ is the discrete data set.

The DFT is primarily used for spectral analysis. However, it is also used when the realisation of some mathematical operation is more easily done in the frequency domain or vice versa such as fast convolution, signal filtering or correlation [67].

From (4.1) we can see that each DFT value for an N length data sequence would require N complex multiplies hence requiring N^2 multiplies for the entire DFT calculation which can lead to high computation demands.

In 1965 a fast algorithm for calculating the DFT known as the Cooley-Tukey algorithm [73] was invented by James W. Cooley and John W. Tukey. The Cooley-Tukey algorithm requires $N\log_2 N$ (where N is a power of 2) operations to calculate an N length DFT that would have required N^2 operations from direct implementation. This significantly reduces the number of operation especially when N is large, e.g. for a 1024 length DFT, the direct implementation would require 1048576 operations whereas the Cooley-Tukey algorithm

would require 10240 operations which is significantly smaller. Other algorithms for efficient DFT calculations such as Prime-factor algorithm [74], Bruun's algorithm [75], Rader's algorithm [76] have since followed. The advent of these fast transforming algorithms led to huge developments in digital signal processing. Collectively these efficient algorithms for DFT calculation are known as Fast Fourier Transforms (FFT). The DFT, though computationally efficient when implemented using an FFT, has two major limitations, namely restricted resolution and spectral leakage which are discussed in the next section.

4.2 Limitations of Discrete Fourier Transform

In this section the limitations of using the DFT in calculating the spectrum of discrete time sequences are discussed.

4.2.1 Spectrum Resolution

In a DFT spectrum of a finite sampled signal, the spectrum's resolution is controlled by the frequency at which the signal was sampled at and the duration of the signal. The resolution of the spectrum, Δf is given as the reciprocal of the signal duration i.e. $1/NT\,Hz$ where T is the sampling period of the data burst and N is the number of samples.

$$\Delta f = \frac{1}{NT} \tag{4.2}$$

In Figure 4.1 and Figure 4.2 the difference in resolution for a signal of frequency 2.4 kHz with the same duration but different sampling periods are shown. Although Figure 4.1 and Figure 4.2 show how we might control the spectrum resolution, in reality a larger sampling period might not always be possible due to factors such as hardware limitations.

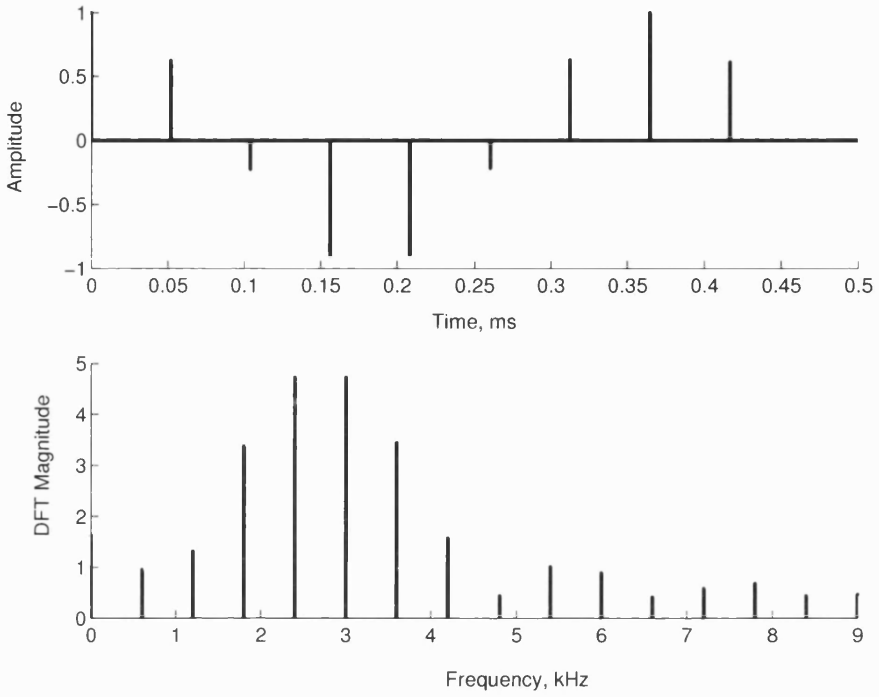

Figure 4.1 Spectrum resolution of a discrete sine wave

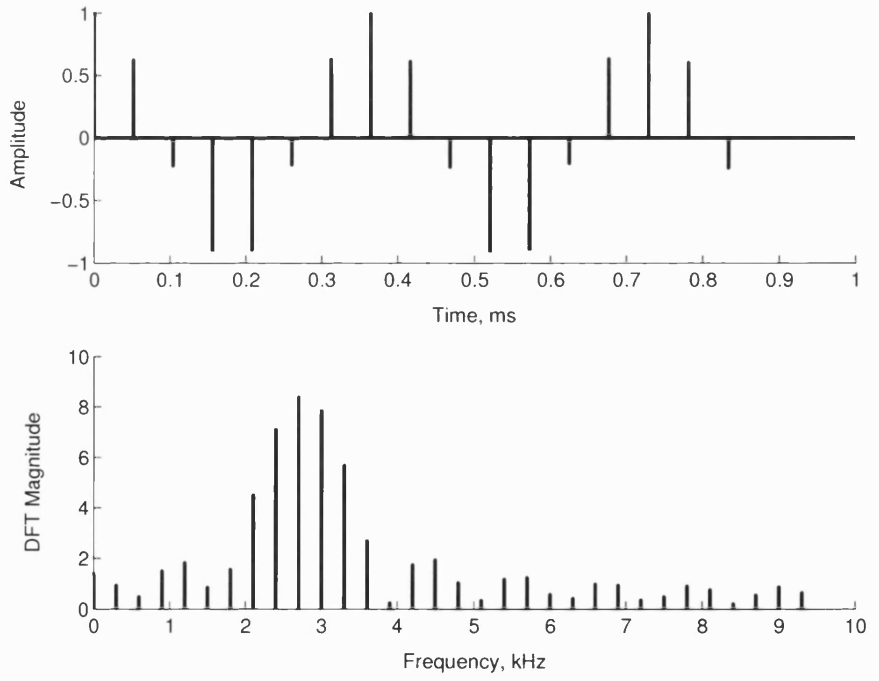

Figure 4.2 Improving spectral resolution by sampling for a longer duration

4.2.2 Windowing and Spectral Leakage

The Fourier transform of a function is defined as an integral between limits of positive and negative infinity. However, in dealing with practical cases such as signals varying with time, we tend to have a finite data set. The approach is then to assume that the data is zero outside the finite data set available and then apply the Fourier transform. Mathematically this is equivalent to representing the function as a product of its continuous form and a rectangular function. Hence the spectrum of a finite sinusoid becomes a convolution between a Dirac pulse at the sinusoids frequency and the spectrum of the rectangular function. This convolution leads to a spread of energy into other frequencies resulting in what are termed as side lobes.

On the other hand spectral leakage occurs when frequency components of a signal are not exact integer multiples of the fundamental frequency of the DFT. Spectral leakage changes both the true amplitudes and positions of frequency components. The affected frequency components, rather than appearing as sharp lines at their true frequencies, appear as a spectrum of frequencies centred on their true frequency positions, in effect giving part of their energy to the nearby frequencies. Figure 4.3 and Figure 4.4 demonstrate spectral leakage with a 3 kHz discrete sine wave. In Figure 4.3 the DFT resolution is a multiple of the fundamental frequency of the signal and hence its spectrum consist of a single peak as expected, whereas in Figure 4.4 the DFT resolution is not a multiple of the fundamental frequency and its spectrum consists of a peak at the fundamental frequency of the signal as well as other smaller surrounding values.

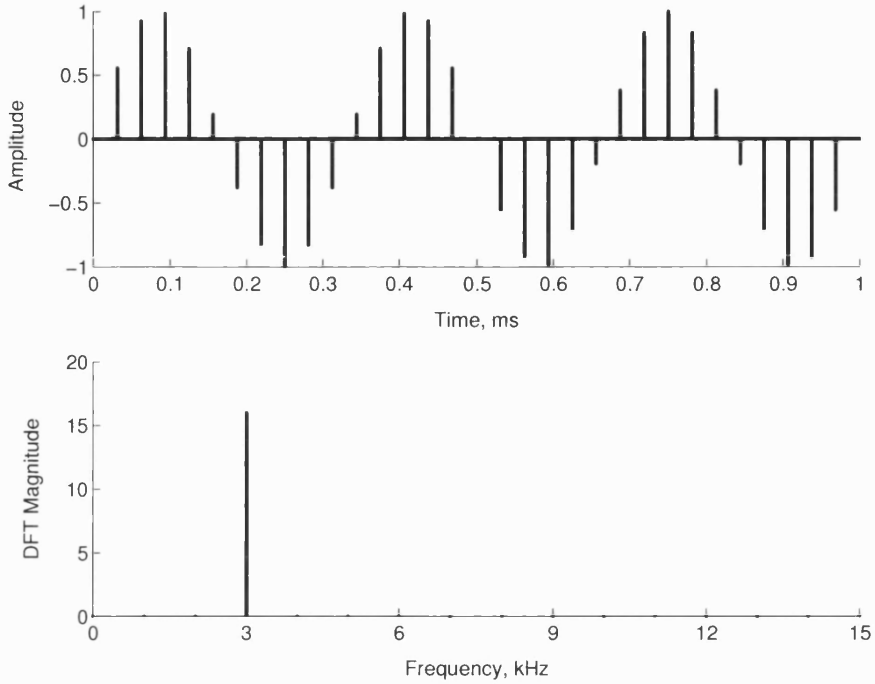

Figure 4.3 Spectrum of signal not suffering spectral leakage

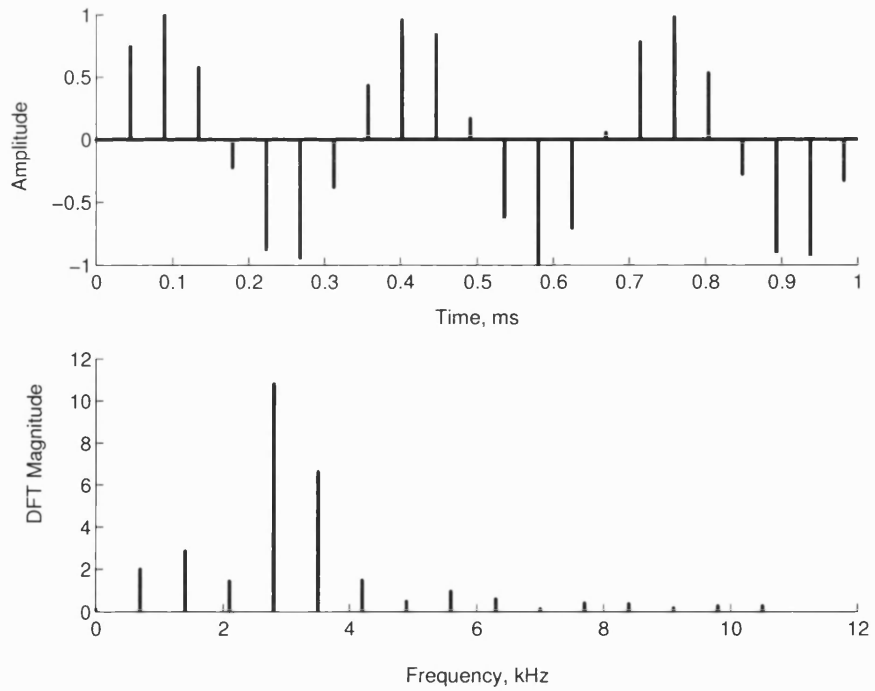

Figure 4.4 Spectrum of signal suffering spectral leakage

Spectral leakage can be combated to an extent by applying special window functions that will minimise the side lobes, which are discussed in the next section. However, the use of window functions comes at the expense of an increased main lobe width, therefore degrading resolution capability and introducing error. Spectral leakage tends to be worst when detecting weak frequency components in the presence of a nearby stronger frequency component.

4.2.3 Window Functions

Windows are special functions used to reduce spectral leakage effects in the Fourier analysis of time limited data by suppressing side lobe levels. In Fourier analysis of time limited data, it is assumed that the signal is periodic with the duration of the signal. If the duration of the signal is not an integer multiple of the period of the signal, the periodic extension assumption will lead to discontinuities as shown in Figure 4.5, which in turn leads to leakage effects in the signal spectrum. Windows are designed specifically to ensure that the transition at the periodic extensions are not abrupt by trying to make the derivative of the boundary points equal to zero or near zero. Equation (4.3) describes the application of a window function $w(t)$ to a signal $s(t)$ with duration τ.

$$s_w(t) = s(t) \times w(t) \qquad 0 \le t \le \tau \tag{4.3}$$

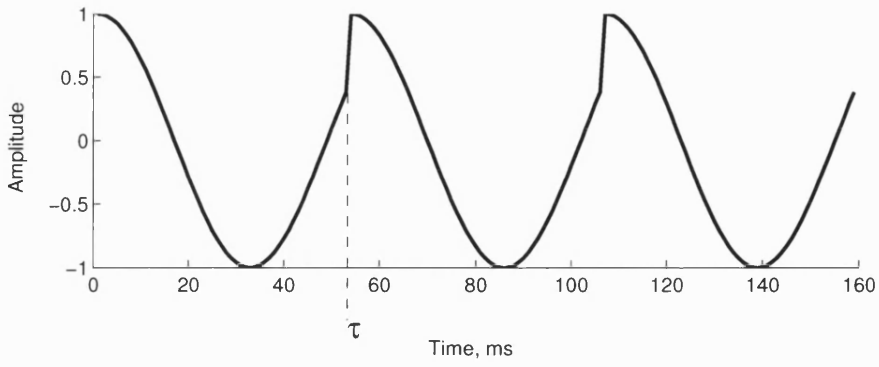

Figure 4.5 Discontinuities in the periodic assumption of the Fourier analysis of finite data

The major drawback to using a window function is an increase in the main lobe width of the signal spectrum, which in turn degrades resolution. In general the lower the side lobe levels, the wider main lobe.

The field of window design remains an active area of research. Over the years, several new window functions have been proposed [77, 78]. Unlike early window function design, where window functions have been developed based on intuition and educative guesses, modern window designs tend to be based on engineering towards an optimal solution.

Window functions generally fall under two categories based on their parameters, namely, fixed windows and adjustable windows. The fixed windows have one parameter, the window length which controls the main lobe width. On the other hand, the adjustable windows have two or more independent parameters, namely, the window length, as in fixed windows, and one or more additional parameters that can control other window characteristics.

The paper by Harris [79] provides an excellent overview of fixed window functions. The vast majority of fixed windows are constructed as weighted sums, products, or convolutions of simple functions or other window functions. For example, the Barltet window is a time domain convolution of two rectangular windows, whereas both the Hann and Hamming windows are shifted sums of the frequency domain representation of the rectangular window.

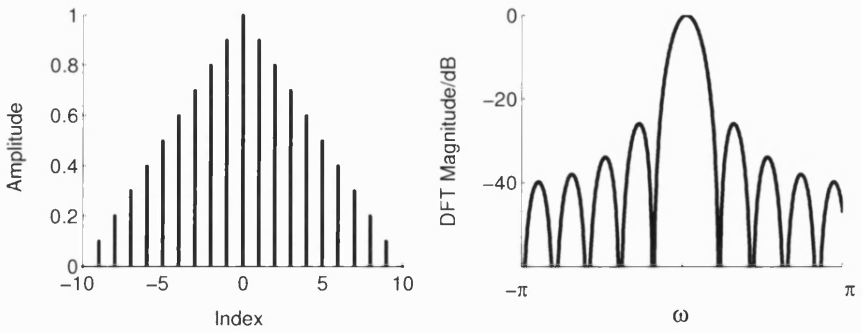

Figure 4.6 Bartlett (triangular) window

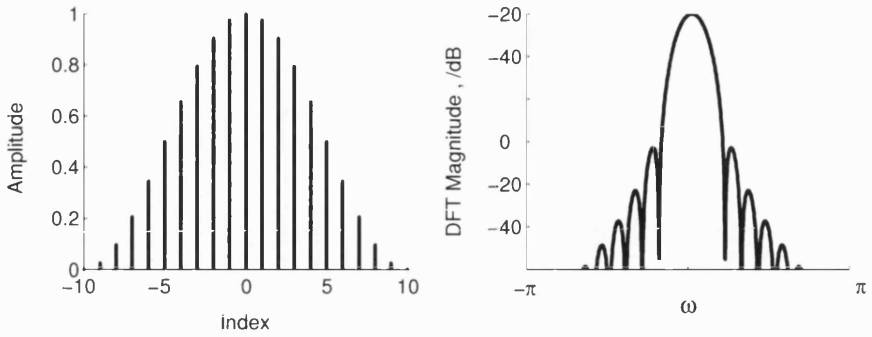

Figure 4.7 Hann window

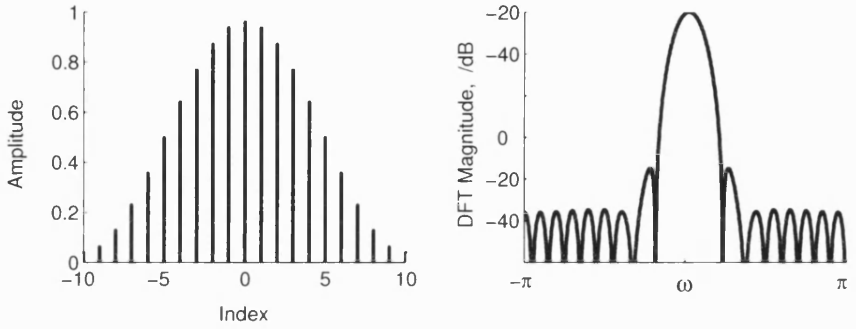

Figure 4.8 Hamming window

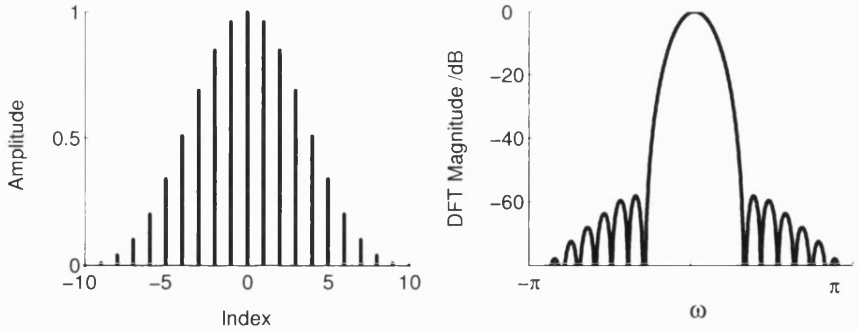

Figure 4.9 Blackman window

Figure 4.6 to Figure 4.9 show some examples of fixed window functions and Table 4.1 shows some of the properties of windows used to compare their performance [79, 80]. As mentioned earlier, the major drawback to using window functions is the increase in the

width of the main lobe as indicated by Table 4.1 and shown in Figure 4.6 to Figure 4.9 which leads to a loss in resolution as indicated by the minimum resolution bandwidth column in Table 4.1, which is a measure of the minimum separation, in units of the spectrum's DFT resolution (see equation (4.2)), of two equal strength frequency components such that their main lobes can be resolved [79].

Window	**Function**	**1st Side lobe level/dB**	**Main lobe width/radians**	**Minimum resolution**
Rectangle	1	-13	$2\pi/\tau$	1.21
Bartlet	$1-2t$	-27	$4\pi/\tau$	1.78
Hann	$cos^2(\pi t)$	-32	$4\pi/\tau$	2.00
Hamming	$.54+.46\cos(2\pi t)$	-43	$4\pi/\tau$	1.81
Blackman	$0.42+0.50cos(2\pi t)$ $+0.08cos(4\pi t)$	-58	$6\pi/\tau$	2.35

Table 4.1 Some common window function properties (τ is the duration of the window function)

On the other hand, adjustable window functions are often derived based on optimality criteria [78]. Dolph's criteria [81] and Kaiser's criteria [82] are two of the most popular optimality criteria used in adjustable window design. Dolph's criteria aims to minimize the main lobe width with the constraints of a fixed window length and side lobes not exceeding a certain level. The window functions resulting from Dolphs criteria are described by the Chebyshev polynomials [81]. Dolph windows have the unique property of constant side lobe levels for all side lobes and hence have no side lobe roll off.

Similarly, Kaiser's criteria aims to minimize the main lobe width with the constraints of a fixed window length and the energy in the side lobes not exceeding a certain percentage of the total window energy. The Kaiser family of windows resulting from the solution to Kaisers optimization problem are approximated by the modified Bessel function of order zero [83]. More recently, the author in [84] proposed a family of minimum side lobe energy windows for filter design which provide a better approximation to the Kaiser

criteria. The windows are shown to have slightly better performance than the original Kaiser windows and are easier to implement.

The adjustable windows tend to have better side lobe suppression capabilities depending on the specific parameters used. For example, a Kaiser window with a length of 41 samples and control parameter of 12, has a 1st side lobe level of -90 dB but has a main lobe width 4 times that of a rectangular window [67].

4.3 Improving DFT Resolution using Superimposition

This research project looked into ways of improving the resolution of the DFT. The result was a technique based on superimposing multiple analyses of the same data set followed by averaging.

A technique was sought that places nulls in the frequency spectrum of a finite duration signal that suffers from spectral leakage. In [85-87] adjustable window functions are presented that have the ability to place a deep dip centred on a particular frequency. The windows achieved side lobe levels similar to a Blackman window and main lobe widths similar to a Hann window.

The synthesis of the technique developed in this project was based on intuition and to an extent satisfying an optimality criteria. It was observed that by taking the product of two sinc functions centred on the same position but with different main lobe widths, a new sinc like function is created with a different side lobe pattern. The next step was to develop a method that would minimize the new side lobe patterns. Equation (4.4) defines the problem around which the technique was developed. The aim was to minimise the energy over the width of the ith side lobe.

$$Minimise \int_{i}^{i+1} sinc(x)sinc(\alpha x)dx \tag{4.4}$$

Where $sinc(x) = \frac{sin(\pi x)}{\pi x}$.

The rest of this section presents the theory behind the technique and the steps involved.

4.3.1 Side Lobes in a DFT Spectrum and Signal Duration

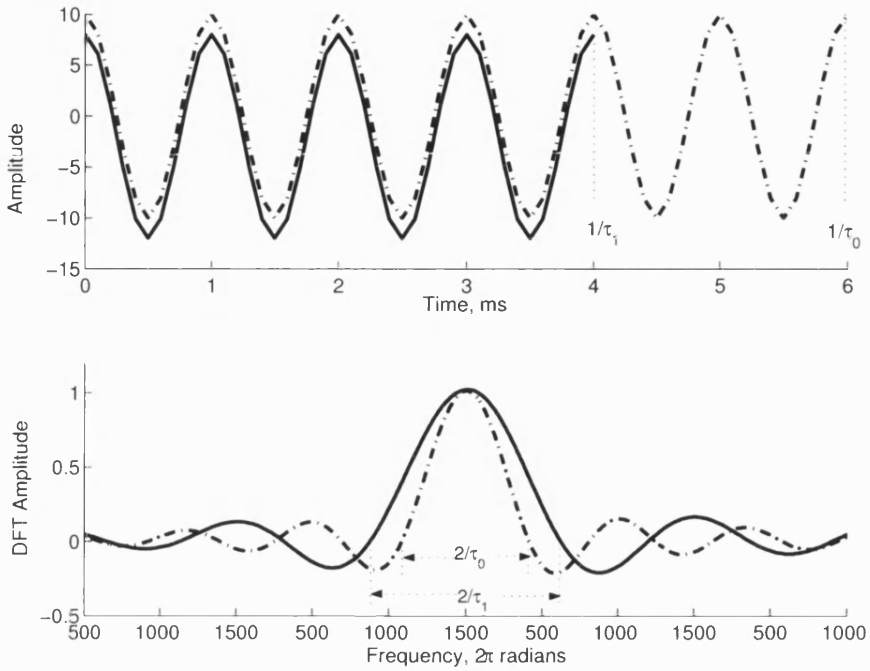

Figure 4.10 Spectrum of signals with same frequency but different durations

Figure 4.10 shows the DFT spectrum of 2 signals of the same frequency but different durations. The main lobe position is always determined by the signal frequency whereas the zero crossings of the main lobe hence the zero crossing width[1] of the main lobe and positions of the side lobes, are determined by the duration of the signal, τ_i. The side lobes occur at intervals of $1/\tau_i$, from the centre of the main lobe, meaning that by altering the duration of the signals the positioning zero crossings in the spectrum could be controlled without altering the position of the main lobe. The dependence of the positioning of the zero crossings in a DFT spectrum on signal duration forms the basis of the signal processing technique which has been named the superimposition technique.

The superimposition technique involves suppressing successive side lobes in the DFT spectrum of the original signal into equal width side lobes by superimposing the DFT

[1] The zero crossing width of the main lobe refers to the amount of separation between the zero crossing bounds of the main lobe.

spectrum of the original signal with DFT spectra of the same signal but with different main lobe widths.

For a sine wave of finite duration, τ_0 and frequency ω_0 ($\omega_0 = 2\pi f_0$) (4.5), its corresponding Fourier Transform is a sinc function ($sin[\pi x]/\pi x$) described by (4.6).

$$s_0(t) = A\sin(\omega_o t) \times rect\left\{\frac{t}{\tau_0} - \frac{\tau_0}{2}\right\} \tag{4.5}$$

$$S_0(\omega) = \exp(\frac{-j\omega\tau_0}{2})\frac{\tau_0}{2}A\left\{sinc\left[\frac{\omega+\omega_0}{2\pi}\tau_0\right] + sinc\left[\frac{\omega-\omega_0}{2\pi}\tau_0\right]\right\} \tag{4.6}$$

The signal duration is chosen such that the zero crossings of the main lobe coincide with the midpoint of the side lobe being targeted.

The increased width main lobe spectrum can be derived from either truncating the original data, applying a window function to the original data or a combination of both truncation and windowing. The next section describes the truncation ratios required to correctly position the side lobes.

4.3.2 Truncating Signals

Figure 4.10 shows the spectrum of a sinusoid with frequency $\omega_o (= 2\pi f_0, f_0 = 1\,kHz)$ and duration τ_0, the zeros crossing in the spectrum (to the right of the main lobe) occur at $\omega_o + 2\pi/\tau_0$, $\omega_o + 4\pi/\tau_0$, $\omega_o + 6\pi/\tau_0$ and so on. In general the ith zero crossing will occur at:

$$\omega_i = \omega_o + 2\pi i/\tau_0 \tag{4.7}$$

We can also see from Figure 4.10 that the ith side lobe is bounded by the ith zero crossing and the (i+ 1)th zero crossings i.e. $\omega_o + 2\pi i/\tau$ and $\omega_o + 2\pi(i+1)/\tau$. The exact midpoint of the ith side lobe will then be

$$\begin{aligned}\omega_{mid-point} &= \omega_i + \frac{1}{2}\left[\omega_{i+1} - \omega_i\right] \\ &= \frac{1}{2}\left[\omega_{i+1} + \omega_i\right] \\ &= \frac{1}{2}\left[\left(\omega_o + \frac{2\pi(i+1)}{\tau_0}\right) + \left(\omega_o + \frac{2\pi i}{\tau_0}\right)\right] \\ &= \omega_o + \frac{2i+1}{2\tau_0}\end{aligned} \tag{4.8}$$

Therefore for a signal with frequency ω_o and duration τ_i to have its 1st zero crossing at midpoint of the ith side lobe of a signal with frequency ω_o and duration τ_0 , its duration τ_i must be such that:

$$\begin{aligned}\omega_0 + \frac{2\pi}{\tau_i} &= \omega_{mid-point} \\ \omega_0 + \frac{2\pi}{\tau_i} &= \omega_o + \frac{2\pi(2i+1)}{2\tau_0} \\ \tau_i &= \frac{2}{2i+1}\tau_0\end{aligned} \tag{4.9}$$

Therefore to target the ith side lobe using the fraction of the original data duration used is

$$k_i = \frac{2}{2i+1} \tag{4.10}$$

4.3.3 Truncating Signals with Window Functions

In the overview of window functions provided in section 4.2.3, it was shown how the use of window functions led to a loss in resolution through increased main lobe widths. However, as the superimposition technique is based on altering the widths of the main lobe in signal spectra, this disadvantage is used to the benefit of the technique. By applying a window function to the data initially, it means that side lobes can be targeted using a

smaller truncation ratio with the additional benefit of side lobe suppression. The Hann, Hamming and Bartlet windows have zero crossing main lobe widths double that of the rectangular window which means that we could reduce the amount of data discarded by a half, whereas the Blackman window on the other hand triples the zero crossing main lobe width thereby allowing us to reduce the amount of data discarded by a third.

For the Hann, Hamming and Bartlet windows that stretch the main lobe by a factor of 2, to target the i^{th} side lobe using the combination of any of these windows, the data is truncated (before applying the window function) by :

$$k_i = \frac{4}{2i+1} \tag{4.11}$$

For the Blackman window that stretches the main lobe by a factor of 3, to target the i^{th} side lobe using the combination of any of this window, the data is truncated by:

$$k_i = \frac{6}{2i+1} \tag{4.12}$$

The windows considered were chosen due to their ease of implementation and this does not prevent the use of other windows in the technique as long as the ratio of the zero crossing main lobe width to rectangular window zero crossing main lobe width is correctly reflected when truncating data.

Figure 4.11 compares the superimposition spectrums where the 2^{nd} side lobe is targeted using truncation and various windows. Figure 4.11 appears to show little difference in the level of side lobe suppression on the 2^{nd} side lobe by the various windows. However, there is a difference in the other side lobes not targeted. As expected the other side lobes in the truncation-only spectrum are highest followed by the Bartlett, Hann and Hamming versions. Also, all but the Bartlett version have side lobes merged together.

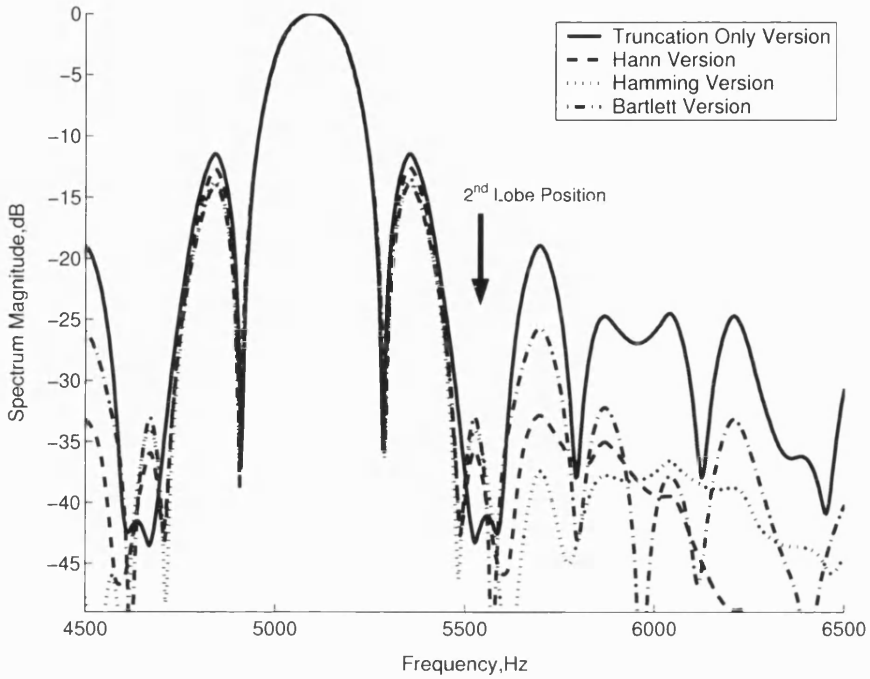

Figure 4.11 Targeting 2nd side lobe with truncation and windowing

4.4 Algorithm

Figure 4.12 shows the steps involved in the proposed algorithm. The algorithm is broken into four parts which are discussed next

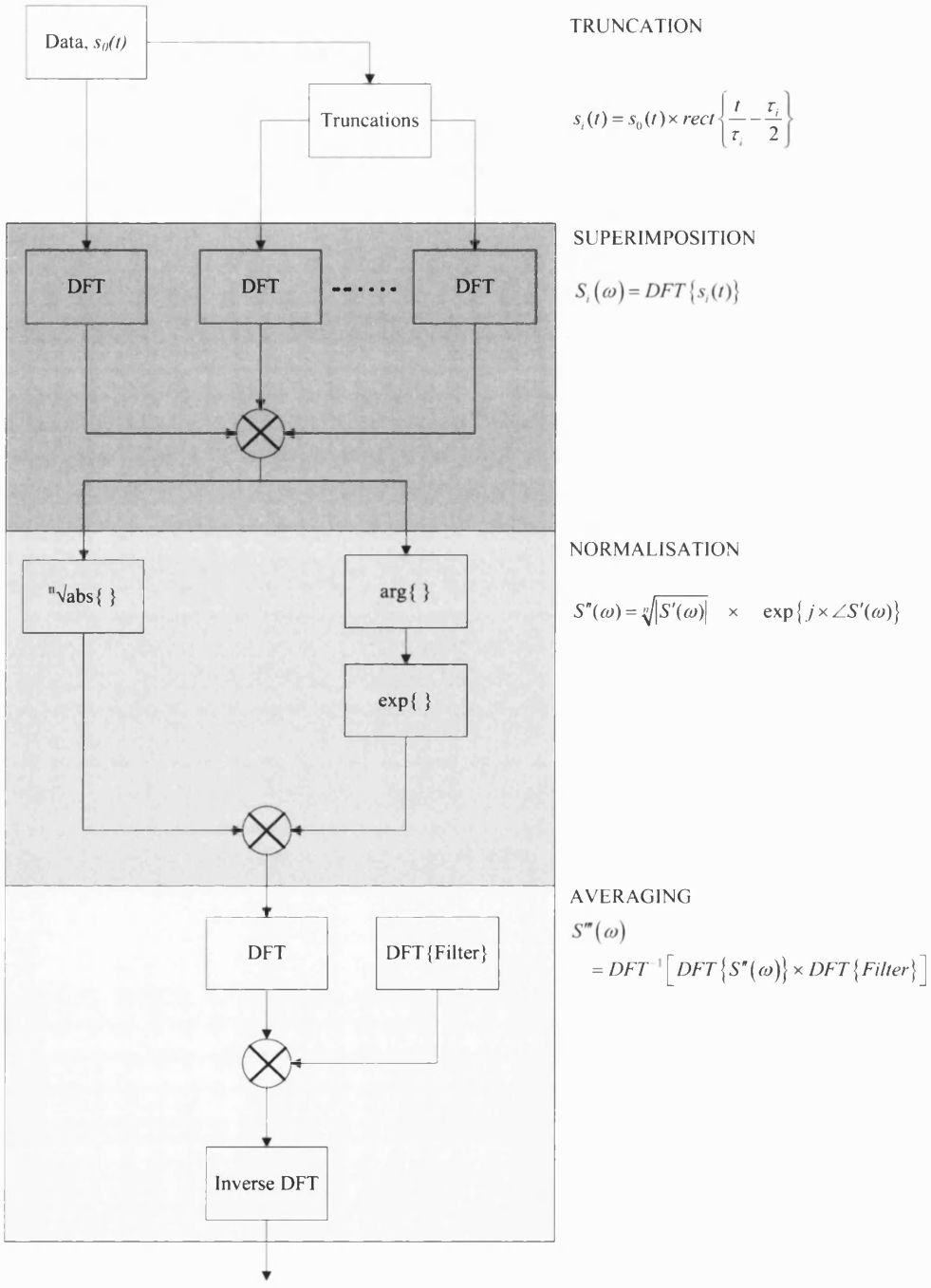

Figure 4.12 Superimposition technique steps

4.4.1 Truncation

The first step in the algorithm is obtaining the data sets from the original data. Depending on the side lobes being targeted, the truncation ratios are chosen using (4.10), (4.11) or (4.12). Equation (4.13) describes the truncation where the i^{th} side lobe is being targeted.

$$s_i(t) = s_0(t) \times rect\left\{\frac{t}{\tau_i} - \frac{\tau_i}{2}\right\} \tag{4.13}$$

Where $\tau_i = k_i \tau_0$, k_i is (4.10), (4.11) or (4.12) and $s_o(t)$ is (4.5).

4.4.2 Superimposition

Equations (4.14) and (4.15) describe the second step in the algorithm. This step is where the spectra of the original data set and the derived data sets are superimposed. Equation (4.14) describes the Fourier transform of the data sets to be superimposed and (4.15) describes the superimposition which is a product of the spectra.

$$S_i(\omega) = \exp(\frac{-j\omega\tau_i}{2})\frac{\tau_i}{2} A\left\{sinc\left[\frac{\omega+\omega_0}{2\pi}\tau_i\right] + sinc\left[\frac{\omega-\omega_0}{2\pi}\tau_i\right]\right\} \tag{4.14}$$

Where A is the amplitude of the original signal, $s_o(t)$.

$$S'(\omega) = \prod_{i=0}^{n} S_i(\omega) \tag{4.15}$$

Where n is the index for the spectra of the truncated data sets with $n = 0$ representing the spectrum of the original signal.

4.4.3 Normalisation

The third step is the normalisation step. The Fourier transforms in (4.14) introduces a scaling factor τ_i and the multiplication in (4.15) results in a A^n factor and a

factor $\prod_{i=0}^{n} \tau_i \exp(-j\omega\tau_i/2)$. Hence the normalisation step described by (4.16) is required to maintain relative strengths between the frequency components in the signal and remove the complex factor in the spectrum. Note how $S'(\omega)$ is separated into its magnitude and phase, this is important as the phase relationship between the truncated signals is what the averaging step described next depends on.

$$S''(\omega) = \sqrt[n]{|S'(\omega)|} \times \exp\{j \times \angle S'(\omega)\} \times \prod_{i=0}^{n} \frac{1}{\tau_i} \exp\left(\frac{j\omega\tau_i}{2}\right) \tag{4.16}$$

4.4.4 Averaging

In the Fourier transform spectrum of a finite sinusoid successive side lobes in the spectrum will have a phase pattern of $\rho + \pi$, ρ, $\rho + \pi$, ρ, $\rho + \pi$ and so on where ρ is a first order linear equation. The linear equation ρ comes from a complex factor introduced in the spectrum due to the finite and causal nature of the signal whereas the π part comes from the sinc function alternating between sets of negative and positive value in successive lobes. For example the spectrum function (4.14) has a complex factor $\exp(-j\omega\tau_i)$, if this factor is removed as is done in the normalisation step of the technique, (4.14) becomes (4.17), therefore when (4.17) is negative, its phase is π, when it is positive its phase is 0.

$$S(\omega) = \frac{\tau_i}{2} A \left\{ sinc\left[\frac{\omega + \omega_0}{2\pi}\tau_i\right] + sinc\left[\frac{\omega - \omega_0}{2\pi}\tau_i\right] \right\} \tag{4.17}$$

As the lobes alternate between negative and positive values as shown in original signal spectrum trace of Figure 4.13, the phase of the lobes will alternate between π and 0. The resulting side lobes from a targeted side lobe after superimposition will also follow a similar pattern as shown in the product of spectrums trace of Figure 4.13, where the 1st and 2nd side lobes are targeted. Averaging over the width of 2 successive side lobes (i.e. a negative and a positive lobe) will therefore have a cancellation effect over the side lobes. As the exact positions of the lobes are unknown the averaging is performed using a

uniform moving average filter [88]. The moving average filtering is a convolution described by

$$S'''(\omega) = S''(\omega) * G(\omega) \equiv \int_0^{\omega} S''(\varphi) G(\omega - \varphi)\, d\varphi \tag{4.18}$$

where $G(\omega) = 1/\tau_0\, rect\{\omega\tau_0\}$, $1/\tau_0$ being the width of a side lobe in the original signal.

The actual implementation is done via a series of Fourier transforms using the convolution theorem [80] as described by (4.19)

$$S'''(\omega) = FT^{-1}\left[FT\{S''(\omega)\} \times FT\{G(\omega)\}\right] \tag{4.19}$$

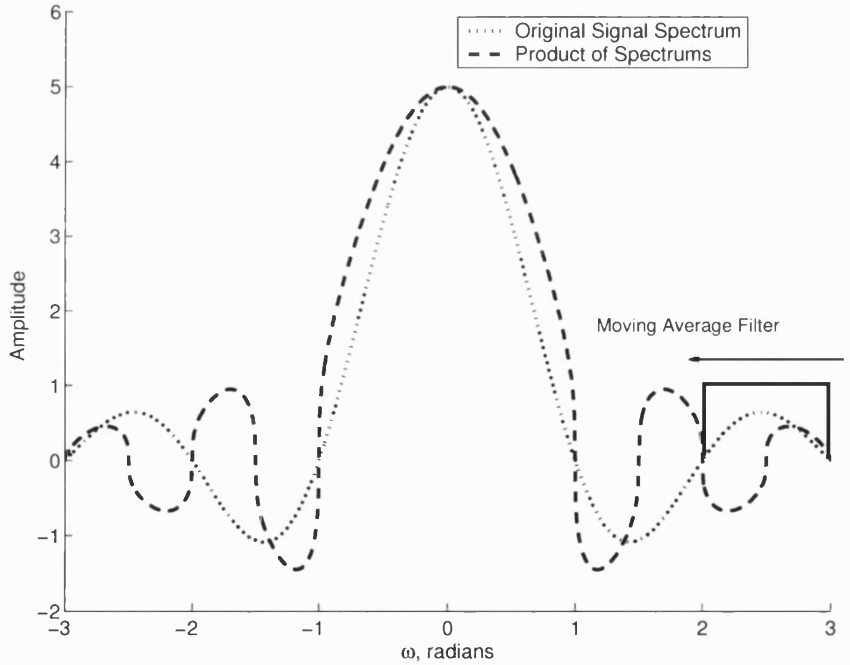

Figure 4.13 Applying averaging filter to product of spectrums

So far the processing technique has been described for a single frequency signal. However, the processing technique described is linear, therefore using linear superimposition the technique can be applied to a multi-frequency signal.

4.5 Discussion

In this section some general issues regarding the technique are discussed.

4.5.1 Technique Variations

In applying the technique there are various scenarios possible. The scenarios include targeting a single side lobe in a spectrum, targeting a succession of side lobes, targeting side lobes by pure truncation or targeting side lobes with truncation in conjunction with windowing. Table 4.2 lists the truncations required for the first four side lobes depending on the approach to be used. The doubling windows include the Hann, Hamming and Bartlet windows whose zero crossing main lobe widths are doubled (see Table 4.1) whereas the tripling window refers to the Blackman window whose zero crossing main lobe width is tripled

Side lobe	Pure Truncation	Truncation with doubling window	Truncation with Tripling window
1st	2/3	--	--
2nd	2/5	4/5	--
3rd	2/7	4/7	6/7
4th	2/9	4/9	2/3
5th	2/11	4/11	6/11

Table 4.2 Data truncation ratios

4.5.2 Breaking a Side Lobe into an Even Number of Side Lobes

Another approach considered was to generalise the technique by breaking a side lobe into an even number of smaller lobes. To break a side lobe into N smaller side lobes we would require $N-1$ truncated versions of the original signal. The 1st zero crossing positions of each

of the truncated signals will be equally spaced across the side lobe being targeted so that the resulting side lobes are of equal width (4.20).

$$\omega_{\Delta} = \frac{2\pi}{\tau_0} \times \frac{1}{N} \tag{4.20}$$

Where τ_o is the duration of the original signal and N is the number of resulting side lobes and N is even.

When breaking the ith side lobe into N side lobes using N-1 truncated signals, the zero crossing of the nth truncated signal will be at:

$$\omega_{crossing-n} = \omega_0 + \frac{2\pi i}{\tau_0} + n\omega_{\Delta} \tag{4.21}$$

This gives the duration of the nth truncated signal required as

$$\begin{aligned} \tau_{i-n} &= \frac{2\pi}{\omega_{crossing-n} - \omega_0} \\ &= \tau_0 \frac{1}{i + n/N} \end{aligned} \tag{4.22}$$

Therefore, it follows that the truncation ratio in this case for the nth truncated signal when breaking the ith side lobe into N side lobes is

$$k_{i-n} = \frac{1}{i + n/N} \tag{4.23}$$

The averaging filter will still average over the width of 2 successive resulting smaller lobes but the filter width is now dependent on the total number of resulting smaller lobes, i.e. N. In this case the averaging filter described earlier by equation (4.18) becomes

$$\begin{aligned} G(\omega) &= \frac{1}{2N} \times \frac{2\pi}{\tau_o} rect\{\omega\tau_0\} \\ &= \frac{\pi}{N\tau_o} rect\{\omega\tau_0\} \end{aligned} \tag{4.24}$$

Figure 4.14 and Figure 4.15 show the averaging filter in the cases where the 2nd side lobe is broken into 4 and 6 smaller side lobes respectively.

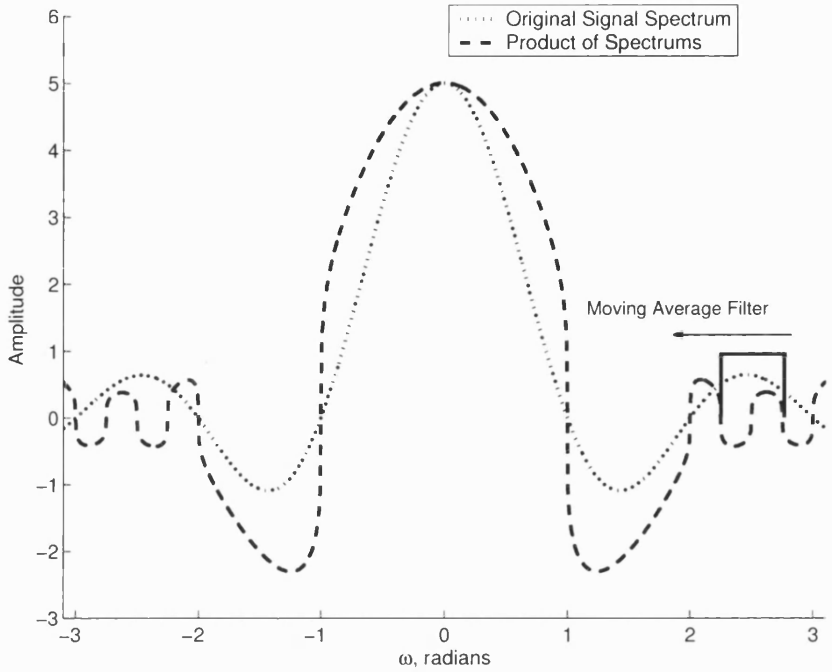

Figure 4.14 Applying a moving average filter when breaking a side lobe into 4 smaller lobes

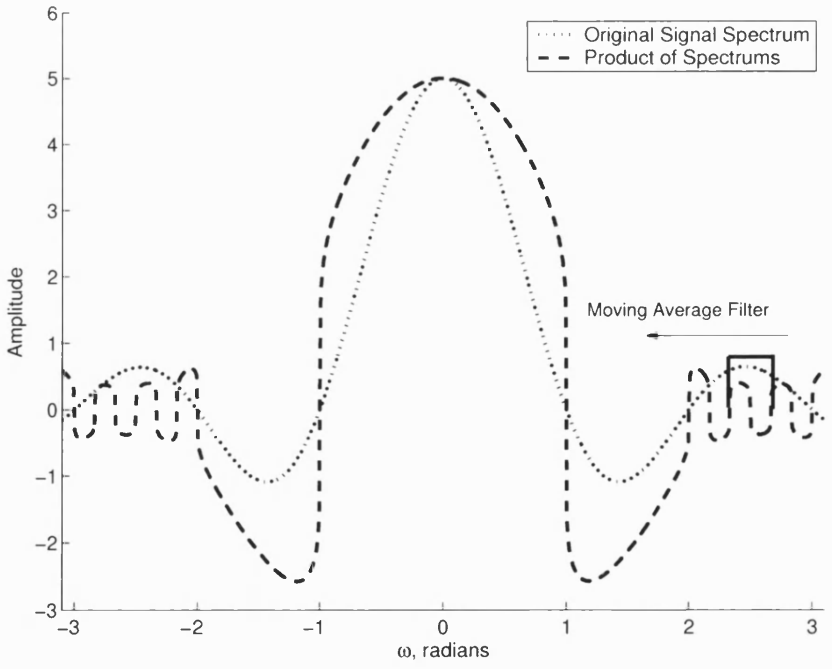

Figure 4.15 Applying a moving average filter when breaking a side lobe into 6 smaller lobes

Figure 4.16, Figure 4.17 and Figure 4.18 show the spectrums where the 1st, 2nd and 3rd side lobes of a simulated sine wave with frequency 5.1 kHz and duration 5.8 milliseconds are targeted by breaking the side lobe into 2, 4 and 6 smaller lobes respectively. In Figure 4.16 where the 1st side lobe is targeted, there appears to be no difference in main lobe widths of the 2 lobe, 4 lobe and 6 lobe traces. However, it appears as further side lobes are targeted the main lobes in the 4 lobe and 6 lobe traces increase in size hence resulting in poorer resolutions, as shown in Figure 4.17 and Figure 4.18. Overall, in all cases it appears that targeting a side lobe by breaking it into 2 smaller lobes results in the best side lobe suppression. For the remainder of this report all superimpositions spectrums will refer to the case where a side lobe is broken into 2 smaller lobes

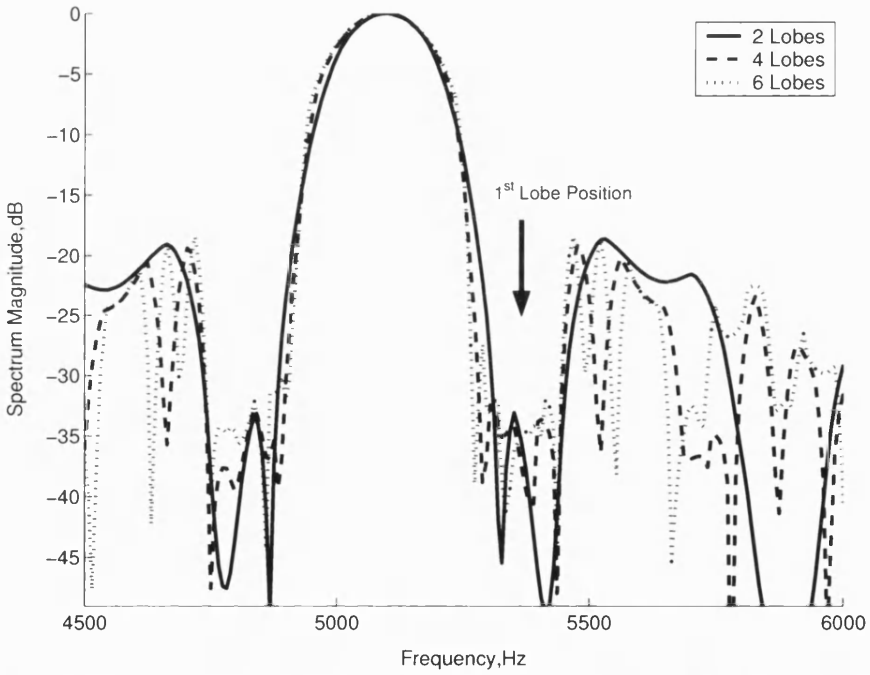

Figure 4.16 Targeting 1st side lobe by breaking side lobe into an even number of smaller lobes

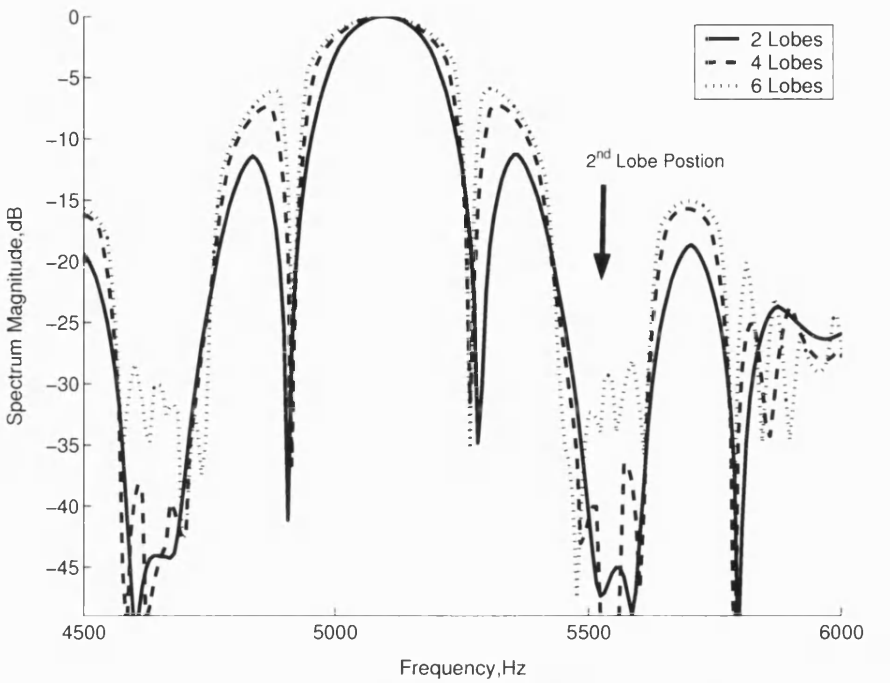

Figure 4.17 Targeting 2nd side lobe by breaking side lobe into an even number of smaller lobes

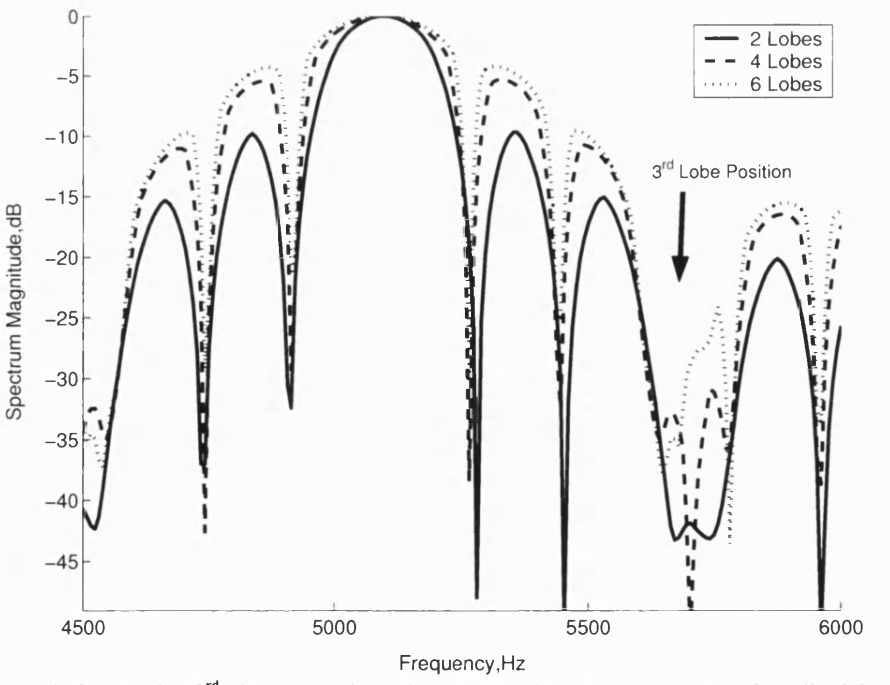

Figure 4.18 Targeting 3rd side lobe by breaking side lobe into an even number of smaller lobes

4.5.3 Other Side Lobes Targeted

Due to the periodic nature of the side lobes in a *sinc(πx)* function, targeting a side lobe using the superimposition technique results in other side lobes being targeted when ever a midpoint of a side lobe in the original signal spectrum coincides with a zero crossing position in the truncated signal spectrum. For example, when we target the 1st side lobe the original spectrums 1st to 4th side lobe midpoints (see equation (4.8)) are at $3/2\pi$,$5/2\pi$, $7/2\pi$ and $9/2\pi$ whereas the zero crossings of the truncated spectrum (see equation (4.7)) are at $3/2\pi$, $6/2\pi$, $9/2\pi$ and so on. The zero crossing of the truncated spectrum at $9/2\pi$ coincides with the 4th side lobe of the original spectrum, therefore this side lobe is also targeted as a result of targeting the 1st side lobe. In Figure 4.19 we can see the original signal DFT, the truncated signal DFT and their product when the 1st side lobe is being targeted. Figure 4.19 also shows not only the 1st side lobe splitting into 2 side lobes as expected but also the 4th and 7th side lobes split into 2 side lobes as well.

In general when targeting the ith side lobe in a $sin(x)/x$ function, the truncated version of the original signal is derived using (4.10) giving the nth zero crossing at:

$$\omega_{crossing-n} = \frac{(2i+1)}{2}\pi n \tag{4.25}$$

In the original signal spectrum, the midpoint of the jth side lobe (see equation (4.8)) is at:

$$\omega_{midpoint-j} = \frac{2j+1}{2}\pi \tag{4.26}$$

Equation (4.26) is a series of successive odd numbers scaled by $\pi/2$. Therefore the zero crossings of the truncated spectrum that coincide with the midpoint of the jth side lobe must be an odd number multiple of $\pi/2$, i.e. $\omega_{crossing-n}$ must be odd. By substituting for n in (4.25) with $(2k+1)$, (4.25) becomes (4.27) i.e. an odd number multiple of $\pi/2$

$$\omega_{crossing-n} = \frac{(2i+1)}{2}\pi(2k+1) \tag{4.27}$$

Therefore if we target the ith side lobe we also will be targeting the j^{th} side lobe, where j is the solution (4.29) of (4.28)

$$(2j+1)\frac{\pi}{2} = (2i+1)(2k+1)\frac{\pi}{2} \tag{4.28}$$

$$j = 2ik + i + k \tag{4.29}$$

(where i is the side lobe targeting initially and k is an integer)

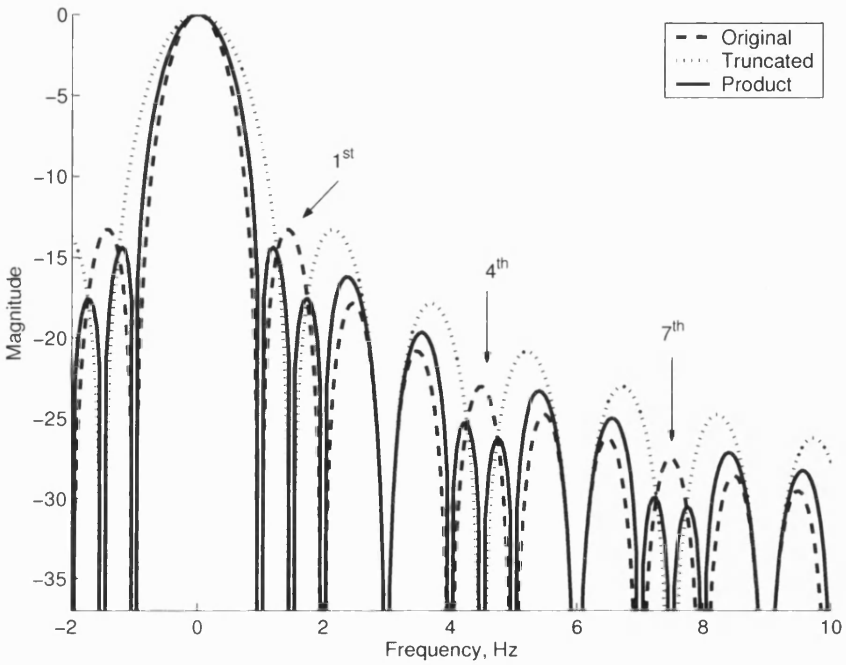

Figure 4.19 Additional side lobes targeting as a result of targeting the 1st side lobe

Table 4.3 lists side lobes targeted as a resulting of targeting the first 3 side lobe in a superimposed spectrum.

Targeted Side lobe	Side lobes Targeted as a result
1st	4th, 7th 10th
2nd	7th, 12th, 17th
3rd	10th, 17th , 24th

Table 4.3 Additional side lobes targeted as a result of targeting a side lobe

4.5.4 Minimum Duration of Signal

Consider a time limited sine wave with frequency f_0, period $T(=1/f_0)$ and duration τ. If the signal duration is a full period i.e. $\tau = T$, the signal spectrum will be a sinc function (see section 4.3.1) with a main lobe centred at f_o, bounded by the zero crossings at $f_o - 1/\tau(=0)$ and $f_0 + 1/\tau(=f_0)$. This implies that the main lobe will just be contained within the useful positive frequency spectrum. This is shown in the Full Cycle trace of Figure 4.20 where the DFT of a sine wave using a dataset containing one period is calculated. On the other hand if the duration of the sine wave is less than the period i.e. $\tau < T$ then the lower boundary of the main lobe will be less than zero i.e. $f_o - 1/\tau < 0$ which implies that main lobe of the spectrum will enter the negative half of the spectrum, in effect the useful positive half appears like a low pass filter. This is also shown in Figure 4.20 where the spectrums of sine waves with duration, $\tau < T$ are shown.

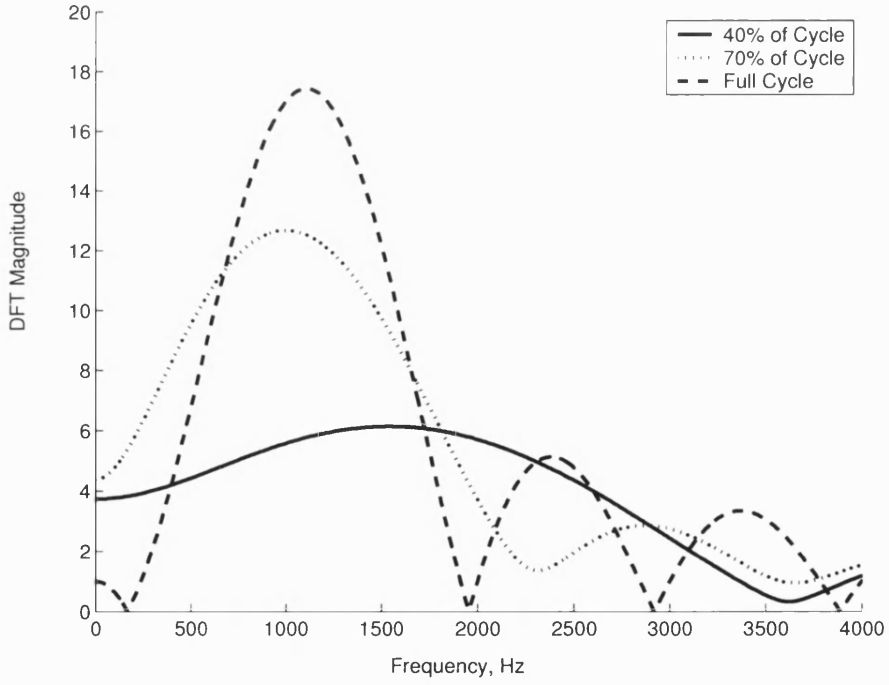

Figure 4.20 Spectrum of signal with different duration

Assuming we know the lowest frequency component, f_{low} , in a time limited signal then we can say that when applying the superimposition technique to such a signal we must ensure that all resulting data set from a truncations must always have durations $\tau_{truncated}$, such that:

$$\tau_{truncated} > 1/f_{lowest} \tag{4.30}$$

That is to say if we have one full period of the lowest frequency component in a signal we are guaranteed to have at least a cycle of the other larger frequency components in the signal. Equation (4.30) is the limiting case and the analysis assumes all signal components are of equal duration, in practice we would like to have a larger minimum duration.

4.5.5 Frequency Components of Unequal Duration

The superimposition technique assumes that all frequency components of the signal being analysed exists for the entire duration of the signal. Potentially a problem arises when a signal consists of frequency components of varying durations as it would result in spectrum where each frequency component has a different main lobe and side lobe width (see section 4.3.1). This could in turn lead to the averaging stage of the technique breaking down as the averaging filter is averaging over the width of a side lobe with the assumption that all components are of equal duration. Figure 4.21 shows a signal composed of 2 equal strength but unequal duration frequency components; the higher frequency component having two-thirds the duration of the lower frequency component. The results of applying the superimposition technique to the signal (Figure 4.21) are shown in Figure 4.22. In the original trace of Figure 4.22 we can already see a sign of distortion as the main lobe width of the shorter duration component is wider and not as strong, whereas the superimposition trace fails to resolve the shorter duration signal. Figure 4.21 and Figure 4.22 demonstrate an extreme case, to reduce the possibility of such a problem occurring, the original signal duration should be as long as possible so that any difference in durations of signal components will be small relative to the durations, which in turn will ensure differences in lobe widths are minimized.

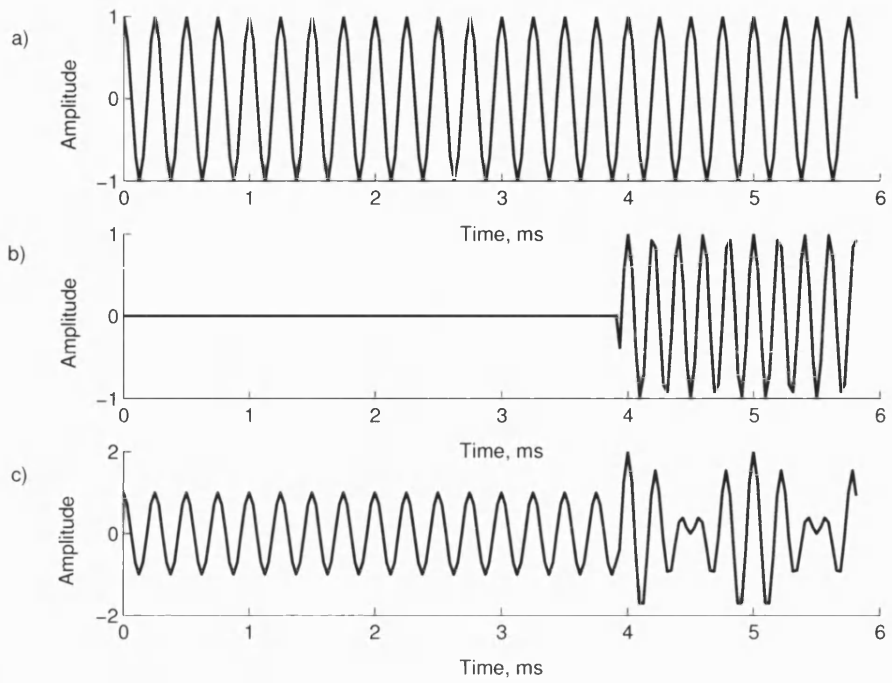

Figure 4.21 Signal Containing Components of Unequal Duration a) Component with duration equal to entire signal duration, b) Component with duration half entire signal duration c) Signal with components of varying duration

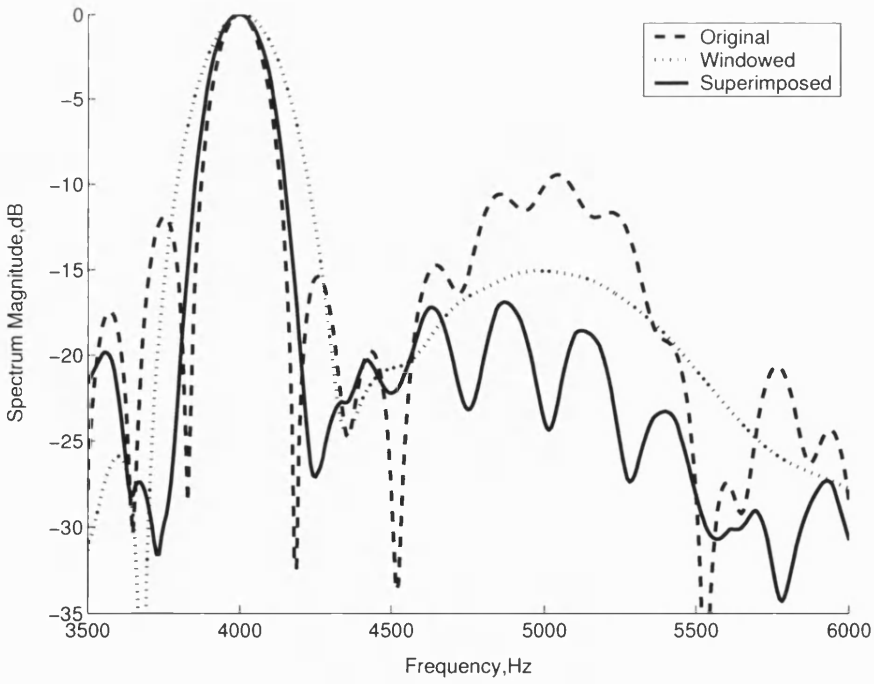

Figure 4.22 Spectrum plots of signals of unequal durations

4.5.6 Alternative Averaging Filters

When a uniform moving average filter is applied to a continuous sine wave with the width of the filter equal to the period of sine wave, the effect is total cancellation. In the case of a *sinc(πx)* function, due to the *1/πx* decay on either side of its main lobe, we do not get total cancellation when we apply a moving average filter over the width of two side lobes. This prompted the investigation of alternative filters with the aim of achieving as close to total cancellation as possible. The idea behind the choice of filters was to compensate for the *1/πx* decay either side of the main lobe of a sinc function. The requirements for suitable filters were:

1. symmetry about their midpoint
2. Zero Phase always

Zero phase implies that all the coefficients of the filter are real and positive. The zero phase requirement is because we already have the phase patterns in the superimposed data which ensure that the side lobes alternate between zero phase and phase π. Figure 4.23 shows the filter functions investigated, these include a raised cosine filter, a double sided exponential filter as well as a triangular filter and a squared raised cosine filter. The raised cosine filters and triangular filter are based on typical window functions [80]. On the other hand, the double sided exponential filter was investigated due to its steep gradient. The results of applying the filters in Figure 4.23 in the filtering stage of the superimposition technique are shown in Figure 4.24.

Another class of filters whereby the zero phase requirement was relaxed was considered. Instead this class of filters provided the alternating zero and π phase patterns required to get the cancellation effect on applying an averaging filter. This also required that the phase of the superimposed data be dropped, as such the normalisation equation, (4.16) , in the superimposition algorithm becomes

$$S''(\omega) = \sqrt[n]{|S'(\omega)|} \times \prod_{i=0}^{n} \frac{1}{\tau_i} \exp\left(\frac{j\omega\tau_i}{2}\right) \tag{4.31}$$

In addition, the filters were required to have each section with a continuous uniform phase to be equal to the smaller lobes resulting from superimposition and the integral value over

the entire width of the filter to be zero. Figure 4.25 and Figure 4.26 shows two of such filters investigated.

Figure 4.25 shows a square wave averaging filter being applied to the superimposition technique variation where a side lobe is broken into 2 smaller lobes, whereas Figure 4.26 shows the superimposition technique variation where a side lobe is broken into three smaller lobes and a shifted top hat averaging filter.

The results of applying the filters in Figure 4.25 and Figure 4.26 to the first side lobe are shown in Figure 4.27 and Figure 4.28 respectively. In both cases severe distortion to the spectrums was experienced with no cancellation on the targeted side lobes.

All the alternative filters considered so far appeared not to give the required cancellation effect expected, therefore it was concluded that the uniform (rectangular) moving average filter was best suited to the technique in its current form.

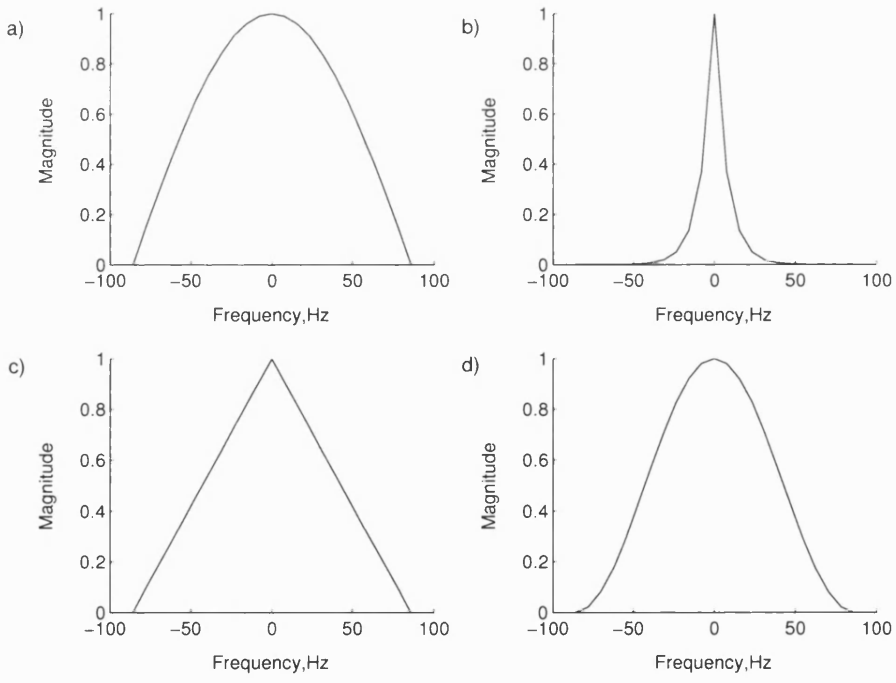

Figure 4.23 Averaging filter functions a) Cosine, b) Double-sided exponential, c) Triangular d) Squared cosine

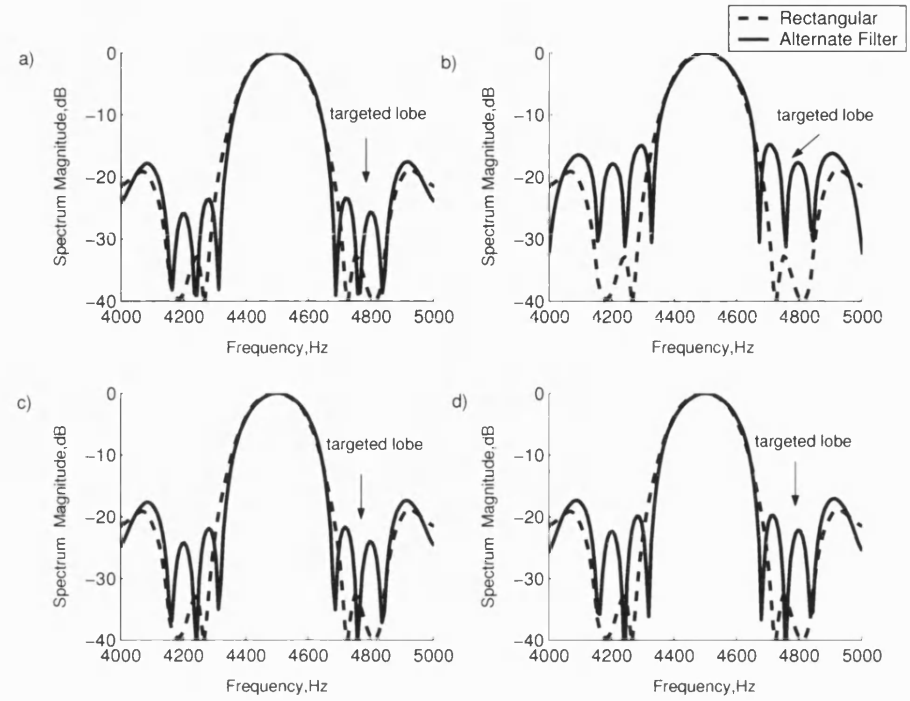

Figure 4.24 Superimposition spectrum plots targeting 1st side lobe for various filter functions a) Cosine, b) Double-sided exponential, c) Triangular d) Squared cosine

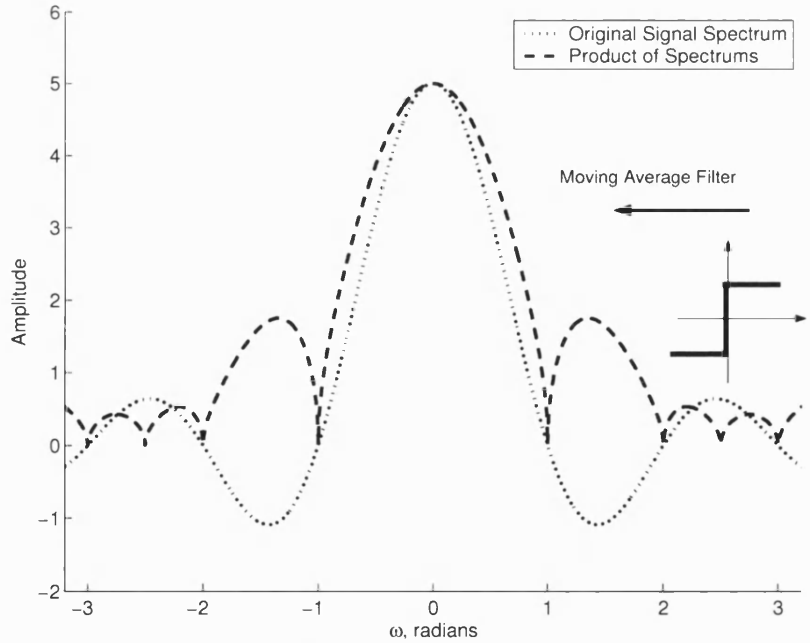

Figure 4.25 Applying a moving average square wave filter

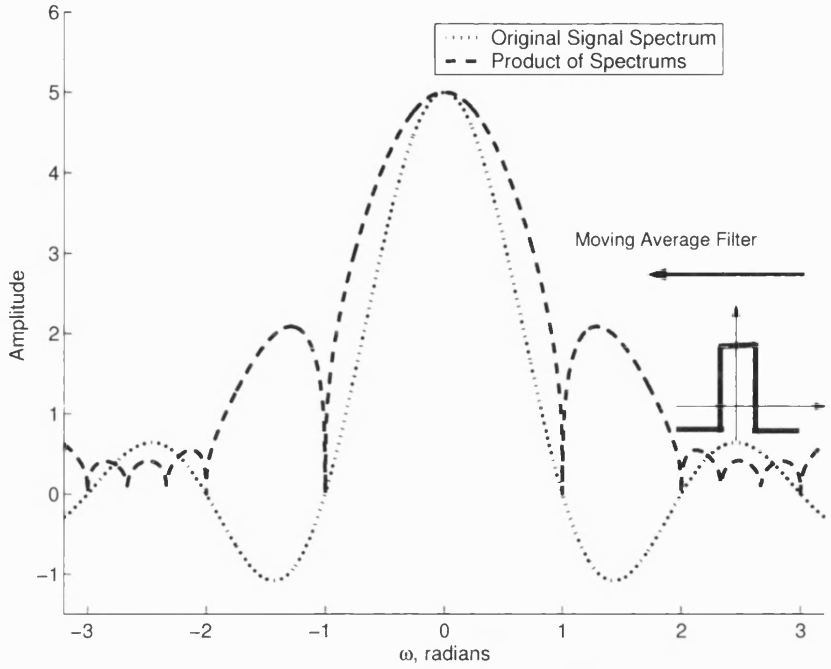

Figure 4.26 Applying a moving average shifted top hat filter

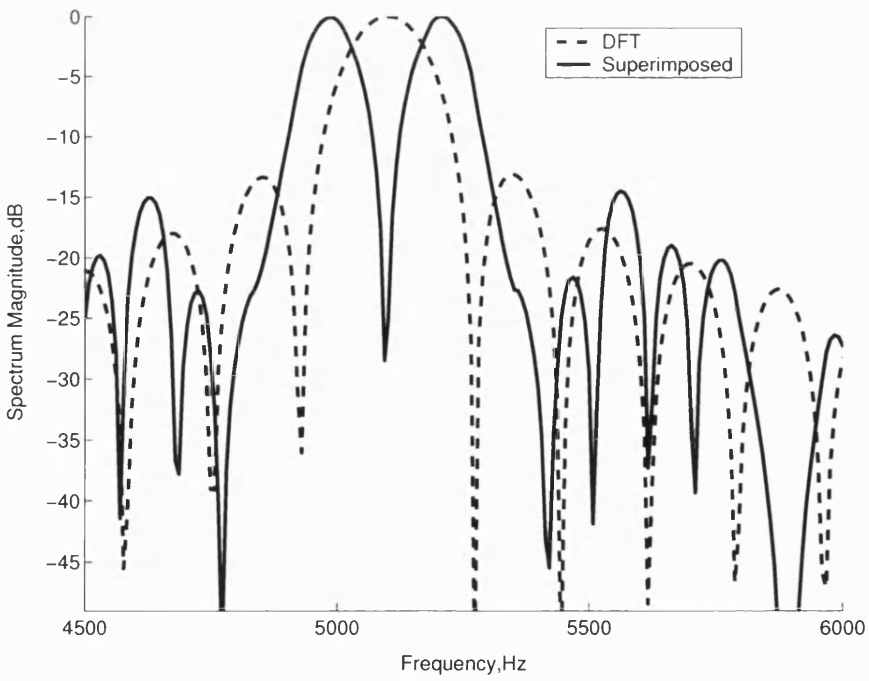

Figure 4.27 Targeting 1st side lobe uisng a square wave avaraging filter

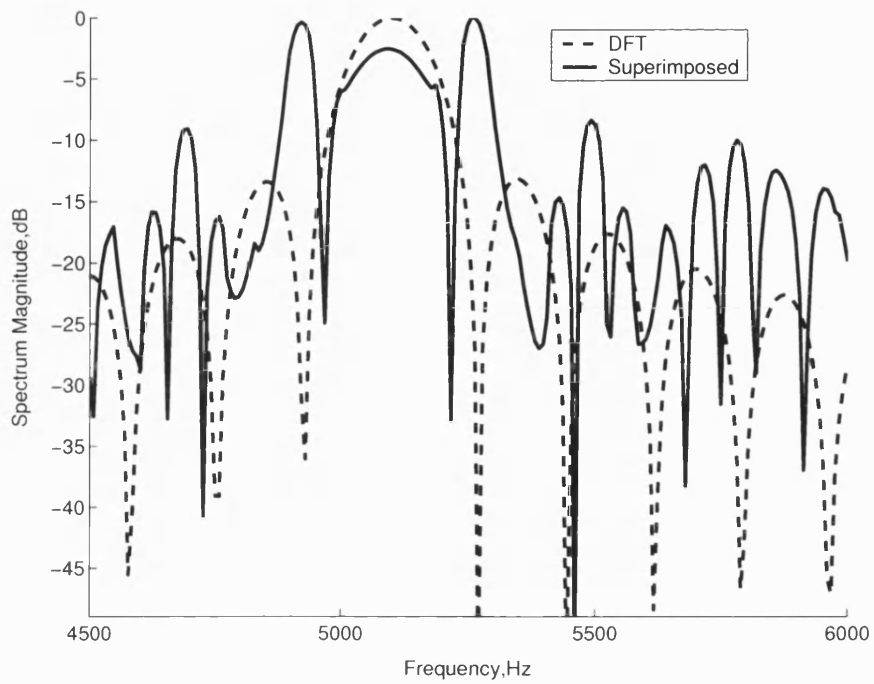

Figure 4.28 Targeting 1st side lobe using a shifted top hat averaging filter

4.5.7 Complexity of Technique

The superimposition technique requires no form of special hardware or computation as it involves only DFT calculations via FFT and array multiplications. The increase in complexity comes from the increase in the number of FFT operations and array multiplications. The operations required for targeting N side lobe are as follows:

1. 1 FFT operation per truncation
2. N-1 array multiplications (where N side lobes are targeted)
3. 2 FFT operations and 1 Inverse FFT operation for averaging

Table 4.4 gives details of the required operations for a few variations of the technique as well as an idea of the average run times of the technique using a 4096 point FFT written in Matlab [89], run on an AMD Athlon 1.8 GHz Desktop PC with 512MB of RAM.

Targeted side lobe	FFT Operations	Array Multiplications	Average run time(ms)
FFT only	1	0	0.85
1^{st} only	5	1	4.2
1^{st} & 2^{nd}	6	2	5
1^{st}, 2^{nd} & 3^{rd}	7	3	6.1

Table 4.4 Operation and timing values for superimposition technique

4.6 Conclusion

In this chapter an overview of the resolution limits and spectral leakage effects encountered in DFT analysis were presented. The use of special window functions to combat spectral leakage was also presented, highlighting the resulting loss in resolution as a consequence of using the window functions. The theory and algorithm for a technique based on superimposition used to combat spectral leakage was then presented. Finally some general issues regarding the superimposition based technique were discussed.

Chapter 5: Results

5.1 Outline

The superimposition technique has been developed to improve DFT frequency analysis, in particular for detecting weak frequencies in the vicinity of a stronger frequency. In this chapter the results of applying the superimposition technique to various forms of data are presented. The performance of the technique is investigated first using simulated data made up of weighted frequency components. The technique is then applied to data generated from simulations of FMCW GPR systems and an experimental GPR representation using a network analyser. Finally the technique is applied to data measured from a prototype FMCW GPR system.

Each result presented is made up of an original trace which refers to data processing with just the DFT, a superimposition trace which refers to data processing using the superimposition technique and a windowed trace which refers to data processing with a window function applied prior to the DFT being applied. In all cases a 4096 point FFT is used to calculate the DFT spectrum unless otherwise mentioned.

5.2 Investigation of Superimposition Technique Performance

In this section the performance of the technique is investigated in the areas of side lobe suppression achieved and detection of low-level amplitude signal components.

5.2.1 Side lobe Suppression

In this section the side lobe levels of the superimposition technique are investigated. The side lobe levels based on an analytical approximation of the technique are predicted followed by measurements using simulated data.

Equations (5.1) to (5.3) define an analytical approximation of the technique based on targeting a single side lobe at a time using two ideal sinc functions. Equation (5.2) describes the signal truncation and (5.3) describes the superimposition and averaging over the width of a side lobe in (5.1).

$$f(x) = sinc(x) \tag{5.1}$$

Where $sinc(x) = \frac{sin(\pi x)}{\pi x}$

Step 1: Truncation to target side lobe n

$$f_n(x) = sinc(\alpha x) \tag{5.2}$$

Where $\alpha = (n + 1/2)^{-1}$

Step 2: Superimposition and Averaging

$$f_{sup}(x) = \int_{x-\frac{1}{2}}^{x+\frac{1}{2}} \left| f(x) f_n(x) \right|^{\frac{1}{2}} dx \tag{5.3}$$

The side lobe peaks in the superimposed function (5.3) will occur at the same position as the side lobe peaks in (5.1). Therefore, to predict the side lobe levels in (5.3), (5.3) is evaluated based on the positions of the side lobe peaks in (5.1). The results are presented in Figure 5.1, where the approximation is applied to target the 1st to 20th side lobes and Table 5.1 where the approximation is applied to target the 1st to 6th side lobes. In all cases, the approximation of the superimposition technique shows significant and increasing improvement as higher side lobes are targeted. To verify the results in Table 5.1 the steps described by Equations (5.1) to (5.3) were simulated, with the results shown in Figure 5.2 to Figure 5.7.

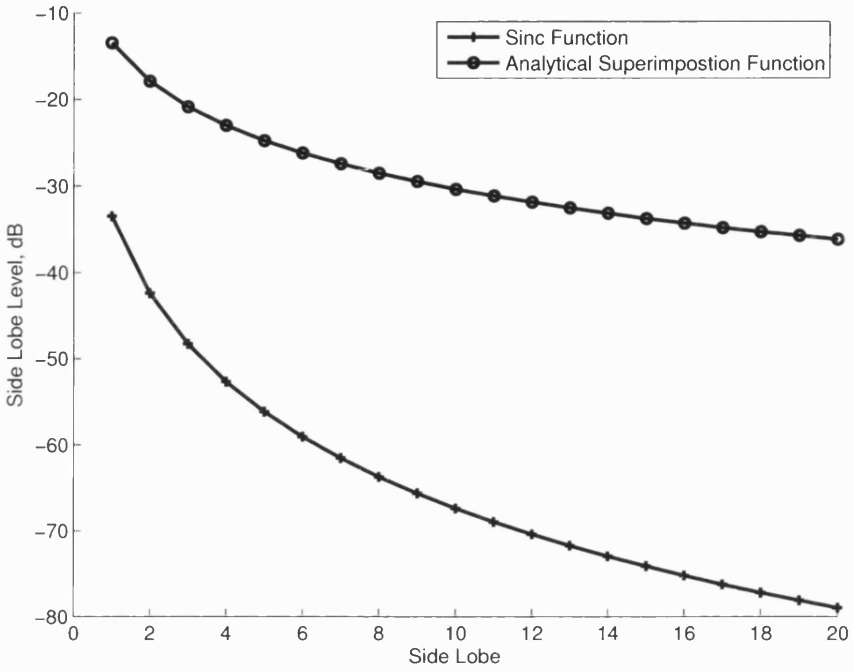

Figure 5.1 Sinc function and analytical approximation of superimposition technique side lobe comparison

Side lobe	DFT side lobe level /dB	Superimposition side lobe level / dB	Improvement /dB
1st	-13.5	-33.5	20
2nd	-17.9	-42.4	24.5
3rd	-20.8	-48.3	27.5
4th	-23.0	-52.6	29.6
5th	-24.8	-56.1	31.3
6th	26.2	-59.0	32.8

Table 5.1 Superimposition technique side lobe levels based on analytical approximation

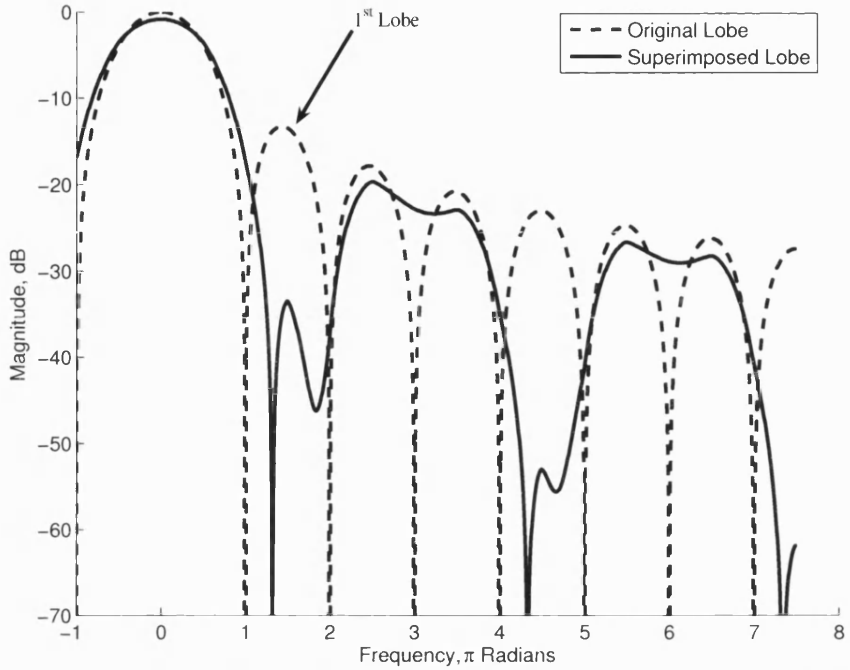

Figure 5.2 Targeting 1st side lobe using analytical approximation to superimposition technique

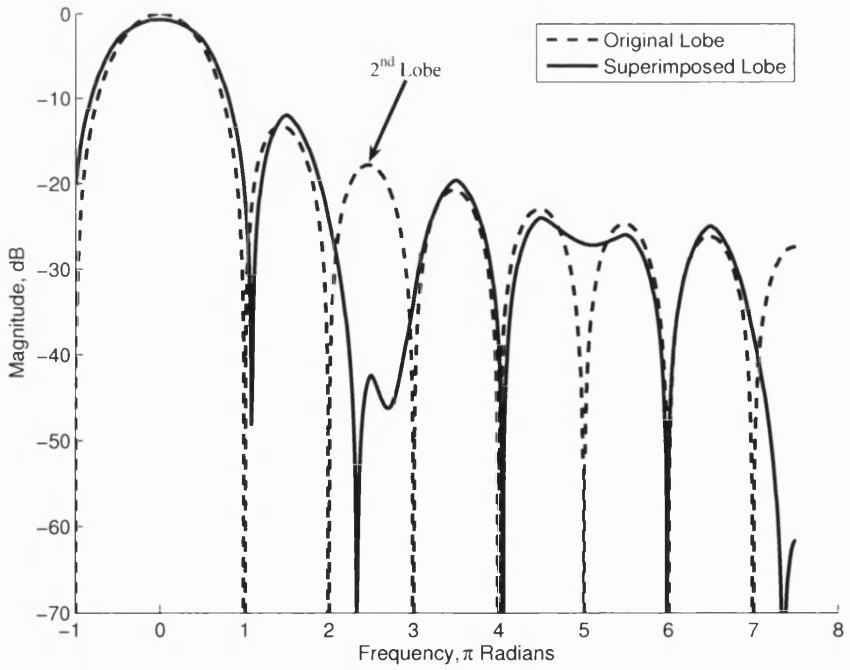

Figure 5.3 Targeting 2nd side lobe using analytical approximation to superimposition technique

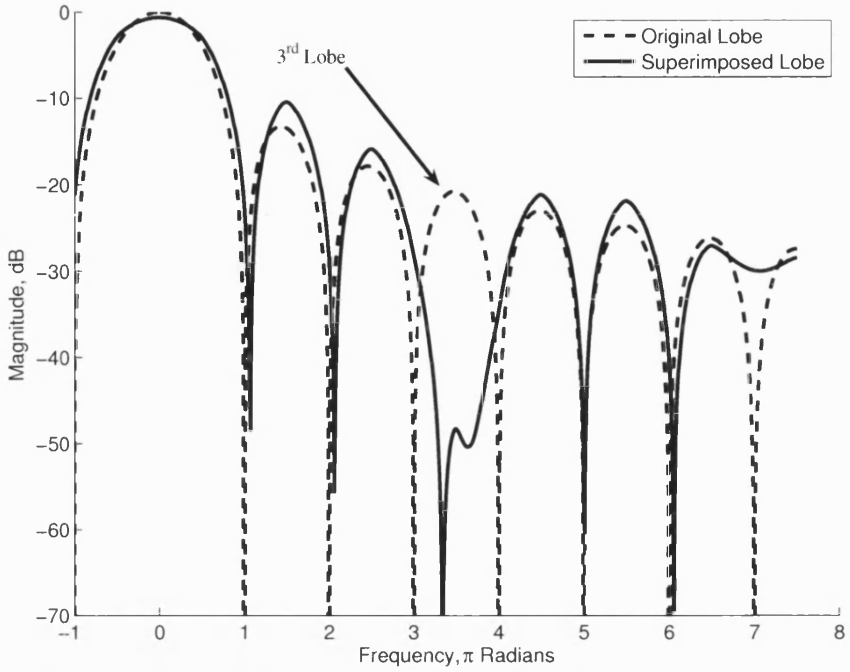

Figure 5.4 Targeting 3rd side lobe using analytical approximation to superimposition technique

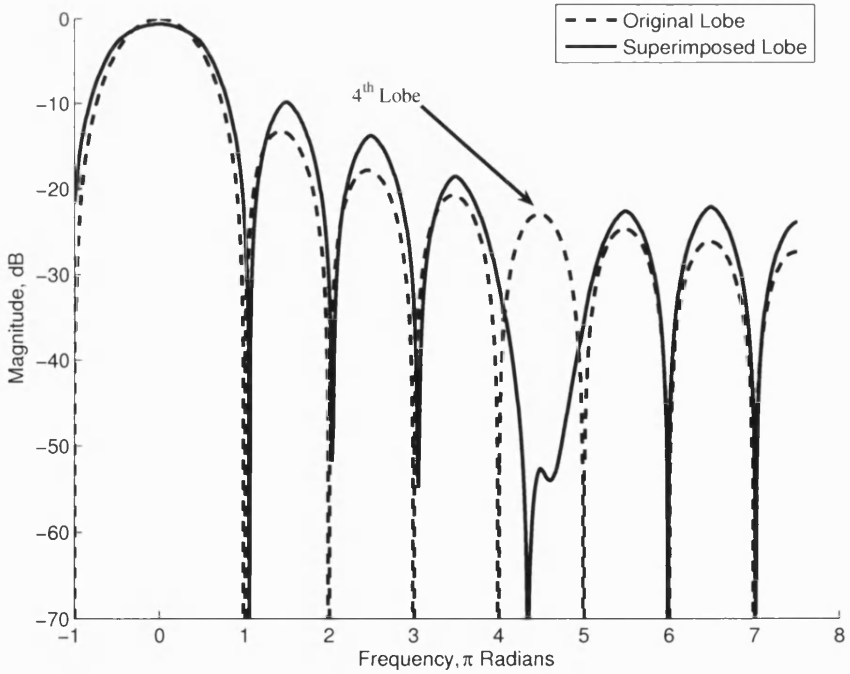

Figure 5.5 Targeting 4th side lobe using analytical approximation to superimposition technique

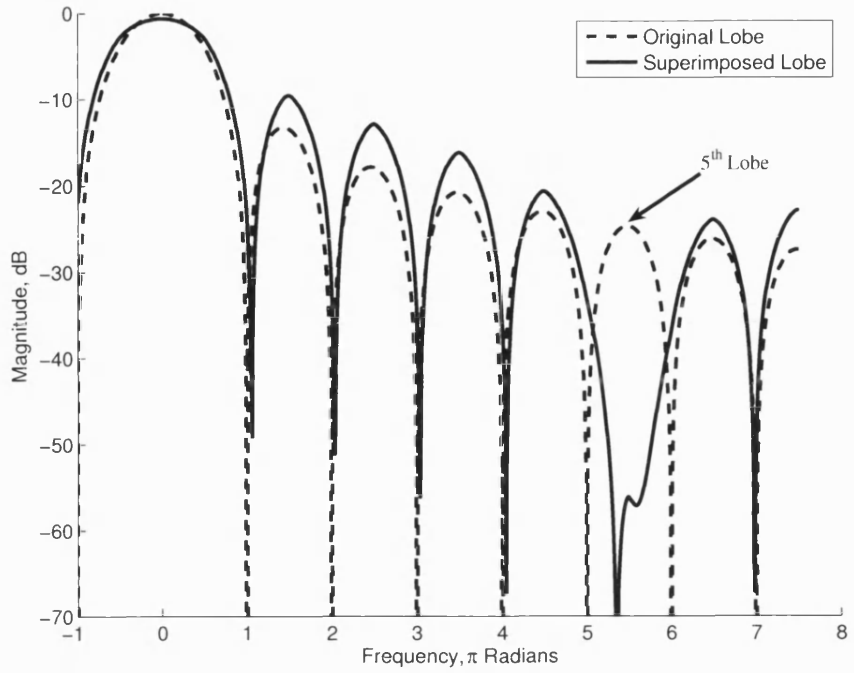

Figure 5.6 Targeting 5th side lobe using analytical approximation to superimposition technique

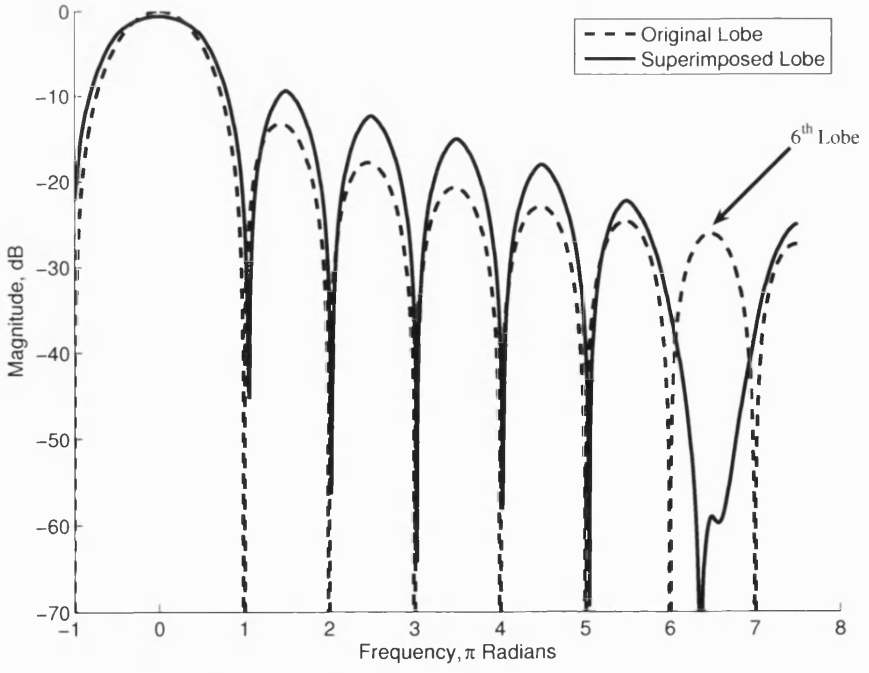

Figure 5.7 Targeting 6th side lobe using analytical approximation to superimposition technique

Next, using a simulated sine wave with frequency 5.1 kHz and duration 5.8 milliseconds, the improvement in side lobe levels achieved by applying the superimposition technique was investigated. Each side lobe is targeted in turn using truncation only (see section 4.3.2) as shown in Figure 5.8 to Figure 5.13 where the superimposition technique is applied to target the 1st to 6th side lobes respectively. Table 5.2 lists the side lobe levels after the superimposition technique is applied. In all cases the side lobe level after the superimposition technique has been applied averages around the 30 dB mark with an improvement of as much as 21 dB's in the case of the 2nd side lobe. However, the improvements in side lobe suppression reduces as we target higher side lobes with the 6th side lobe showing an improvement of just 6.8 dB's

Side lobe	DFT side lobe level /dB	Superimposition side lobe level / dB	Improvement /dB
1st	-13.5	-32	18.5
2nd	-17.9	-39	21.1
3rd	-20.8	-37	16.2
4th	-23.0	-36	13
5th	-24.8	-35	10.2
6th	26.2	-33	6.8

Table 5.2 Superimposition technique side lobe levels based on simulated sine wave

The measured results based on the simulated sine wave are significantly different from the analytical levels previously predicated. This should be expected, as in the analytical approximation, no DFT's and normalisations were performed. Rather, the technique started with perfect sinc functions and the averaging was performed through direct implementation. However, both approaches highlight the potential of the technique in suppressing side lobes and at the same time highlight a limitation.

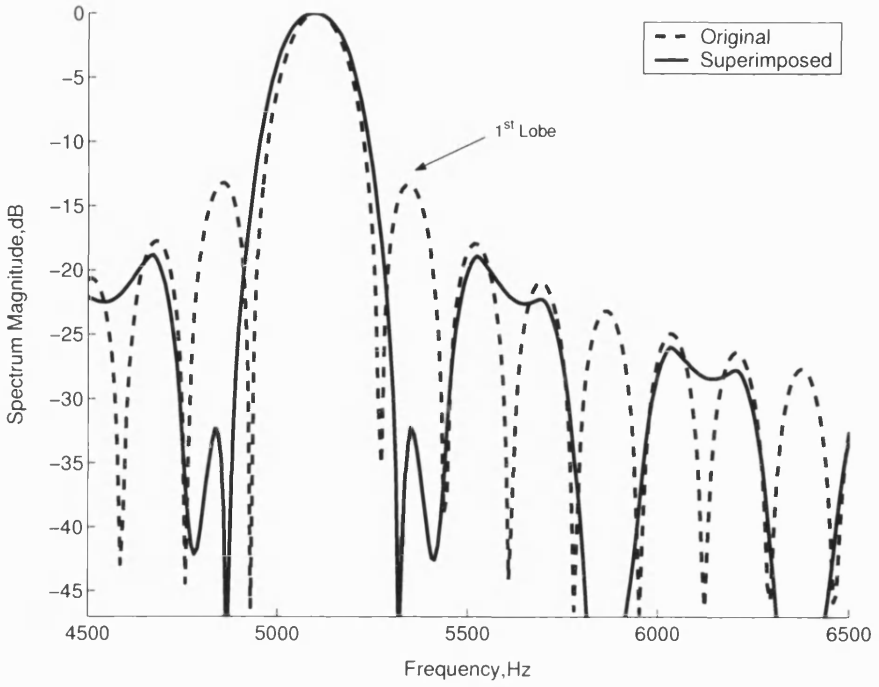

Figure 5.8 Targeting 1st side lobe using a simulated sine wave

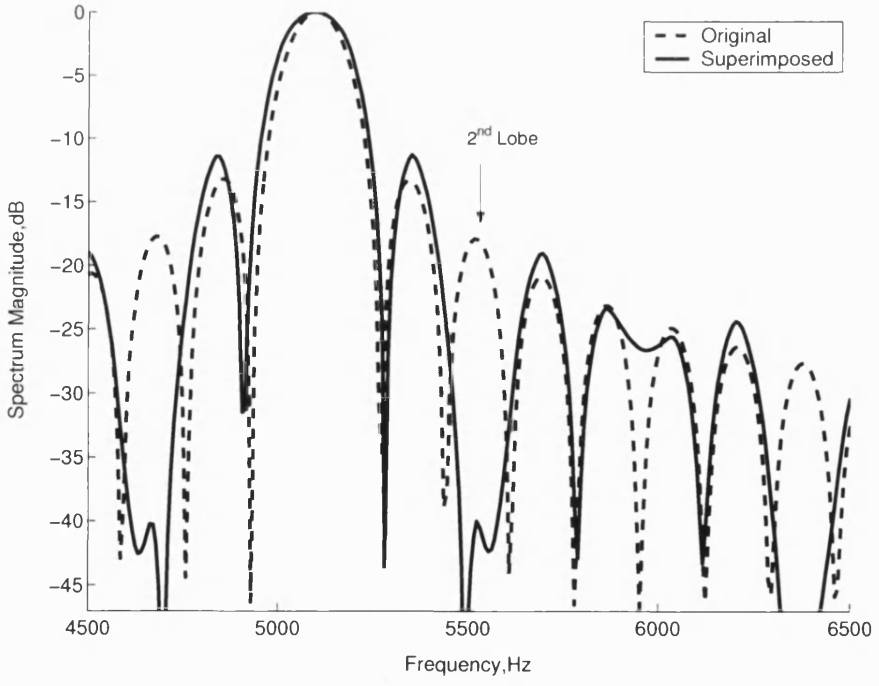

Figure 5.9 Targeting 2nd side lobe using a simulated sine wave

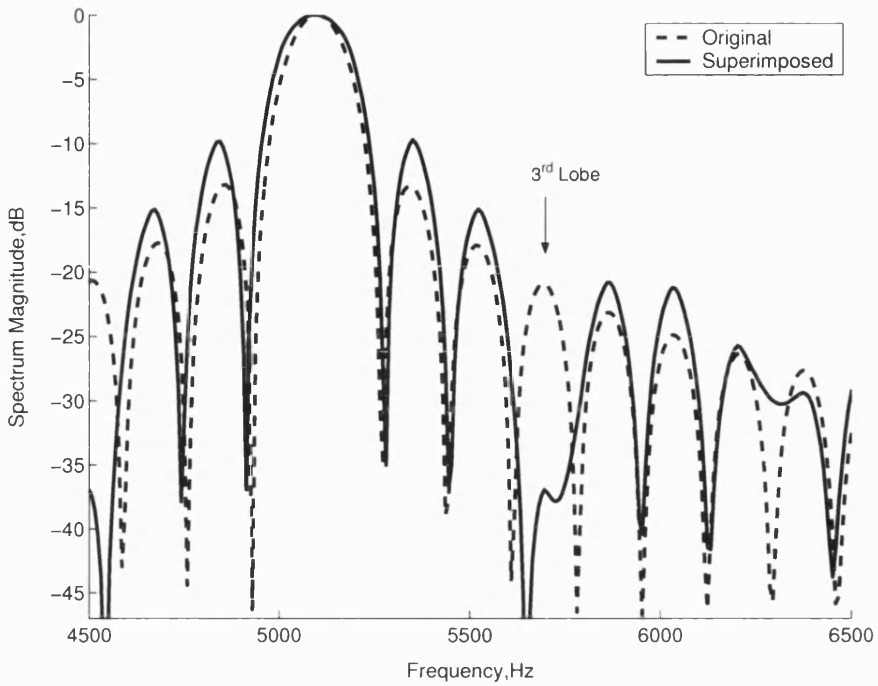

Figure 5.10 Targeting 3rd side lobe using a simulated sine wave

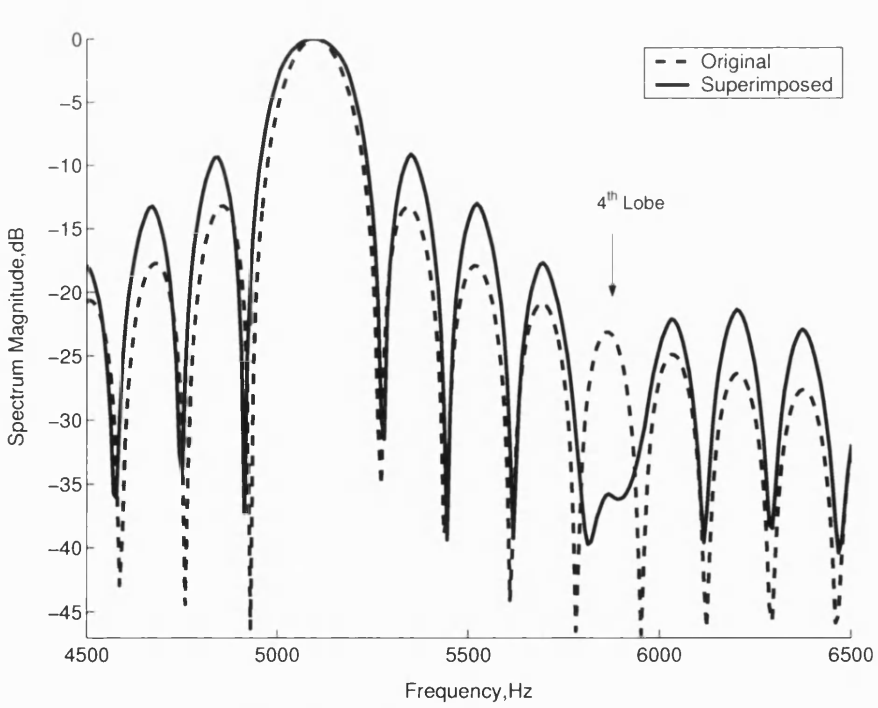

Figure 5.11 Targeting 4th side lobe using a simulated sine wave

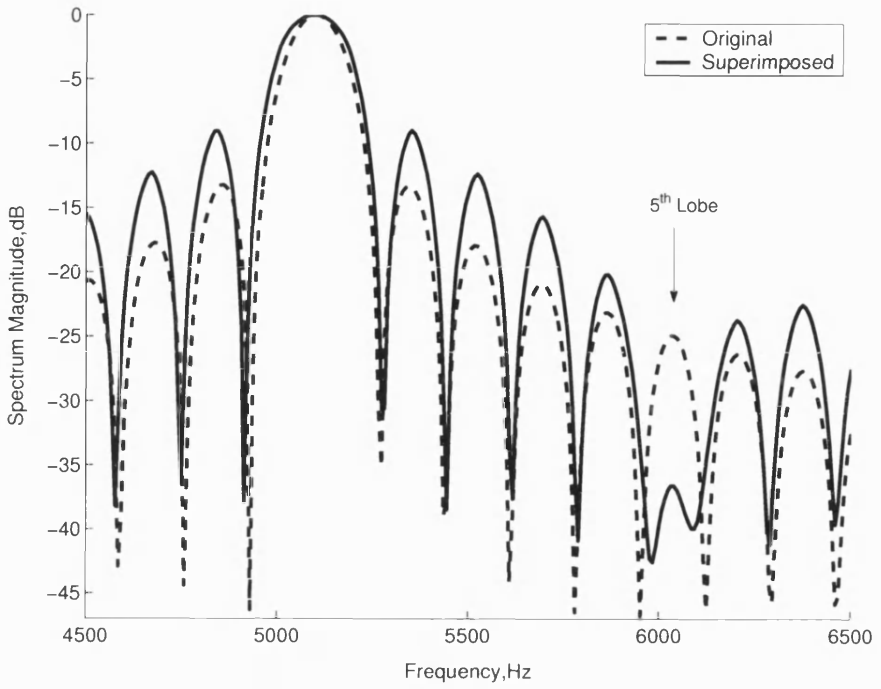

Figure 5.12 Targeting 5th side lobe using a simulated sine wave

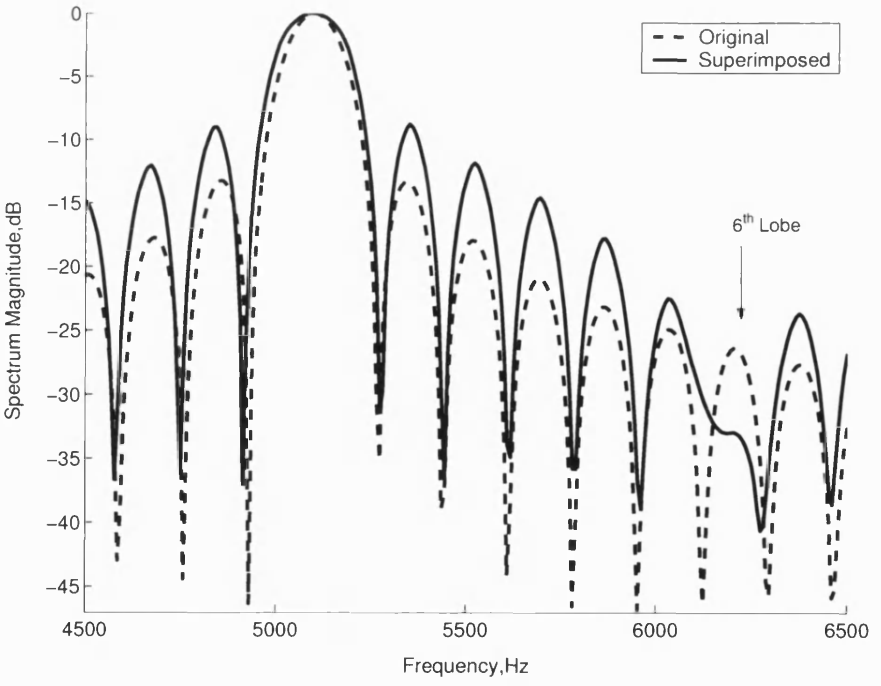

Figure 5.13 Targeting 6th side lobe using a simulated sine wave

5.2.2 Technique Variations

In section 4.5.1 various combinations on how the technique could be applied were introduced, in this section we compare some of the variations on a simulated sine wave with frequency 5.1 kHz and duration 5.8 milliseconds.

In Figure 5.14 and Figure 5.15 the 2nd and 3rd side lobes are targeted respectively by truncation in conjunction with windowing. Comparing this variation in Figure 5.14 and Figure 5.15 to Figure 5.9 and Figure 5.10 where just truncation is used we can see that in both cases similar levels of side lobe suppressions are achieved while maintaining their resolutions. However, in Figure 5.14 and Figure 5.15 the subsequent side lobes appear to be suppressed due to the windowing functions used in the superimposition technique.

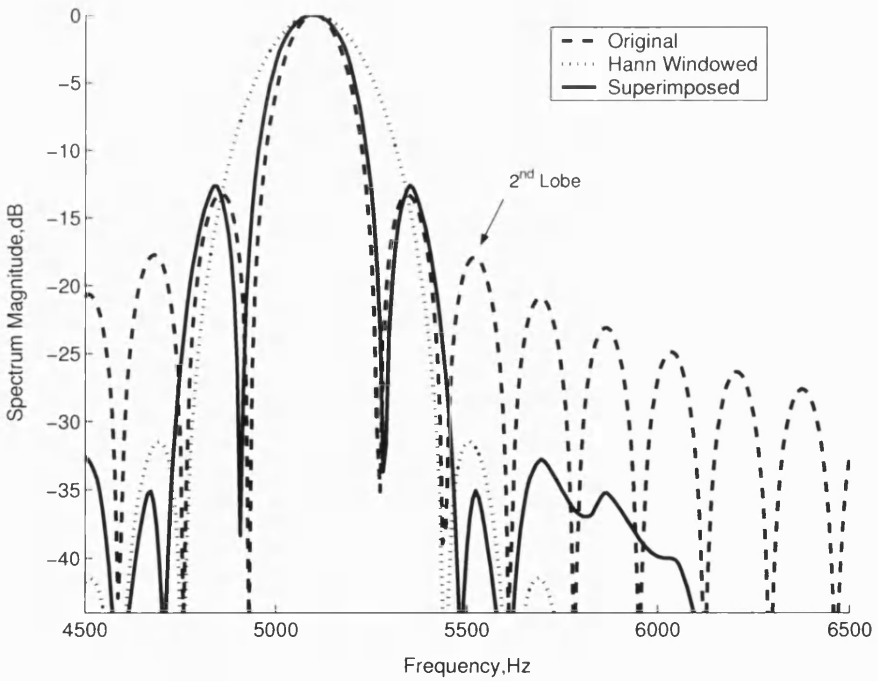

Figure 5.14 Targeting 2nd side lobe with truncation and Hann windowing

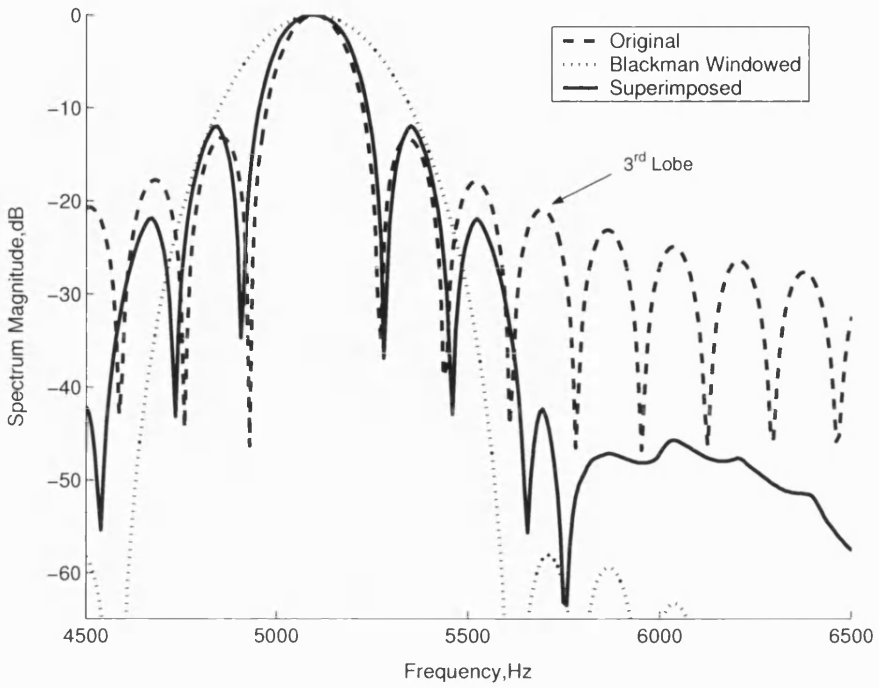

Figure 5.15 Targeting 3rd side lobe with truncation and Blackman windowing

Targeting of successive side lobes was also investigated. Figure 5.16 shows the superimposition technique spectrum where the first three side lobes are targeted using truncation only and in Figure 5.17 the superimposition spectrum where the first four side lobes are targeted is shown. Looking at Figure 5.16 and Figure 5.17 there appears not to be much difference in terms of the side lobe suppression and resolution, in particular there appears to be a peak in between the 2nd and 3rd side lobe common to both cases.

In Figure 5.18 the superimposition technique spectrum is shown where the technique has been set up to target the first three side lobes but in this case the 2nd side lobe is targeted using truncation in conjunction with the Hann window and the 3rd side lobe is targeted using the truncation in conjunction with the Blackman. In this case the peak that appears in Figure 5.16 where only truncation was used, has been suppressed and the subsequent side lobe levels appear to be much better with resolution being maintained.

Several other variations were tested and it was concluded that the technique variation whereby the first three side lobes are targeted using truncation only for the 1st side lobe,

truncation in conjunction with the Hamming window for the 2nd side lobe and truncation in conjunction with the Blackman window for the 3rd side lobe provides the best performance. The performance measure was based on the level of side lobe suppression for both the targeted side lobes and subsequent side lobes.

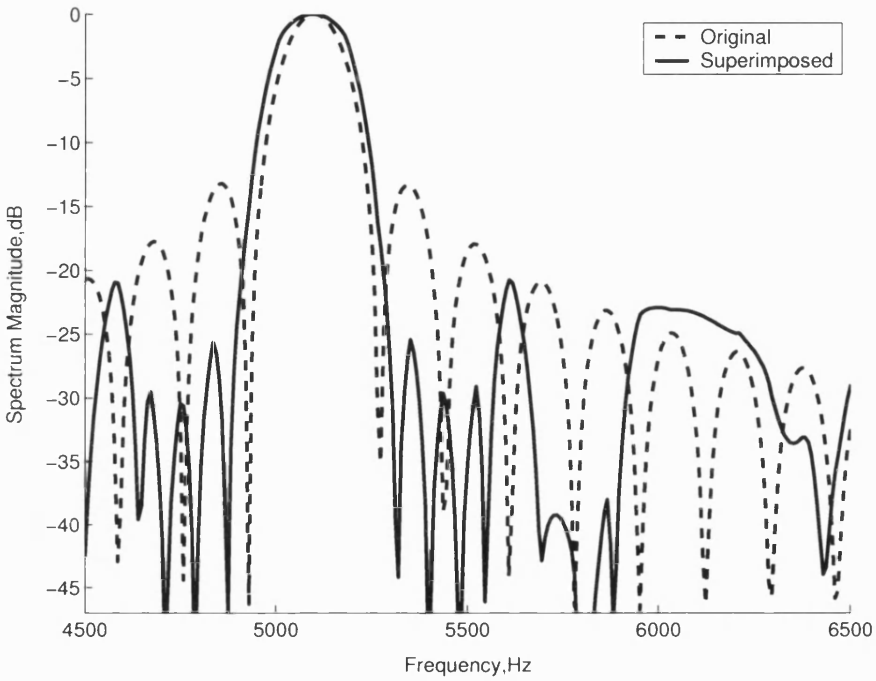

Figure 5.16 Targeting side lobes 1 to 3 using truncation only

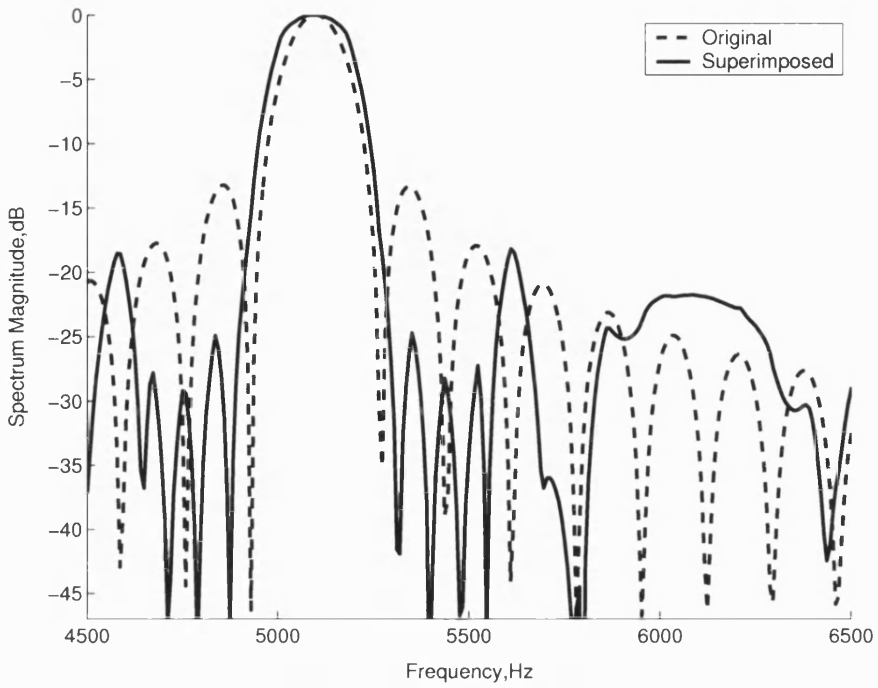

Figure 5.17 Targeting side lobes 1 to 4 using truncation only

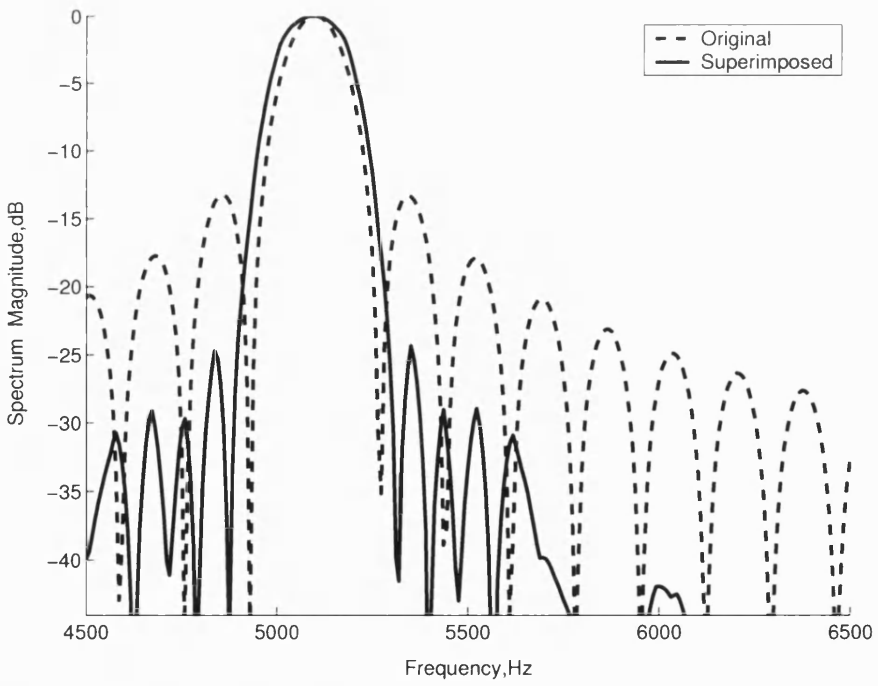

Figure 5.18 Targeting side lobes 1 to 3 using truncation in conjunction with the Hann and Blackman windows

5.2.3 Detection of Weak Components

In this section we look at the detection capability of the superimposition technique. In particular we look at the technique's ability to detect a weak frequency component which is located on the side lobe position of a stronger component and would otherwise have gone undetected by DFT analysis alone. The simulated data set consists of two sine waves of equal duration of 5.8 milliseconds with the stronger sine wave having a frequency of 5 kHz and the weaker sine wave having a frequency equal to the position of the side lobe of the stronger frequency it was placed on. Also the strength of the weaker sine wave is half the strength of the side lobe of the stronger frequency it is placed on. The frequency positions of the first three side lobes of a 5 kHz sine wave with duration 5.8 milliseconds are listed in Table 5.3. In all cases presented the technique has been set up to target the first three side lobes. The variation used (see section 4.5.1) targets the 1st side lobe using truncation only, the 2nd side lobe using truncation in conjunction with the Hamming window and the 3rd side lobe the truncation in conjunction with the Blackman window.

Side lobe	Frequency position /Hz
1st	5258
2nd	5430
3rd	5602

Table 5.3 Side lobe positions of a 5 kHz sine wave with duration 5.8 milliseconds

Figure 5.19 to Figure 5.20 show the spectrums of a signal composed of two frequency components with the weaker frequency component located on a side lobe of the stronger frequency and at half the strength of the side lobe it is located on. In Figure 5.19 where the weaker frequency is located on the 1st side lobe of the 5 kHz component, we can see that only the superimposition technique detects the weaker frequency even though the there is an error in true position of the weaker frequency.

In Figure 5.20 the weaker frequency is located on the 2nd side lobe of the 5 kHz component, again only the superimposition technique detects the weaker frequency but this time around with accuracy in position detection. Finally, when the weaker frequency is

located on the 3rd side lobe of the 5 kHz component as shown in Figure 5.21, again only the superimposition technique detects the weak frequency without compromising the true position of the weaker frequency.

In Figure 5.22 we consider the case of a weak frequency component on the 1st side lobe of a 5 kHz component and an additional much weaker component at 6.5 kHz. Clearly windowing enhances the deeper target response but is failing to resolve apart the 5 kHz component and the component located on its 1st side lobe. Even though the superimposition technique was set-up to optimise the performance around the first 3 side lobes, it still resolves all the 3 components of the simulated signal and does not broaden the response from the component at 6.5 kHz.

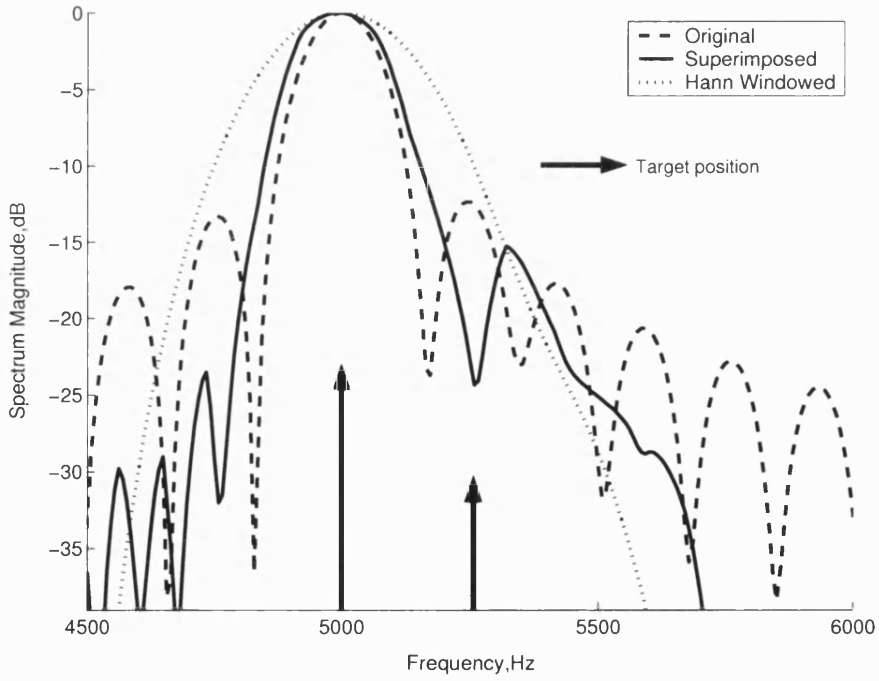

Figure 5.19 Detecting weak frequency component located on 1st side lobe position of stronger frequency component

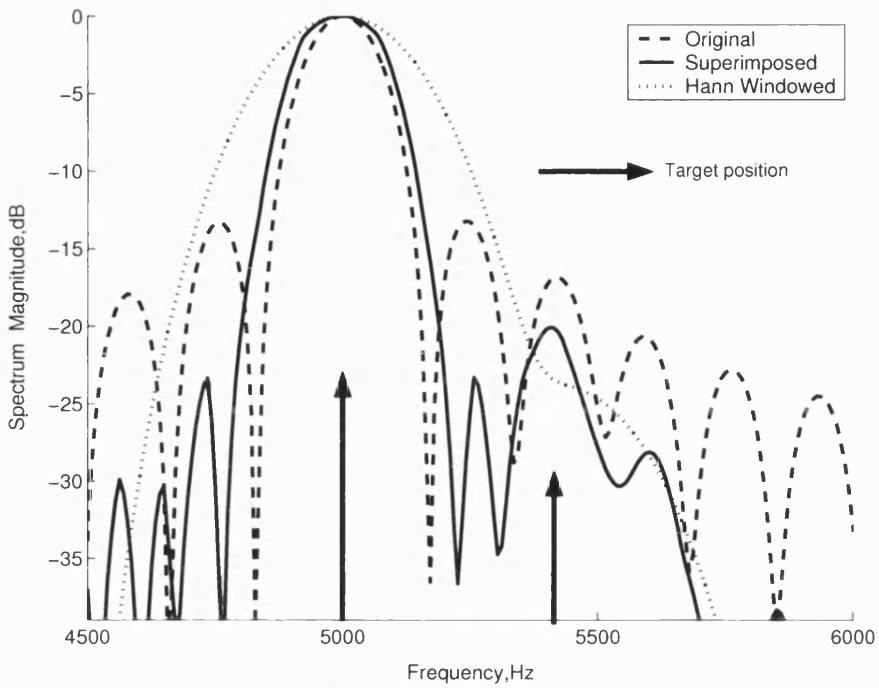

Figure 5.20 Detecting weak frequency component located on 2nd side lobe position of stronger frequency component

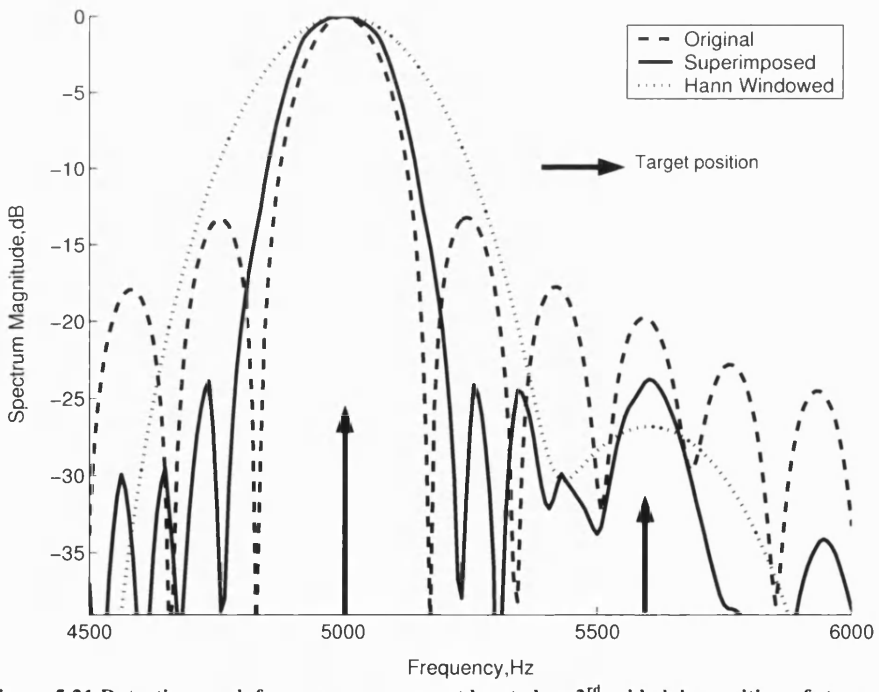

Figure 5.21 Detecting weak frequency component located on 3rd side lobe position of stronger frequency component

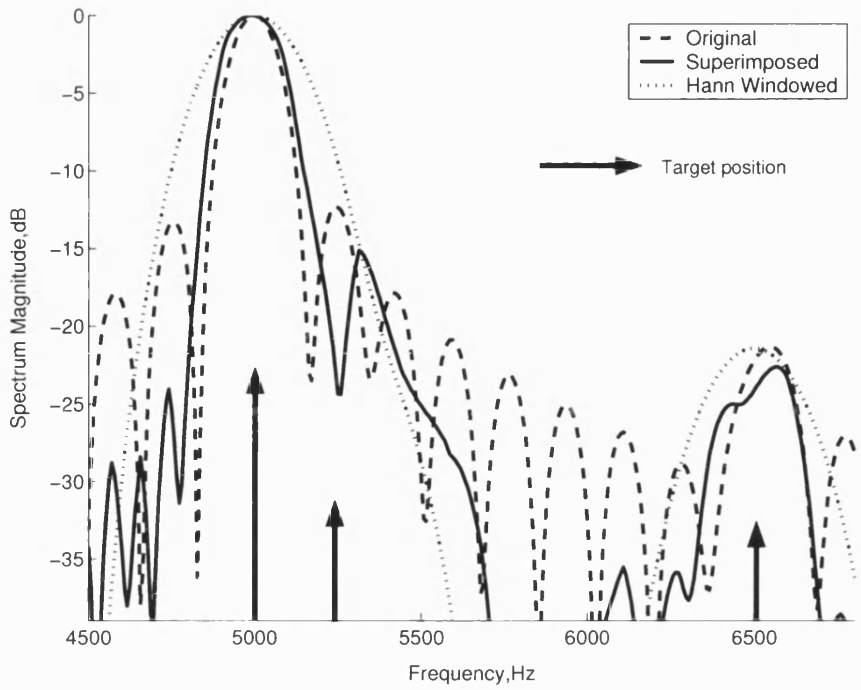

Figure 5.22 Detecting a higher weaker frequency in the presence of a much stronger lower frequency

5.3 GPR System Simulation

Already some performance aspects of the superimposition technique have been tested in section 5.2 using sine waves of varying strengths. In this section the superimposition technique is tested on data generated from simulations of FMCW GPR systems. The simulation of a GPR system was required right from the onset of the project to help in understanding FMCW GPR behaviour as well as to test various aspects of the superimposition technique as it was developed. In the next section the simulation model is discussed.

5.3.1 Simulation Model

Figure 5.23 shows a diagram of the simulation model. The simulation has three sets of inputs, namely:

1. FMCW parameter i.e. the parameter of the Radar system
2. Target Parameters – depth and physical characteristics of target
3. Propagation Medium parameters – this includes the soil permittivity, ε_r and conductivity, σ

The output of the simulation is a time series representing the beat signal after the received signal has been mixed and filtered (see section 3.2) based on the GPR radar equation presented in Chapter 2.

For the purposes of the simulation the GPR equation is simplified, constant factors in the GPR equation will be ignored as the signal analysis problem is that of relative response strengths between targets rather than their absolute values. The simplified form of the GPR equation for the simulation then becomes:

$$P_r = \frac{1}{r^4}\alpha_r' \tag{5.4}$$

where α_r' is the material attenuation loss due to the medium attenuation constant α and r is the range to the target.

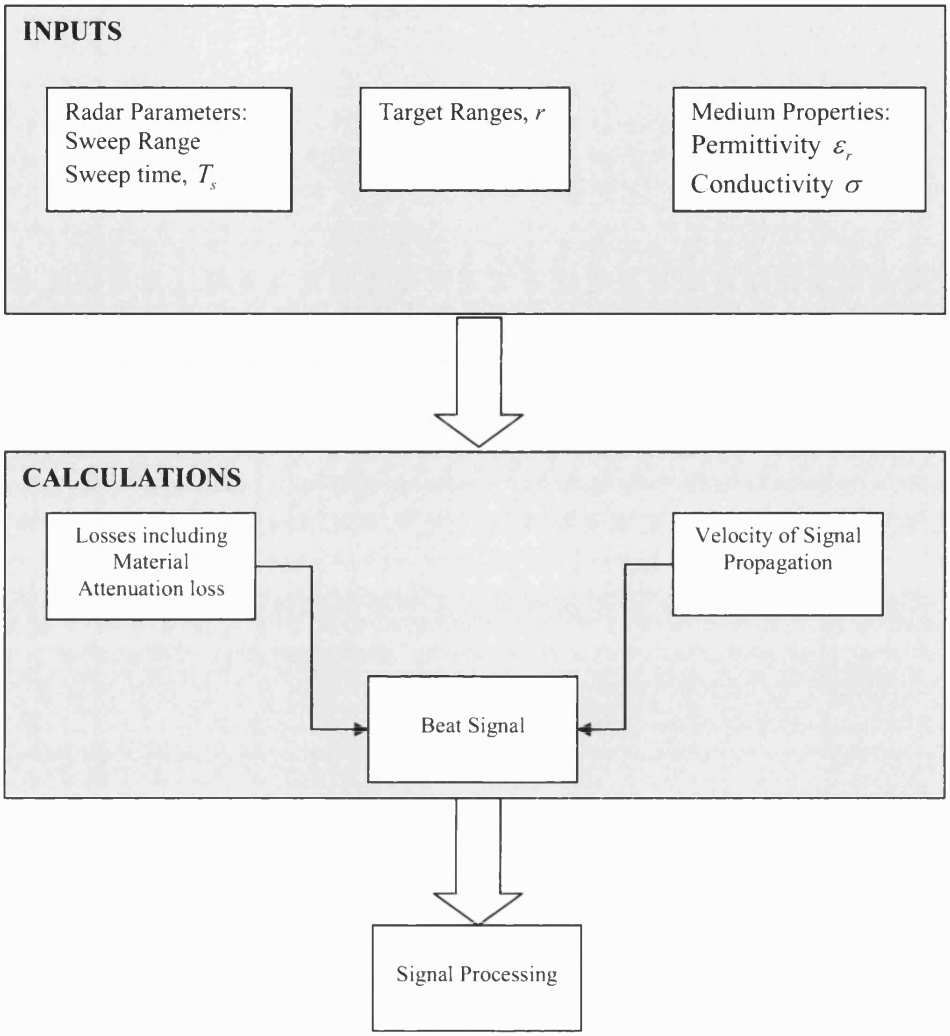

Figure 5.23 FMCW system simulation

In addition the following assumptions were made to simplify the simulation

- Dielectric mediums are considered to be uniform and homogeneous; hence permittivity ε_r and conductivity σ are constant within a given medium
- Relative magnetic permeability $\mu_r = 1$ at all frequencies
- Over the frequencies of interest the relative electrical permittivity ε_r is considered constant
- Material attenuation constant, α, is directly proportional to frequency

The last two assumptions are due to the fact that modelling the electrical properties of dielectrics is difficult (see section 2.3). However, it has been shown that over the typical frequency range of operation for FMCW GPR systems the permittivity of a given material sample is fairly constant [9]. The last assumption is based on results in [40] where material attenuation α loss was found to be directly proportional to frequency and also from (2.20); when frequency, $f = 0$ i.e. at DC, the attenuation constant, $\alpha = 0$. Therefore a single value of the attenuation constant at a given frequency could be used to estimate attenuation constants at other frequencies as:

$$\alpha(f) = \frac{\alpha_{f_m}}{f_m} f \tag{5.5}$$

To simulate the beat signal in the time domain, we will need to transform (5.5) into a function of time. Recall from Chapter 3, the frequency of the transmitted signal is given as a function of time in (3.1). Substituting for the frequency in (5.5) using (3.1) gives the material attenuation constant as a function of time:

$$\alpha(t) = \frac{\alpha_{f_m}}{f_m}\left(f_l + \frac{\Delta f}{T_s} t\right) \tag{5.6}$$

where f_l is the lower bound of the frequency sweep range.

Where the corresponding material attenuation loss for a target at range r is then given as:

$$\alpha'(t) = e^{-\alpha(t)2r} \tag{5.7}$$

The beat frequency f_b of the targets and the propagation velocity of the signal in the medium are calculated as (5.8) and (5.9) respectively.

$$f_b = \frac{2r\Delta f}{vT_s} \tag{5.8}$$

$$v = \frac{c}{\sqrt{\varepsilon_r}} \tag{5.9}$$

Where

T_s is sweep time,

Δf is sweep width,

v is velocity of propagation,

ε_r is relative permittivity,

r is range to target,

c is speed of signal in vacuum.

Ignoring the constant phase terms of the beat signal (3.8), the beat signal can be re-written as:

$$S_b(t) = \frac{1}{r^4}\alpha_r'(t)\cos(2\pi f_b t) \tag{5.10}$$

5.3.2 Simulation Results

In this section we present some of the results of the simulation and apply the superimposition technique to some results. Two GPR radar systems *GPR A* and *GPR B* are modelled with their parameters listed in Table 5.5. *GPR B* has a much larger bandwidth than *GPR A* giving it the potential for much better resolution of targets. Also two soil types are modelled namely Dry Loamy Soil and Wet Loamy Soil with their electrical parameters listed in Table 5.4 which are typical of these soil types at 100MHz (see Table 2.1). The wet loamy soil is modelled as a high attenuation medium whereas the dry loamy soil is modelled as a medium with moderate attenuation.

First the problem of high frequency dependent attenuation is demonstrated. Figure 5.24 shows the DFT beat spectrum of two targets at 0.2 and 0.5m in wet loamy soil generated using *GPR B*. The target at 0.5m is heavily attenuated and is barely detectable. In Figure 5.25 where the same targets are located in the same wet loamy soil but with *GPR A* used to generate the beat signal, the target at 0.5m experiences a much heavier attenuation and is not detected at all due to the higher frequencies of *GPR A*.

Parameter	Dry Loamy Soil	Wet Loamy Soil
Relative Permittivity	6	10
Conductivity	10^{-3}	10^{-2}

Table 5.4 Model parameters for soils used in simulation

Parameter	*GPR A*	*GPR B*
Frequency Sweep	1.2GHz – 2.4GHz	250MHz – 750MHz
Bandwidth	1.2GHz	500MHz
Sweep Time	0.001s	0.024s
Sampling Frequency	32kHz	32kHz

Table 5.5 Model parameters for FMCW GPR systems simulated

Next, achieving better resolution through the use of the larger bandwidth signal is demonstrated. Figure 5.26 and Figure 5.27 show the DFT beat spectrums of three targets at 0.2m, 0.5m and 0.6m in dry loamy soil. In Figure 5.26 where *GPR B* is used the targets at 0.5m and 0.6m are barley resolved whereas in Figure 5.27, where *GPR A* is used, all three targets are detected with good resolution due to the larger bandwidth of *GPR B*.

Figure 5.28, Figure 5.29 and Figure 5.30 show the DFT beat spectrums from some simulation results as well as the windowed versions of the spectrums and superimposition technique versions. The superimposition technique has been set up to target the first three side lobes. The variation used (see section 4.5.1) targets the 1st side lobe using truncation only, the 2nd side lobe using truncation in conjunction with the Hamming window and the 3rd side lobe the truncation in conjunction with the Blackman window.

Figure 5.28 shows the beat spectrum of two closely located targets in wet loamy soil generated using *GPR* A. The DFT spectrum fails to resolve apart the two targets whereas the windowing and the superimposition technique resolve the two targets with the superimposition technique providing the better resolution.

In Figure 5.29 the beat spectrum of two well separated targets in wet loamy soil generated using *GPR B* is shown. Here only the superimposition technique succeeds in detecting the two targets with both the DFT and windowed DFT failing to detect the deeper target.

In Figure 5.30 the beat spectrum of two closely located targets and a much deeper target in dry loamy soil generated using *GPR A* is shown. The deeper target is always detected but only windowing fails to resolve apart the two closely located targets. Also the superimposition technique shows considerable improvement in side lobe levels especially with the deeper target.

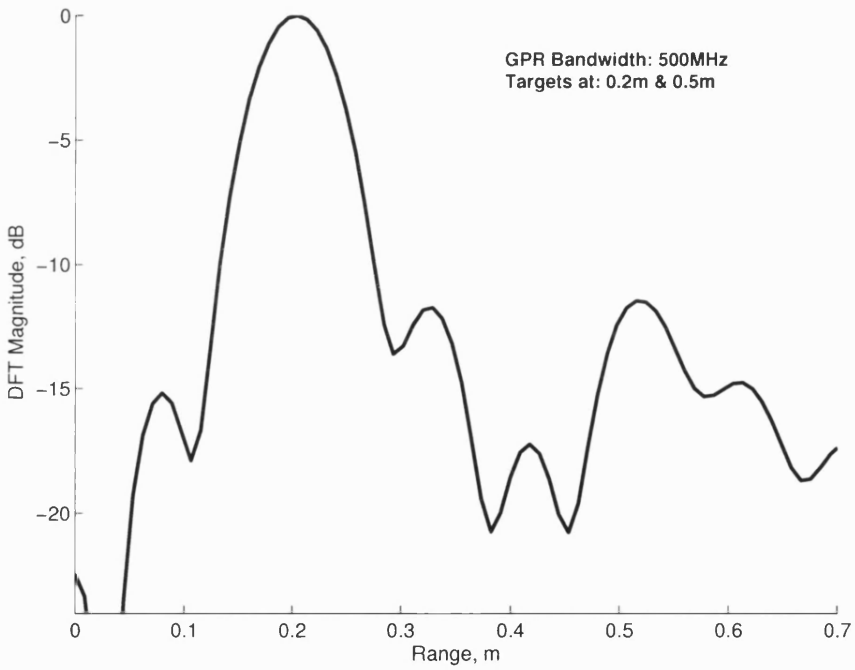

Figure 5.24 Detection of targets in wet loamy soil using a 500 MHz bandwidth FMCW GPR

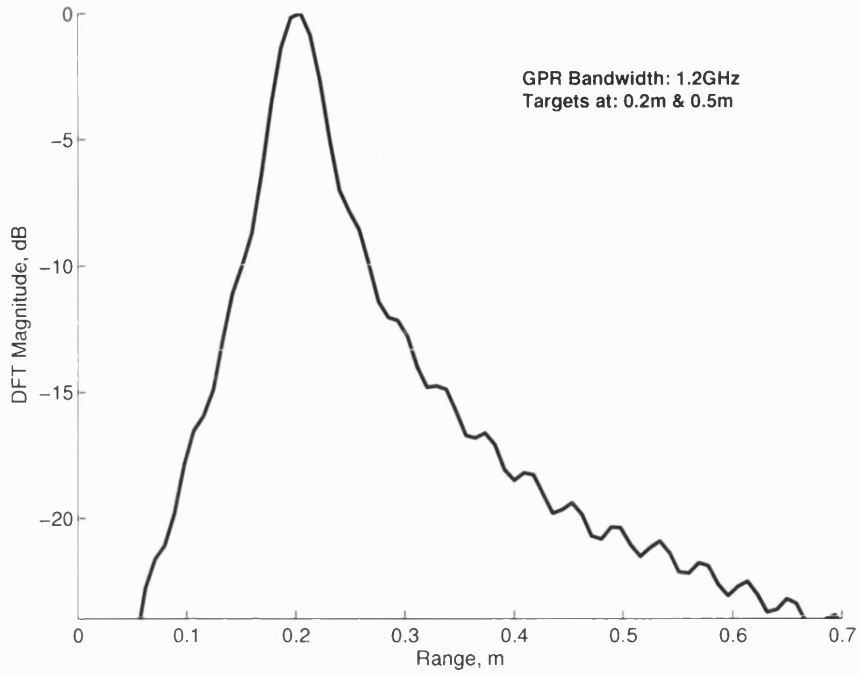

Figure 5.25 Detection of targets in wet loamy soil using a 1.2 GHz bandwidth FMCW GPR

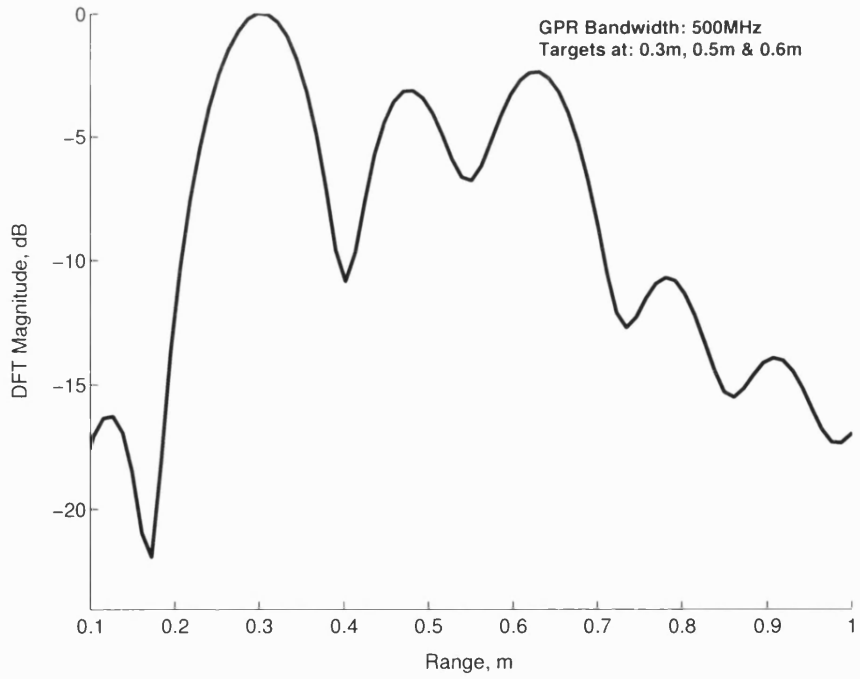

Figure 5.26 Resolving targets in dry loamy soil using a 500 MHz bandwidth FMCW GPR

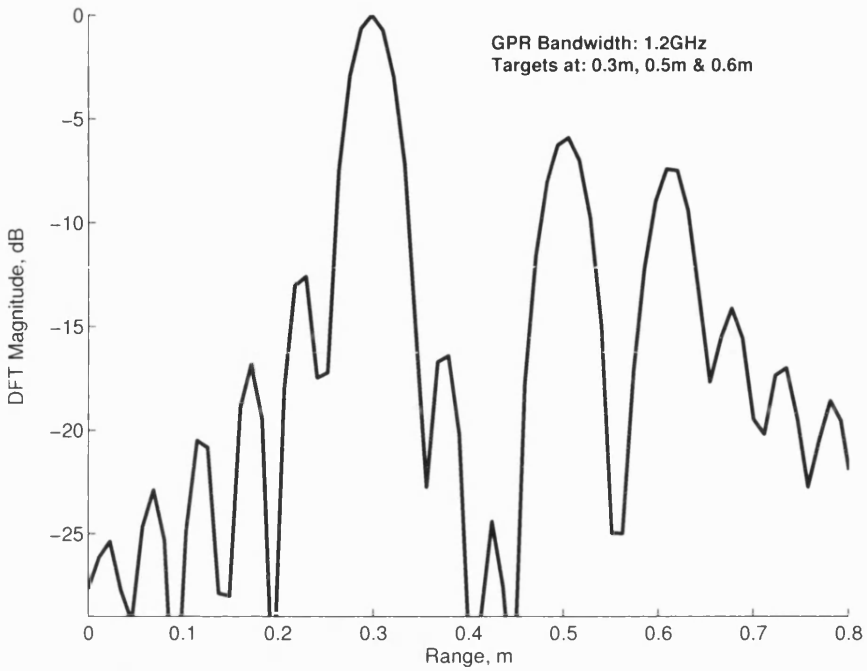

Figure 5.27 Resolving targets in dry loamy soil using a 1.2 GHz bandwidth FMCW GPR

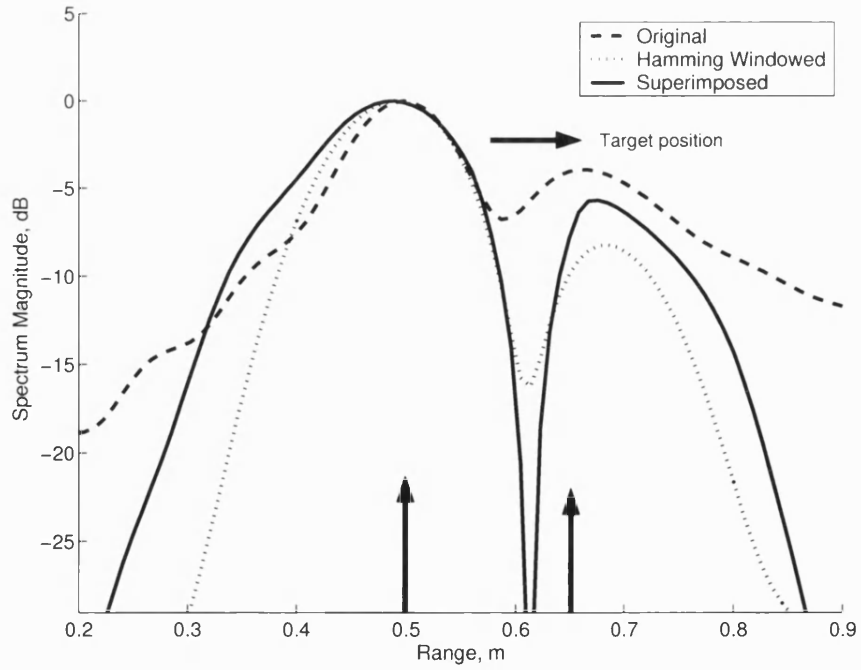

Figure 5.28 Beat spectrum from 500 MHz bandwidth GPR of closely located targets in wet loamy soil

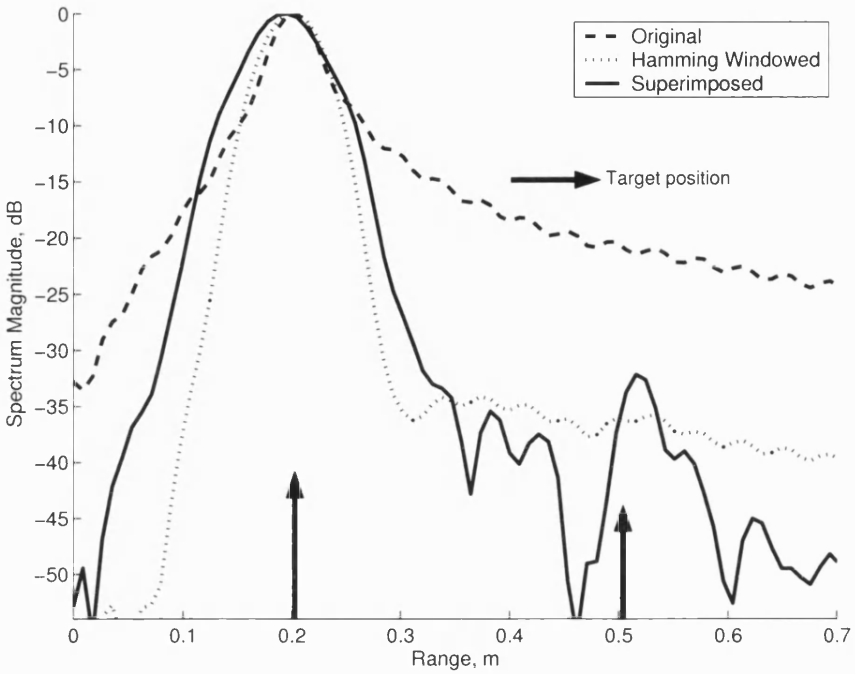

Figure 5.29 Beat spectrum from 1.2 GHz bandwidth GPR of well separated targets in wet loamy soil

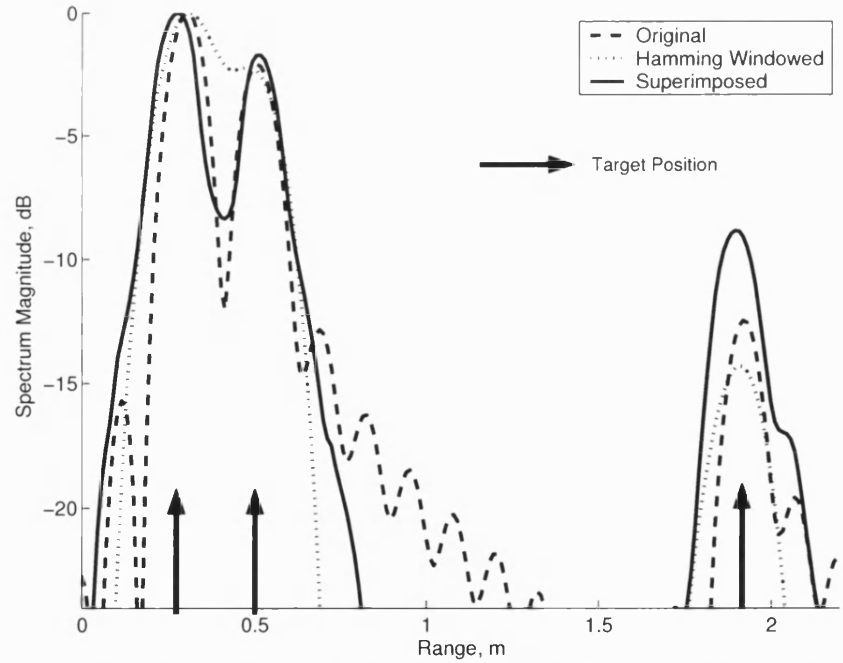

Figure 5.30 Beat spectrum from 500 MHz bandwidth GPR of 2 closely located targets and a deeper target in dry loamy soil

5.4 Experimental Results from Network Analyser

An experimental GPR System based on a Vector Network Analyser (VNA) was set up as shown in Figure 5.31. The VNA generates a Stepped Frequency Continuous Waveform (SFCW) signal and acts as the radar receiver as well. The idea of a GPR system based on a VNA is not new. In [90] the advantages and disadvantages of using VNA based GPR system are discussed and in [56] a VNA based GPR was used to collect experimental data. The VNA gives the advantage of being able to generate a wide and adjustable frequency bandwidth, which is particularly useful to GPR systems as such a system can be easily adjusted to suit various situations and also this relaxes the restrictions on antennas that can be used. However, the cost of VNA's does not make such systems feasible for commercial use. In the next section a description of the experimental model is presented.

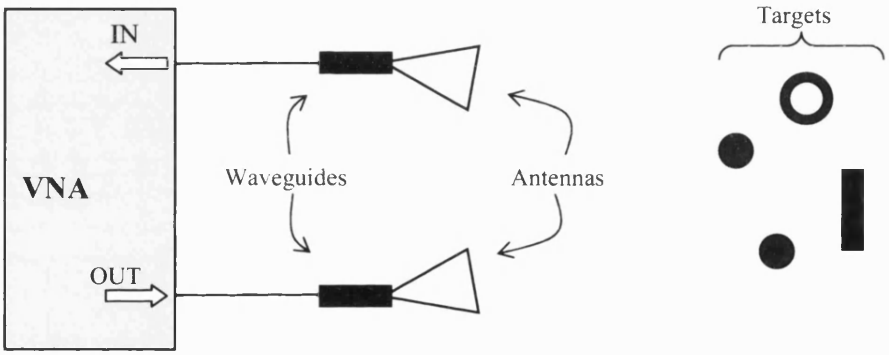

Figure 5.31 Experimental vector network analyser based GPR system

5.4.1 Experiment Model

The system in Figure 5.31 forms a network consisting of the VNA, connector cables, waveguides, horn antennas on both input and output ports of the analyser and the targets in free space. The antenna on the output port transmits a weighted chirp signal and the bistatic reflection off the targets is measured by the antenna on the input port. The impulse response is then calculated from the forward frequency response (phase and amplitude) of the network to give the target positions.

Assuming the reflection coefficients of the targets are frequency independent, the forward frequency response is then given as:

$$H(\omega)=\sum_{i=1}^{N} s_i \exp\{-j\omega\tau_i\} \tag{5.11}$$

where s_i is the reflection coefficient off the i^{th} target and τ_i is the 2-way delay to the target.

The impulse response is then calculated by taking the inverse Fourier transform of the frequency response (5.11) as:

$$\begin{aligned} h(t) &= \frac{1}{2\pi}\int_{\omega=-\infty}^{\infty} H(\omega)\, e^{j\omega t}\, d\omega \\ &= \frac{1}{2\pi}\int_{\omega=-\infty}^{\infty}\left[\sum_{i=1}^{N} s_i \exp\{-j\omega\tau_i\}\right] e^{j\omega t}\, d\omega \\ &= \frac{1}{2\pi}\sum_{i=1}^{N} s_i \int_{\omega=-\infty}^{\infty} \exp\{j\omega(t-\tau_i)\}\, d\omega \\ &= \frac{1}{2\pi}\sum_{i=1}^{N} s_i \delta(t-\tau_i) \end{aligned} \tag{5.12}$$

Equation (5.12) is a sum of Dirac delta pulses at time positions which correspond to the 2-way delays to the targets, τ_i. Due to the finite frequency sweep, the windowing effect and spectral leakage occur but this time in the time domain; hence the impulse response is actually a sum of sinc functions. This means that though the superimposition technique was presented for use in improving DFT analysis, it can also be applied to Inverse DFT analysis where impulse responses are being calculated from a finite frequency response data set.

5.4.2 Experiment Setup

The VNA used was the Anritsu 37397C [91]. Table 5.6 gives details of the VNA configuration used. The VNA was calibrated to the frequency range 8GHz to 12.5GHz to

match the antenna frequency range. However, the measurement reference planes are the end of the cable connectors on the input and output ports of the VNA, therefore impulse responses calculated will include delay times due to the waveguides connected to the antennas.

Parameter	Value
Frequency Sweep	8GHz – 12.5GHz
Frequency Step	0.01125GHz
Number of Steps	401

Table 5.6 Vector network analyser configuration

Figure 5.32 shows some of the objects used as targets in the experiments which include a rectangular steel slab, metal pipe and plastic pipes. The rectangular steel slab provides a flat and larger surface area which gives a much stronger reflection than the other smaller cylindrical objects. The complete experiment setup is shown in Figure 5.33.

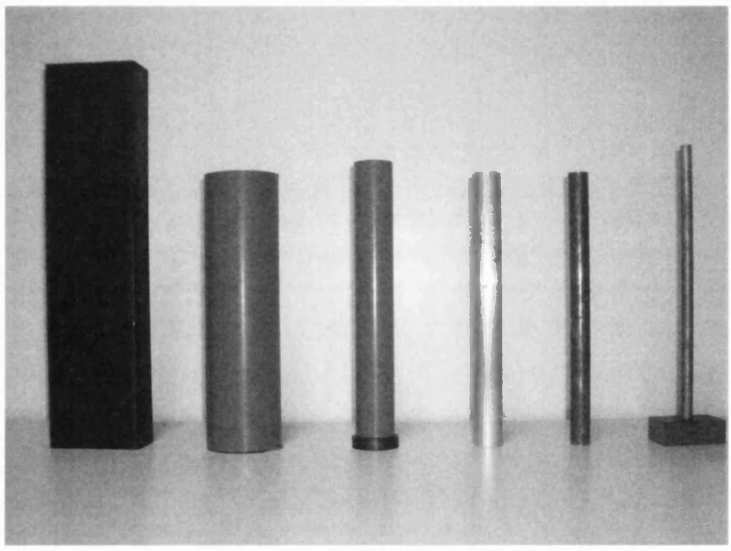

Figure 5.32 Steel slab, metallic pipes & rods and plastic pipes used as targets in experiment

Figure 5.33 Experiment setup

5.4.3 Experiment Results

Figure 5.34 to Figure 5.42 show a range of results obtained from various target setups. The targets have been set up to give scenarios where strong reflections are interacting with weaker reflections. For all the results presented the superimposition technique is set up to target the first three side lobes. The variation used (see section 4.5.1) targets the 1st side lobe using truncation only, the 2nd side lobe using truncation in conjunction with the Hamming window and the 3rd side lobe the truncation in conjunction with the Blackman window.

Figure 5.34 shows the impulse response from the measurement where a 10mm diameter cast iron rod is placed directly in front of a 40mm diameter air filled plastic. The impulse response should indicate the presence of 3 targets due to the reflection off the cast iron rod and two reflections from the front and back sides of the pipe. However, only the presence of the cast iron rod is clearly indicated with a single strong peak with the high lobes around the strong peak suggesting the presence of other targets. As shown in Figure 5.34 applying windowing degrades resolution and appears to have merged the smaller lobes into a single

target, whereas applying the superimposition technique clearly resolves the 3 targets as expected.

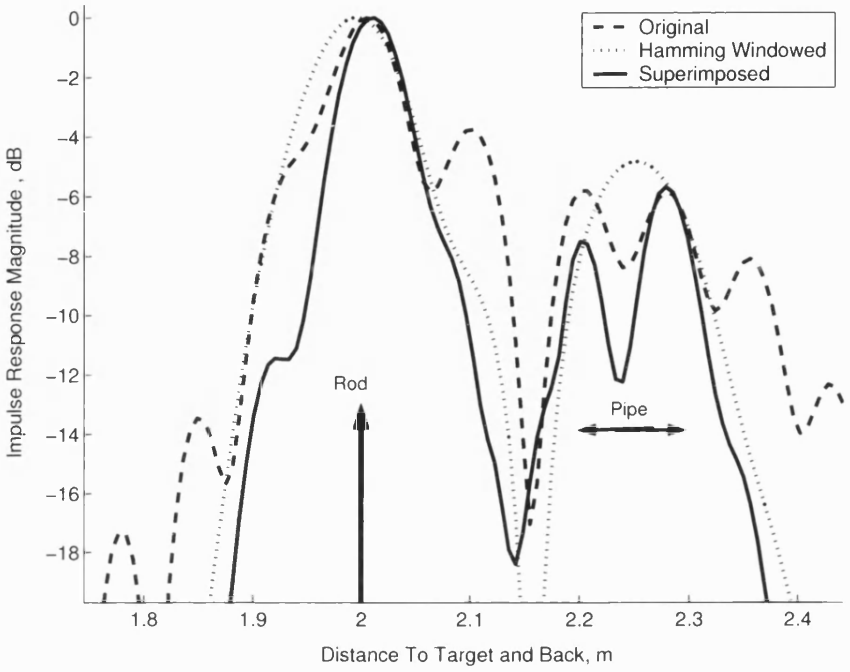

Figure 5.34 Impulse response of reflection off an iron rod placed in front of an air filled pipe

Figure 5.35 shows the impulse response from the measurement where a 10mm diameter cast iron rod is placed in front of a 100 mm wide steel slab. The impulse response suggests the presence of two targets. Applying the Hamming window improves the resolution but the superimposition technique gives a much better resolution.

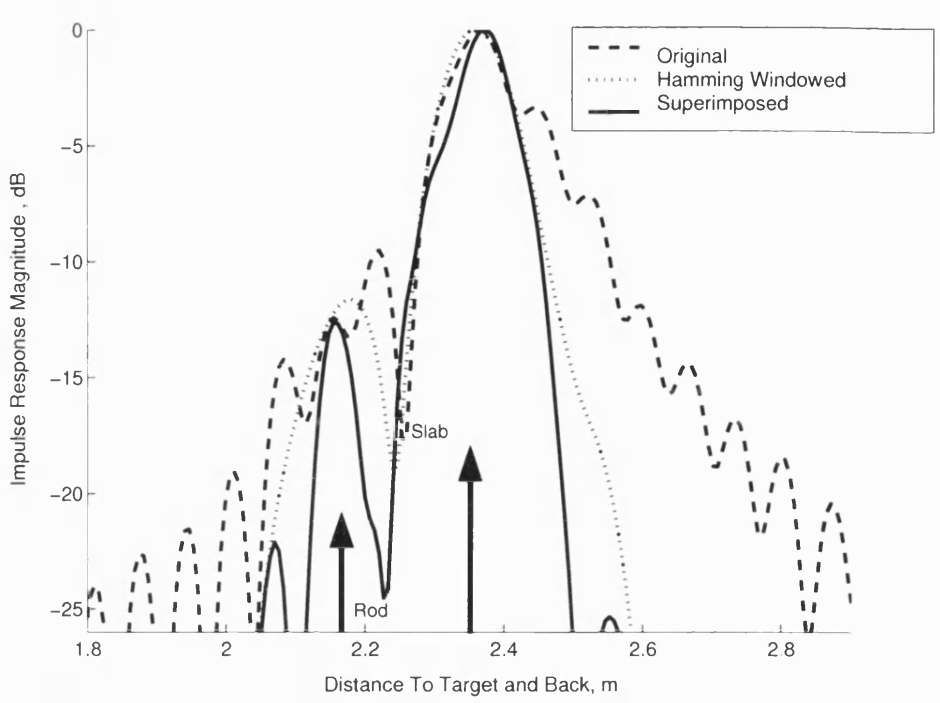

Figure 5.35 Impulse response of reflection off an iron rod placed in front of a steel slab

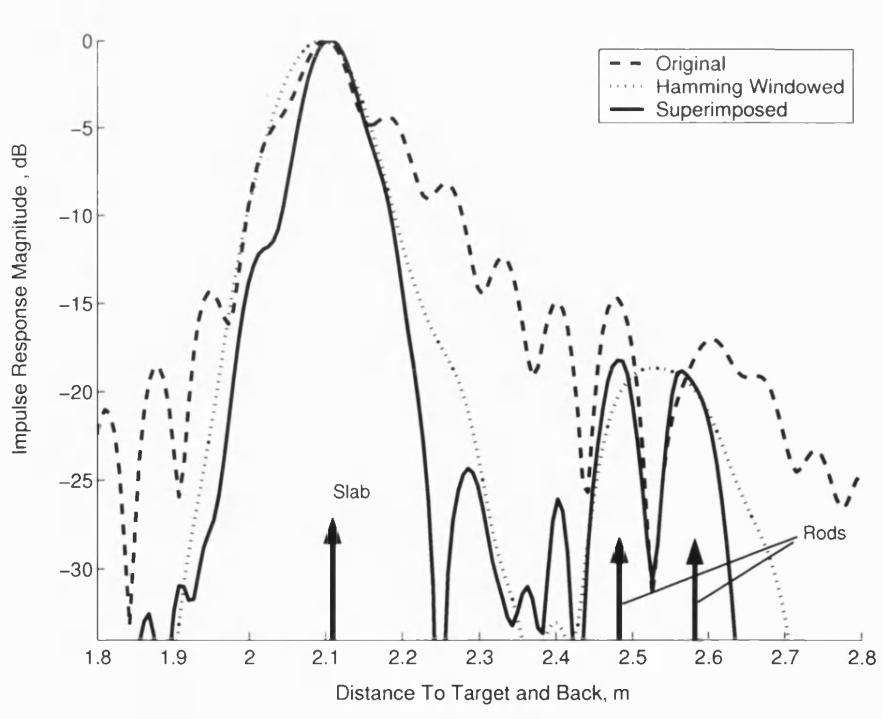

Figure 5.36 Impulse response of reflection off 2 closely spaced iron rods behind a steel slab

In Figure 5.36 the impulse response where two 10mm cast iron rods were placed close to each other and behind a 100 mm steel slab is shown. The Inverse DFT alone fails to clearly resolve the 2 iron rods in the presence of the strong reflection off the steel slab and applying the Hamming window function degrades resolution such that the two iron rods appear as a single target. On the other hand the superimposition technique clearly detects and resolves the two irons rods.

In Figure 5.37 the impulse responses of an empty 40mm plastic pipe is shown with the front and back sides of the pipe clearly visible. In Figure 5.38 the Inverse DFT impulse response of the same pipe filled with water is shown, it is now expected that the back side of the pipe will appear a further distance due to the signal slowing down in water and as a weaker response due to signal attenuation caused by the reflection losses at the air-water interfaces.

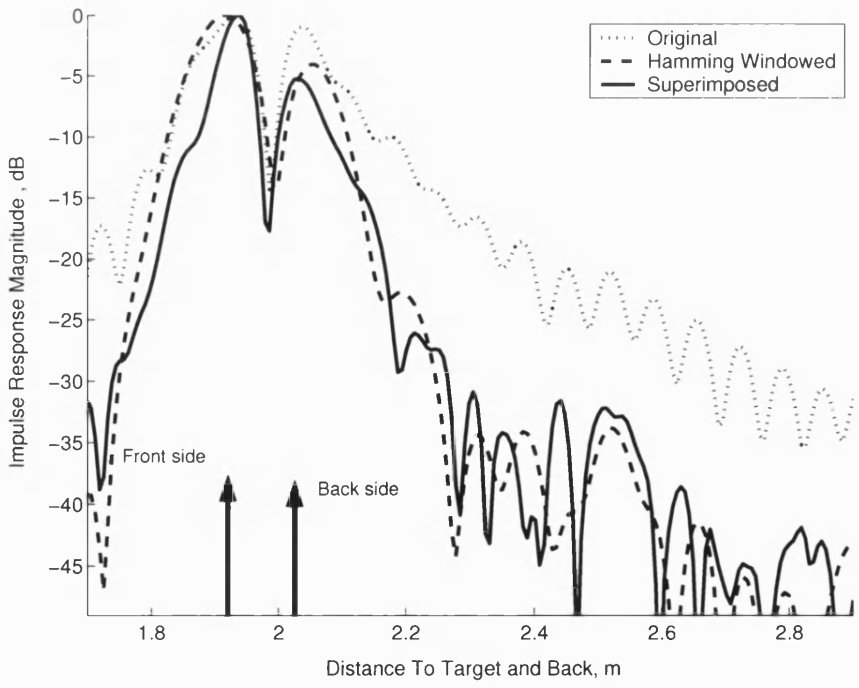

Figure 5.37 Impulse response of empty plastic pipe with 1st 3 side lobes targeted

In air, the front and back sides in the impulse response are expected to be separated by the signal propagation distances from the front side to the back side and from the back to the front side i.e. at least twice the diameter of the pipe (80mm). However, in water which has a relative permittivity, ε_r of 81, the signal is expected to slow down by a factor of 9 i.e. $\sqrt{\varepsilon_r}$, hence the front and back sides should be separated by at least 720mm.

In Figure 5.38 the inverse DFT impulse response of the water filled pipe indicates the front side response of the pipe at around 1.95m, therefore it is expected that the back side response will appear at around 2.67m. Close examination of the side lobes between 2.4m and 2.8m in the Inverse DFT trace of Figure 5.38 would suggest the presence of weaker targets. Figure 5.38 also shows the superimposition technique where the first three side lobes have been targeted failing to clearly resolve the back side of the pipe; instead multiple peaks appear possibly resulting from the scattering patterns of the signal on the curved pipe surface in water. It should also be noted that the side lobes of the stronger response of the front side that occur 720mm from its main lobe i.e. the 9th side lobe in particular, were not targeted.

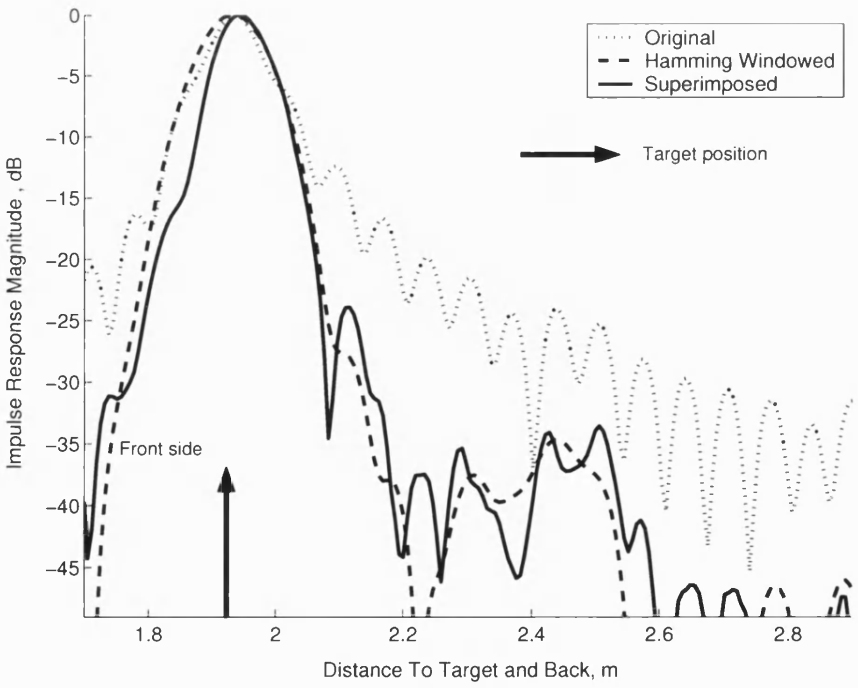

Figure 5.38 Impulse response of water filled plastic pipe with 1st 3 side lobes targeted

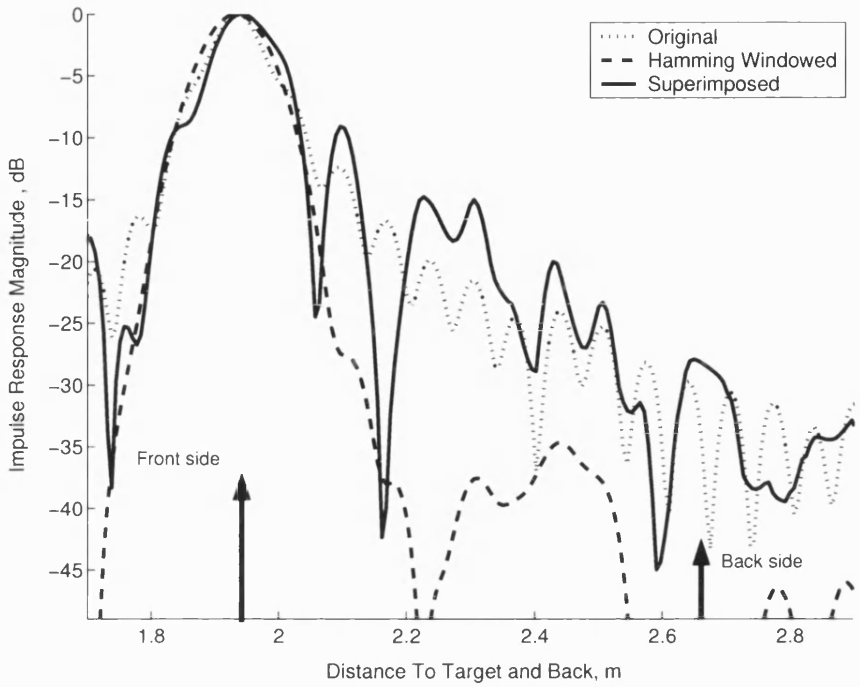

Figure 5.39 Impulse response of water filled plastic pipe with 1st, 9th, 10th and 11th side lobes targeted

In Figure 5.39 the superimposition technique has been setup to target the 1st side lobe using pure truncation and the 9th, 10th & 11th side lobes using truncation and the Hamming window, hence covering the area where we expect the back side response to be. In this case only the superimposition technique trace indicates the presence of a response at around 2.7m where we expected the back side response of the pipe to appear.

In a similar situation, the same 40mm diameter pipe was filled with methylated spirit (ethanol and methanol mixture) with a relative permittivity of around 20. In this case we would expect the separation of the sides of the pipe to be around 350 mm (i.e. the signal has been slowed down by a factor of $\sqrt{\varepsilon_r}$), which would be in the region between the 4th and 6th side lobes of the stronger response of the front side. As such in Figure 5.40 we have targeted the 1st side lobe using pure truncation and the 4th, 5th & 6th side lobes using truncation and the Hamming window, hence covering the area where we expect the back side response should be. Figure 5.40 shows the strong front side response at around 2.7m clearly resolved in all cases. However, the back side which we expected to be around

3.05m is resolved only in the superimposition and Hamming windowed traces, with the superimposition technique providing better resolution.

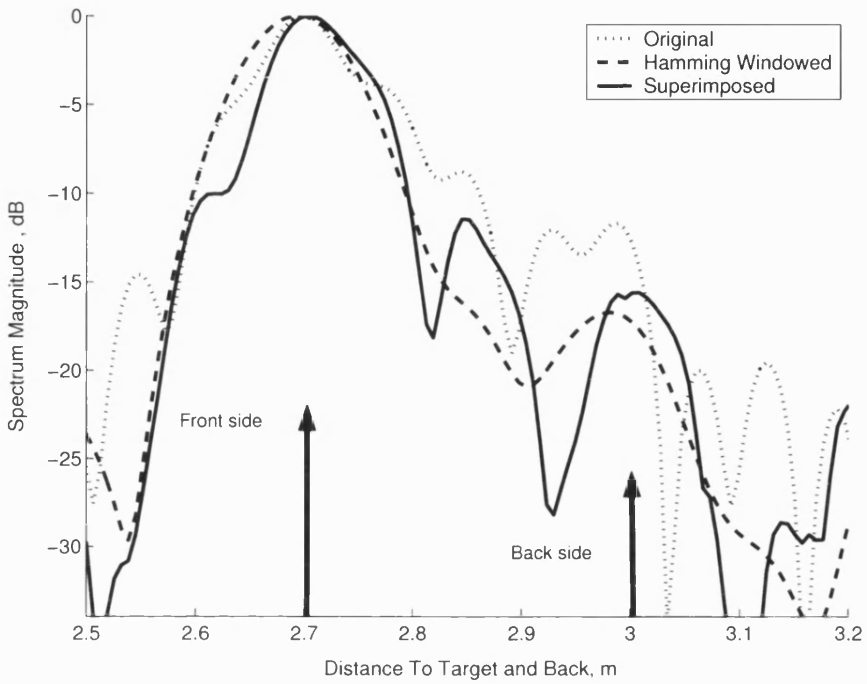

Figure 5.40 Impulse response of methylated spirit filled plastic pipe with the 1st, 4th, 5th and 6th side lobes targeted

The previous examples where we attempted to resolve the sides of a pipe filled with liquid have demonstrated a limitation of the technique. Though the technique is unsupervised, some knowledge of where the targets are could help in determining exactly which side lobes to target. Alternatively a brute force approach could be used whereby all possible side lobes could be targeted but this would be highly inefficient. It should also be noted that the frequency range of 8 GHz to 12.5 GHz used in the experiment is not typical of frequency modulated GPR systems, frequency modulated GPR systems tend to operate with a centre frequency of a giga-hertz or two and therefore in the previous examples the response from the back side would suffer from a relatively smaller attenuation hence improving the chances of detection.

Finally in Figure 5.41 and Figure 5.42 the problem of error in position detection due to lobes interacting is highlighted. In Figure 5.41 two 10mm diameter cast iron rods are separated such that the Hamming window is just resolving the 2nd target. However, the registration of the target position has been affected. The superimposition technique clearly shows a smaller deviation from the true target position than the case when the Hamming window is applied. In Figure 5.42 a 10mm diameter cast iron rod is placed behind a 100mm steel slab, again the Hamming windowed impulse response, though detecting the iron rod, causes deviation from the true target position. Also in Figure 5.41 and Figure 5.42 the superimposition technique and windowing show considerable side lobe reduction from the use of the Inverse DFT alone, with the superimposition technique maintaining a resolution similar to that of the original Inverse DFT impulse response and the windowed impulse response suffering from a loss in resolution.

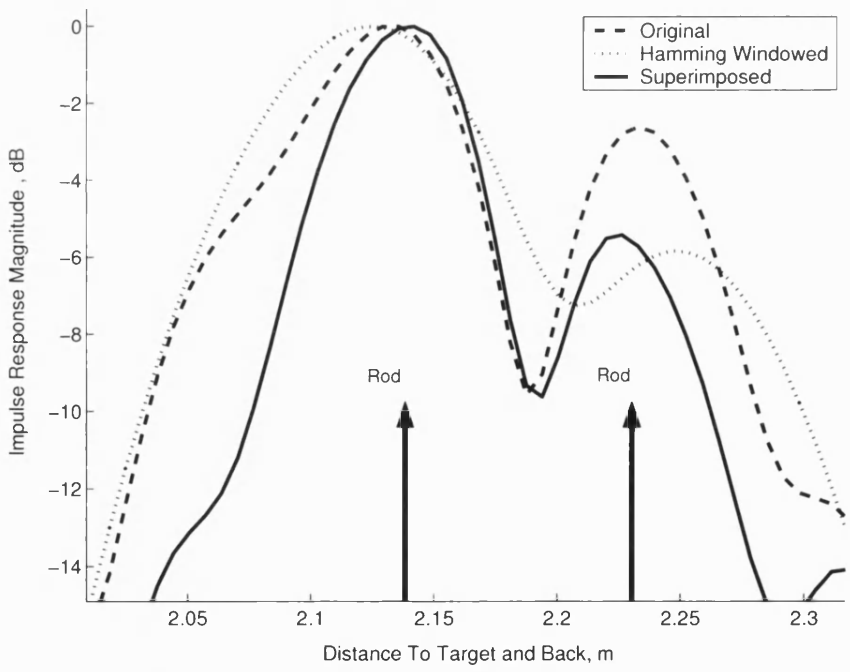

Figure 5.41 Impulse response of reflection off two iron rods that are just being resolved

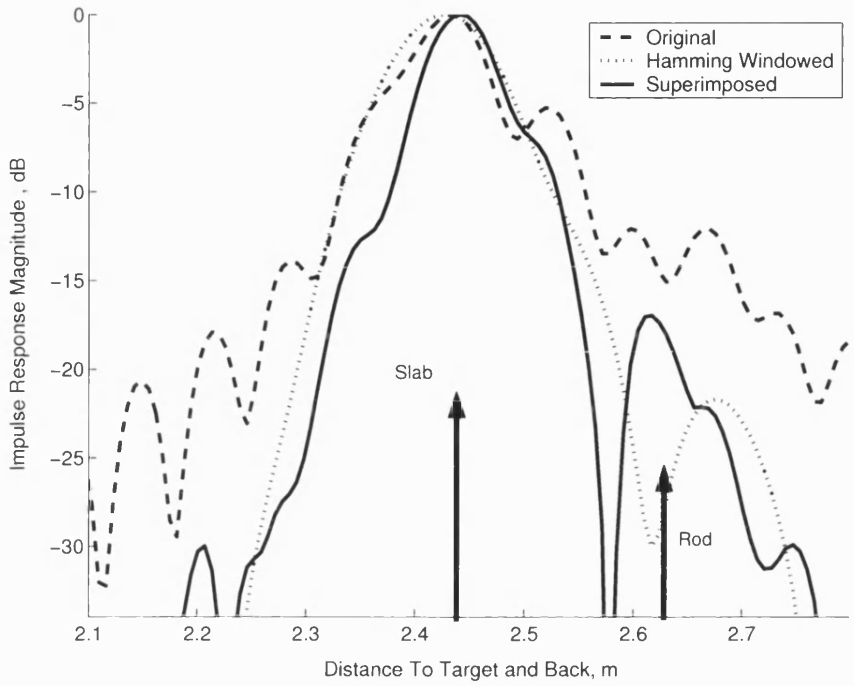

Figure 5.42 Impulse response of reflection off an iron rod placed close to a steel slab

5.5 Prototype GPR System Results

The technique has also been applied to data collected from a previous project using a prototype multi-channel FMCW GPR system [51]. The system was built for buried utility line detection, using a triangulation approach to guide the unit to a position directly above a target and provide a safe digging depth. Some of the properties of the GPR system are listed in Table 5.7 whereas the system's channels in relation to its antenna positions are depicted in Figure 5.43.

In addition a test site was constructed to perform controlled experiments. The test site was a pit with dimensions 3m wide by 5 m long and 2.8 m deep, filled with sharp sand. Figure 5.44 shows the target positions for one of the measurement set ups in a vertical cross section of the sand pit. Target's 1 and 2 are 5cm diameter power cables and Target 3 is a 1.4cm diameter distribution cable.

Parameter	GPR Prototype
Frequency Sweep	250MHz - 750MHz
Sweep Time	0.024s
Sweep Repetition Period	0.131s
Sampling Frequency	6.25kHz

Table 5.7 Prototype GPR system properties

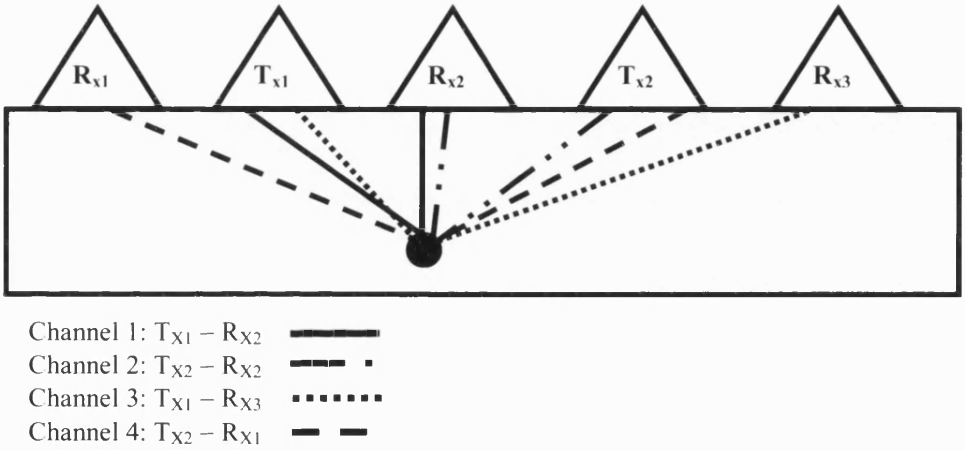

Figure 5.43 Prototype FMCW GPR antenna configuration

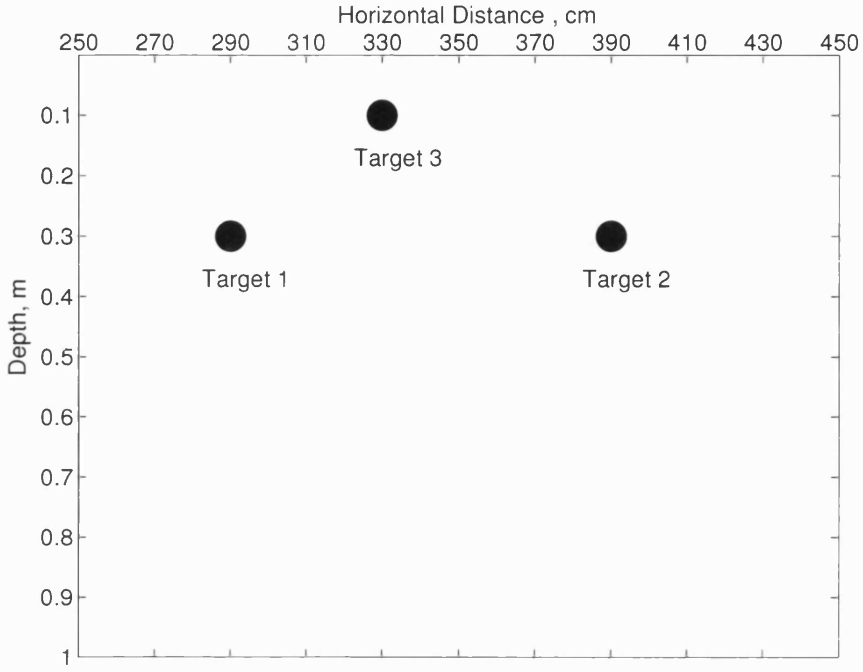

Figure 5.44 GPR target positions

In the project, DFT analysis is used to compute beat spectrums. One of the major data analysis problems encountered resulted from the interaction of the response of the direct coupling signal between the transmitter and receiver and the desired target responses due to spectral leakage. In most cases the direct coupling signal response and the target response nearest to it could not be resolved apart. Eventually subtraction of a reference signal measured from an area of the test pit where no targets were present was used as a means of reducing the direct coupling signal interaction effects. This is demonstrated in Figure 5.45 where the channel 1 beat spectrum before and after subtraction is shown for the measurement taken when the antenna R_{x2} was directly above target 3 at horizontal position 330cm. The spectrum before subtraction fails to resolve apart the responses from target 3 and the direct coupling signal. However, after subtraction the response from target 3 is clearly visible. Although this approach enabled responses to be resolved, in practice such an approach might not be always be possible, as determining where targets are located is part of the problem in the first place.

Figure 5.46, Figure 5.47 and Figure 5.48 show various channel 1 beat spectrum analyses including the superimposition technique for measurements without a reference signal subtraction taken when the antenna R_{x2} is directly over the 3 targets i.e. positions 290cm, 330cm and 390cm as shown in Figure 5.44. The superimposition technique has been set up to target the first two side lobes. The variation used (see section 4.5.1) targets the 1st side lobe using truncation only and the 2nd side lobe using truncation in conjunction with the Hamming window. In all three figures it can be seen that the superimposition technique resolves apart the direct coupling signal from the nearest target response and significantly reduces side lobes levels while maintaining a resolution similar to the DFT processing hence improving overall target detection. In addition the apparent position of Target 2 in the windowed spectrum of Figure 5.46 highlights the extent of error that can be introduced when using window functions in DFT analysis.

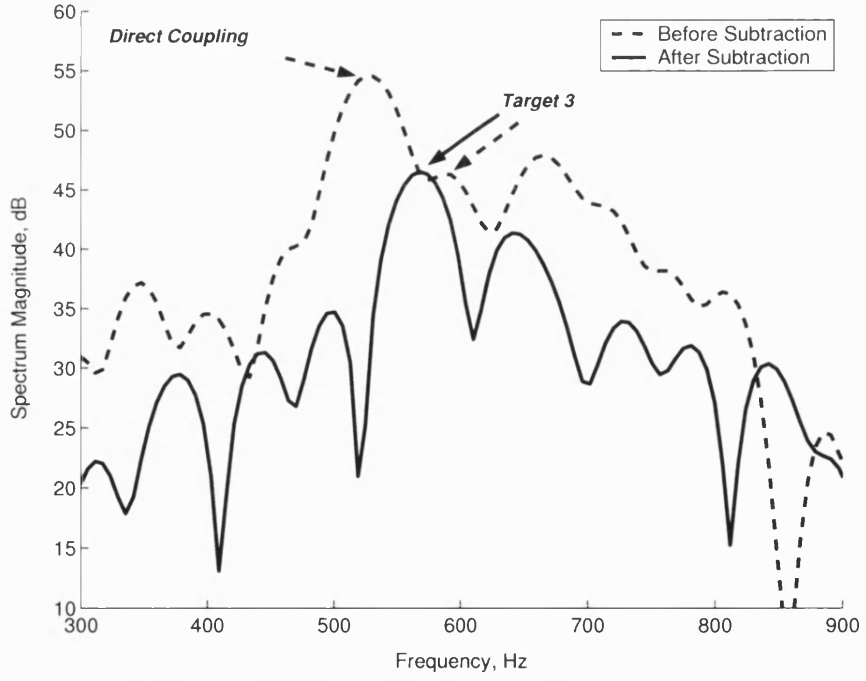

Figure 5.45 Reference signal subtraction applied at horizontal position 330cm

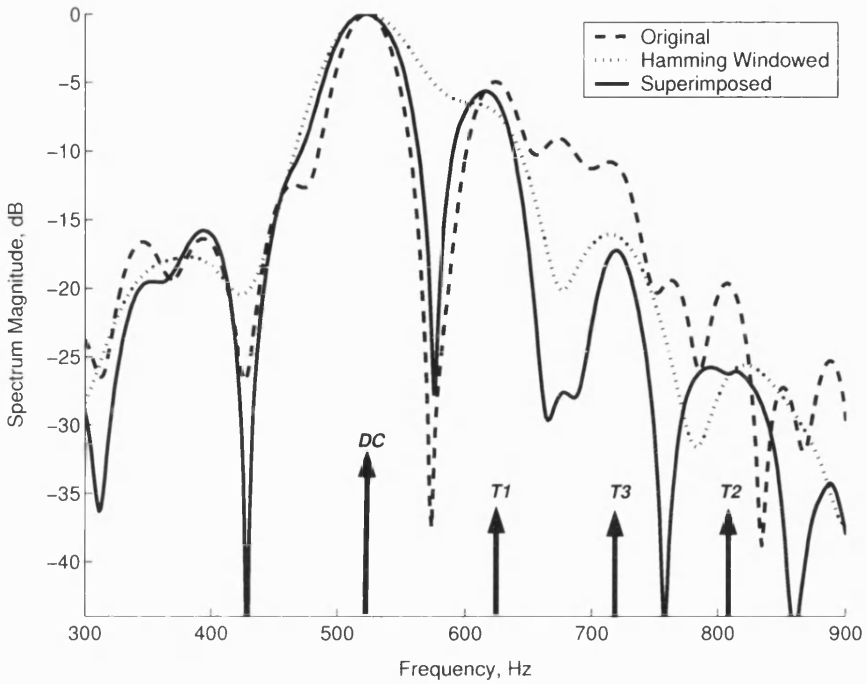

Figure 5.46 Beat spectrum at position 290cm. (Responses; DC - Direct coupling, T1 - Target 1, T2 - Target 2, T3 - Target 3)

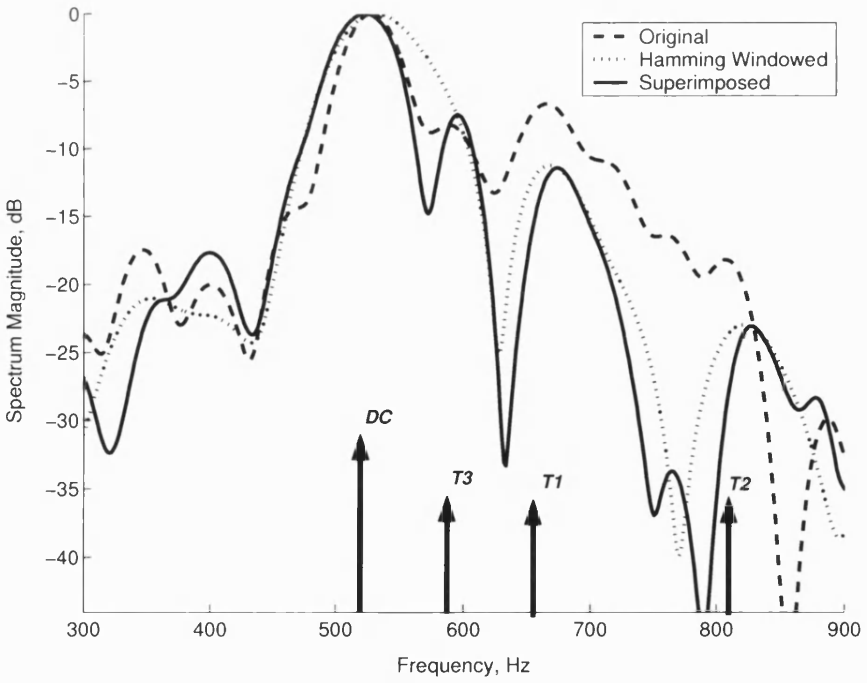

Figure 5.47 Beat spectrum at position 330cm. (Responses; DC - Direct coupling, T1 - Target 1, T2 - Target 2, T3 - Target 3)

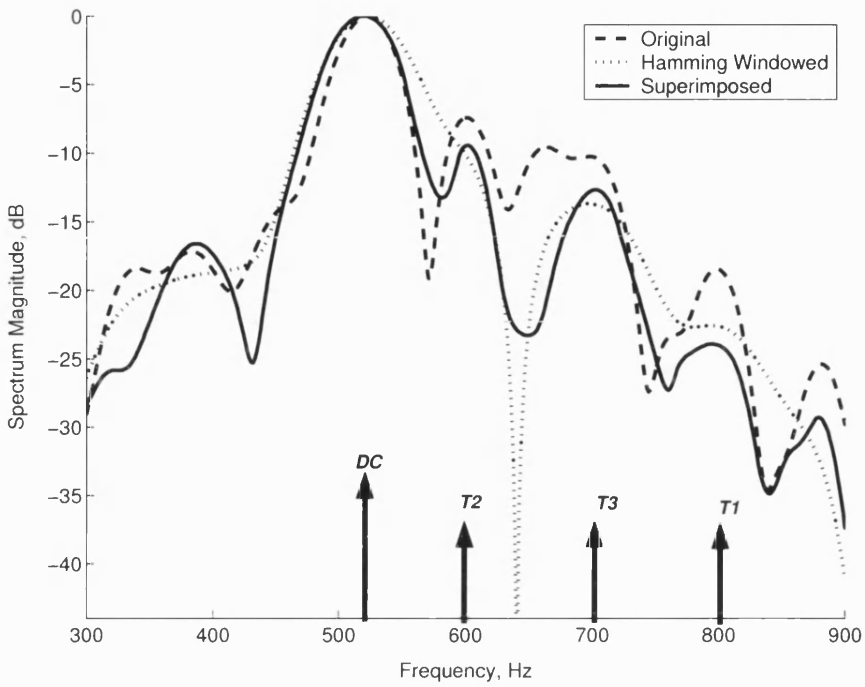

Figure 5.48 Beat spectrum at position 390cm. (Responses; DC - Direct coupling, T1 - Target 1, T2 - Target 2, T3 - Target 3)

5.6 Conclusion

In this chapter some of the areas where the superimposition technique provides improved performance to Fourier analysis have been presented as well as results of applying the technique to both simulated and measured data representing GPR systems. The technique has been shown to achieve significant side lobe reduction and has shown a superior ability to windowing in detecting weak frequency components/targets whilst maintaining resolution.

Chapter 6: Conclusion

6.1 Summary

It is without question that GPR is fast becoming a mature technology. From the early days when specialised/trained operators were needed to read GPR cross sections, more and more derived quantitative numbers such as depth target size and orientation are being extracted from GPR data. Factors that have lead to this growth include the advances in ultra-wide band antennas design, availability of high frequency electronics, advent of efficient digital signal processing techniques and the huge increase in processing power. In particular signal processing has been identified as an area that will bring the next wave of advancements in the GPR technology by workers in the field [9, 10]. Another area of development is in the modelling of electrical properties of materials, which as was shown in Chapter 2, is not a trivial task and is still the subject of much research. With better understanding, more reliable quantitative information could be derived from GPR data. In this section a summary of the thesis is presented.

In Chapter 1 the need for buried utility location technology has been highlighted. Some of the available technologies for locating buried utility lines including GPR systems were compared.

A review of GPR technology was presented in Chapter 2, tracing its history from its early uses to the wide range of applications available today. In addition, the science behind GPR operation was presented. It was shown how Maxwell's equations give rise to a mathematical description of the propagation, reflection and transmission of electromagnetic fields. Finally, losses due to electromagnetic propagation, scattering, antenna properties and spreading were used to provide a mathematical description of the received signal levels in the GPR equation.

In Chapter 3 the theory and operating principle of linear FMCW radar was presented, which led to the description of an analytical form of FMCW from transmission through to reception and processing in the receiver. Also some of the data analysis techniques used for FMCW beat spectrum analysis were discussed. Spectral analysis techniques like the eigen-vector based MUSIC algorithm were shown to provide better resolution than the DFT. However, it was also shown that such techniques require careful and accurate control in order to achieve an accurate spectrum. Also these higher resolution techniques do not provide an accurate representation of the relative strengths between frequency components in a spectrum.

In Chapter 4 an overview of DFT spectrum analysis is provided. The problems of limited spectral resolution and spectral leakage are discussed. It was also highlighted that spectral leakage tends to be worst when detecting weak frequency components in the presence of a close and stronger frequency component which is of major significance to DFT based GPR analysis as high and frequency dependent attenuation in soils more than often results in such situations. The use of special window functions was then presented as a means of combating spectral leakage but at the expense of target resolution.

At the end of Chapter 4 a novel signal processing technique for combating unwanted side lobes as a result of spectral leakage was introduced. The theory behind the technique and the steps involved were presented, followed by some general discussions about the technique. This led on to Chapter 5 where results of applying the technique to both experimental and simulated data were presented.

6.2 Superimposition Technique

In this project a novel signal processing technique, which we call the "Superimposition Technique", has been developed for side lobe suppression in a DFT spectrum. Unlike the windowing approach to side lobe suppression in a DFT spectrum, where an increase in main lobe width is expected, hence leading a loss in resolution, the technique suppresses side lobes whilst maintaining a resolution similar to that of the original DFT spectrum.

The superimposition technique is particularly suitable for improving GPR signal analysis that is based on the DFT, especially where there is a requirement for a large signal bandwidth to provide high resolution e.g. in buried utility detection applications, and there is a high frequency dependent media attenuation of the GPR signal, leading to situations where side lobes from strong target responses mask weaker targets responses or are mistaken as targets responses.

The superimposition technique is based on superimposing multiple DFT analyses from the same data set and averaging the unwanted side lobes. The superimposing of the DFT analyses is based on the fact that regardless of the duration of a signal, a DFT spectrum will always produce main lobes at the fundamental frequency components of the signal and smaller side lobes related to each main lobe with the zero crossing widths of the main lobes and side lobes controlled by the signal duration. Selecting data subsets of particular length from the original signal data set and superimposing their DFT analysis will result in a spectrum where the fundamental frequency components are still maintained as main lobes but the side lobe patterns are changed. The data subsets are chosen such that certain side lobes are broken into an even number of equal and opposite smaller side lobes. A moving average filter of width equal to the combined width of two of the smaller side lobes is then applied to give a cancellation effect on the side lobes. The technique was successfully developed with an additional normalisation step to maintain relative strengths between components after superimposition. Also tests showed that breaking the side lobe being targeted into 2 equal and opposite smaller side lobes provided the best side lobe suppression after averaging.

An improvement to the technique was made by incorporating window functions in the algorithm. We were able to take advantage of the fact that window functions degrade resolution by widening the zero crossing width of main lobes, hence allowing us to select a large subset of the original data to achieve the same effect. This meant that less data and potential target information was discarded and in addition the side lobe suppression properties of the window function also improved the technique's performance.

In Chapter 5 the technique's detection and side lobe suppression capabilities were evaluated. The technique showed improved side lobe levels over pure DFT analysis with

improvements of up to 21 dB and minimal loss in resolution. The incorporation of window functions into the technique provided further side lobe suppression as subsequent side lobes that were not targeted by the technique were also suppressed. Also, even though windows like the Blackman window that degrades resolution by a factor of 3 were used in the technique, the technique always maintained a resolution similar to that of pure DFT analysis. In addition, the use of the window functions in the technique meant that potentially the limits of the technique could be extended by targeting side lobes farther away from the main lobe, especially when the duration–maximum frequency constraint discussed in section 4.5.4 is reached.

The technique was also shown to perform better than both pure DFT analysis and windowed DFT analysis in detecting a weak frequency component in the vicinity of a strong frequency component. The technique was able to resolve a weak frequency component in the vicinity of a strong component at relative strengths of up to 20 to 1 that were not being resolved by DFT analysis or windowed DFT analysis.

The technique was then applied to simulated FMCW GPR beat signals, again the technique was shown to provide superior detection and resolution capabilities over DFT and windowed DFT analysis. The technique was able to detect a target in a high attenuation media that had been undetected by DFT and windowed DFT analysis. Also the technique showed improved resolution when detecting closely located targets.

An experiment was set up to collect data representing a GPR system operating in high attenuation media. High side lobe levels in the data sets measured meant that in most cases only the strongest target could be resolved and detected with a high degree of certainty with pure Inverse DFT (IDFT) analysis. Windowed IDFT analysis improved detection in some cases but always degraded resolution, whereas applying the superimposition technique always improved target detection and again maintained a resolution similar to that of pure DFT analysis. Also the technique showed better accuracy in detecting target positions than windowed Inverse DFT analysis of the measured data when multiple targets were present.

The technique was also applied to measured beat signal data from a prototype GPR system from a previous project [51]. The system employs a reference signal subtraction signal

processing scheme to combat the undesired effects from the direct coupling signal between the system's transmitter and receiver pairs, whereby the side lobes from the strong direct coupling signal response was often masking the nearest target response and window functions were failing to suppress the side lobes and resolve the responses at the same time. Applying the technique not only reduced general side lobe levels but also successively managed to resolve apart the responses from the direct coupling signal and the nearest target responses, again maintaining a resolution similar to that of DFT analysis.

Lastly, while the technique appears to take about 7 times longer to run (bearing in mind this is un-optimised software running on a desktop PC) when targeting 3 side lobes, the actual computation time of 6.1ms is still negligible.

6.3 Future work

The basis for the superimposition technique has been established i.e. truncating data to position zero crossing and main lobe widths followed by superimposition and averaging. However, there still remain areas which could be investigated to further enhance the technique.

The uniform averaging filter used in the technique does not provide total cancellation even on ideal data, alternative averaging filters were discussed and investigated in section 4.5.6 but none were found to perform better. More detailed analysis of the filtering stage of the technique and filter functions is a major area in which the technique performance could be improved.

Other areas of further investigation include whether the unused data after truncation could be used as it could contain useful information, also more work is required to quantify accurately the performance of the technique and find the best variation of the technique for improving DFT analysis.

References

[1] Underground Focus Magazine (2002). [Online] www.undergroundfocus.com (accessed 01/05/2006).

[2] Stampolidis, A., Soupios, P., Vallianatos, F., and Tsokas, G. N., "Detection of leaks in buried plastic water distribution pipes in urban places - a case study," *In 2nd International Workshop on Advanced Ground Penetrating Radar, 2003.*, vol. 1, pp. 120-124, 2003.

[3] Young, J., Caldecott, R., and Peters, L., Jr., "Underground radar research at Ohio state university," *IEEE Antennas and Propagation Society Newsletter*, vol. 21, pp. 4-8, 1979.

[4] Tjora, S., Eide, E., and Lundheim, L., "Evaluation of methods for ground bounce removal in GPR utility mapping," in *Proceedings of the Tenth International Conference on Ground Penetrating Radar (GPR 2004).* vol. 1, 2004, pp. 379-382.

[5] Al-Nuaimy, W., Huang, Y., Nakhkash, M., Fang, M. T. C., Nguyen, V. T., and Eriksen, A., "Automatic detection of buried utilities and solid objects with GPR using neural networks and pattern recognition," *Journal of Applied Geophysics*, vol. 43, pp. 157-165, 2000.

[6] Ciochetto, G., Delbo, S., Gamba, P., and Roccato, D., "Fuzzy shell clustering and pipe detection in ground penetrating radar data," *In Proceedings of the IEEE Geoscience and Remote Sensing Symposium (IGARSS '99)*, vol. 5, pp. 2575-2577 vol.5, 1999.

[7] Michiguchi, Y., Hiramoto, K., Nishi, M., Ootaka, T., and Okada, M., "Advanced subsurface radar system for imaging buried pipes," *IEEE Transactions on Geoscience and Remote Sensing*, vol. 26, pp. 733-740, 1988.

[8] Chignell, R. J., "The radio licensing of GPR systems in europe," *In Proceedings of the Tenth International Conference on Ground Penetrating Radar (GPR 2004).* vol. 1, pp. 3-6, 2004.

[9] Daniels, D. J., *Ground penetrating radar*, 2nd ed. London: Institution of Electrical Engineers, 2004.

[10] Annan, A. P., "GPR - History, Trends and Future Developments," *Subsurface Sensing Technologies and Applications*, vol. 3, pp. 253 - 270, 2002.

[11] Hulsmeyer, C. (1904). Patent No. [165546]. 1904. Germany.

[12] Leimbach, G. and Lowy, H. (1910). Patent No. [237944]. 1910. Germany.

[13] Lowy, H. and Leimbach, G. (1910). Patent No. [246836]. 1910. Germany.

[14] Morey, R. M., "Continous subsurface profiling by impulse radar," *In Engineering Foundations Conference on Subsurface Explorations for Underground Explorations and Heavy Construction.*, Henniker, New Hampshire, pp. 213-232, 1974.

[15] Commercial GPR products (2004). [Online] http://diwww.epfl.ch/lami/detec/gprmaker.html (accessed 13/05/2006).

[16] Earp, S. L., Hughes, E. S., Elkins, T. J., and Vickers, R., "Ultra-wideband ground-penetrating radar for the detection of buried metallic mines," *IEEE Aerospace and Electronic Systems Magazine*, vol. 11, pp. 30-39, 1996.

[17] Daniels, D. J., Brooks, D., Dittmer, J., Mitchell, O., and Hunt, N., "Wide swathe multi-channel GPR systems for mine detection," *In RADAR 2002*, pp. 210-216, 2002.

[18] Lanka, M., Butler, A., and Sterling, R., "Use of approximate reasoning techniques for locating underground utilities," *Tunnelling and Underground Space Technology*, vol. 16, pp. 13-31, 2001.

[19] Instanes, A., Lonne, I., and Sandaker, K., "Location of avalanche victims with ground-penetrating radar," *Cold Regions Science and Technology*, vol. 38, pp. 55-61, 2004.

[20] Modroo, J. J. and Olhoeft, G. R., "Avalanche rescue using ground penetrating radar," *In Proceedings of the Tenth International Conference on Ground Penetrating Radar (GPR 2004).* pp. 785-788, 2004.

[21] Fauchard, C., Derobert, X., Cariou, J., and Cote, P., "GPR performances for thickness calibration on road test sites," *NDT & E International*, vol. 36, pp. 67-75, 2003.

[22] Saarenketo, T. and Scullion, T., "Road evaluation with ground penetrating radar," *Journal of Applied Geophysics*, vol. 43, pp. 119-138, 2000.

[23] Hugenschmidt, J., "Concrete bridge inspection with a mobile GPR system," *Construction and Building Materials*, vol. 16, pp. 147-154, 2002.

[24] Heiler, M., McNeil, S., and Garrett, J., "Ground penetrating radar for highway and bridge deck condition assessment and inventory," *NDT & E International*, vol. 30, pp. 333, 1997.

[25] Sussmann, T. R., Selig, E. T., and Hyslip, J. P., "Railway track condition indicators from ground penetrating radar," *NDT & E International*, vol. 36, pp. 157-167, 2003.

[26] Hugenschmidt, J., "Railway track inspection using GPR," *Journal of Applied Geophysics*, vol. 43, pp. 147-155, 2000.

[27] Tohge, M., Karube, F., Kobayashi, M., Tanaka, A., and Katsumi, I., "The use of ground penetrating radar to map an ancient village buried by volcanic eruptions," *Journal of Applied Geophysics*, vol. 40, pp. 49-58, 1998.

[28] Hruska, J. and Fuchs, G., "GPR prospection in ancient Ephesos," *Journal of Applied Geophysics*, vol. 41, pp. 293-312, 1999.

[29] Perez Gracia, V., Canas, J. A., Pujades, L. G., Clapes, J., Caselles, O., Garcia, F., and Osorio, R., "GPR survey to confirm the location of ancient structures under the

Valencian Cathedral (Spain)," *Journal of Applied Geophysics*, vol. 43, pp. 167-174, 2000.

[30] Elkhetali, S. I., "Ground penetrating radar as an assisting tool for prospecting for oil," *In*, vol. 2, pp. 730-731 vol.2, 2003.

[31] Rashed, M., Kawamura, D., Nemoto, H., Miyata, T., and Nakagawa, K., "Ground penetrating radar investigations across the Uemachi fault, Osaka, Japan," *Journal of Applied Geophysics*, vol. 53, pp. 63-75, 2003.

[32] Nakashima, Y., Zhou, H., and Sato, M., "Estimation of groundwater level by GPR in an area with multiple ambiguous reflections," *Journal of Applied Geophysics*, vol. 47, pp. 241-249, 2001.

[33] Harari, Z., "Ground-penetrating radar (GPR) for imaging stratigraphic features and groundwater in sand dunes," *Journal of Applied Geophysics*, vol. 36, pp. 43-52, 1996.

[34] Barbin, Y., Nicollin, F., Kofman, W., Zolotarev, V., and Glotov, V., "Mars 96 GPR program," *Journal of Applied Geophysics*, vol. 33, pp. 27-37, 1995.

[35] Lanbo, L. and Lieyuan, Z., "GPR signal analysis: can we get deep-penetration and high-resolution simultaneously?," *In Proceedings of the Tenth International Conference on Ground Penetrating Radar (GPR 2004).* vol. 1, pp. 263-265, 2004.

[36] Daniels, D. J., "Ultrawideband radar detection of buried objects," *In IEEE International Geoscience and Remote Sensing Symposium*, vol. 3, pp. 1278-1281, 1997.

[37] Kingsley Simon, P. and Quegan, S., *Understanding Radar Systems*: McGraw, 1992.

[38] Kraus, J. D., *Electromagnetics*, 4th ed. ed: McGraw-Hill, 1991.

[39] "Electromagnetic Wave" Created by: PIRA-Organisation. [Online] http://www.wfu.edu/physics/pira/ResourceCD/ResourceImages/PhysicsDrawings/EandM_Wave.gif (accessed 16/05/2006)

[40] Alattar, A., Scott, H. F., and Daniels, D. J., "Wideband Measurement of Microwave Characteristics of Soils," *Electronics Letters*, vol. 18, pp. 194-196, 1982.

[41] Dobson, M. C., Ulaby, F. T., Hallikainen, M. T., and Elrayes, M. A., "Microwave Dielectric Behavior of Wet Soil .2. Dielectric Mixing Models," *IEEE Transactions on Geoscience and Remote Sensing*, vol. 23, pp. 35-46, 1985.

[42] Fano, W. G. and Trainotti, V., "Dielectric properties of soils," *In IEEE Conference on Electrical Insulation and Dielectric Phenomena*, pp. 75-78, 2001.

[43] Scott, W. R., Jr. and Smith, G. S., "Measured electrical constitutive parameters of soil as functions of frequency and moisture content," *IEEE Transactions on Geoscience and Remote Sensing*, vol. 30, pp. 621-623, 1992.

[44] Deloor, G. P., "The Dielectric-Properties of Wet Materials," *IEEE Transactions on Geoscience and Remote Sensing*, vol. 21, pp. 364-369, 1983.

[45] Peplinski, N. R., Ulaby, F. T., and Dobson, M. C., "Dielectric-Properties of Soils in the 0.3-1.3-Ghz Range," *IEEE Transactions on Geoscience and Remote Sensing*, vol. 33, pp. 803-807, 1995.

[46] Soutsos, M. N., Bungey, J. H., Millard, S. G., Shaw, M. R., and Patterson, A., "Dielectric properties of concrete and their influence on radar testing," *NDT & E International*, vol. 34, pp. 419-425, 2001.

[47] Adams, M. J., *An introduction to optical waveguides*. Chichester: Wiley, 1981.

[48] Hallikainen, M. T., Ulaby, F. T., Dobson, M. C., Elrayes, M. A., and Wu, L. K., "Microwave Dielectric Behavior of Wet Soil .1. Empirical-Models and Experimental-Observations," *IEEE Transactions on Geoscience and Remote Sensing*, vol. 23, pp. 25-34, 1985.

[49] Yamaguchi, Y., Mitsumoto, M., Sengoku, M., and Abe, T., "Synthetic aperture FM-CW radar applied to the detection of objects buried in snowpack," *IEEE Transactions on Geoscience and Remote Sensing,* , vol. 32, pp. 11-18, 1994.

[50] Carr, A. E., Cuthbert, L. G., and Olver, A. D., "Digital Signal-Processing for Target Detection in FMCW Radar," *IEE Proceedings-F Radar and Signal Processing*, vol. 128, pp. 331-336, 1981.

[51] Zhang, X., "Modelling of FMCW ground penetrating radar" PhD, University of Bath, 1997.

[52] Deng, R. and Liu, C., "FM-CW radar performance in a lossy layered medium," *Journal of Applied Geophysics*, vol. 42, pp. 23-33, 1999.

[53] Liau, T. F., Carr, A. G., and Cuthbert, L. G., "Using Non-Fourier Techniques in Signal-Processing for an FMCW Hidden-Object Detection Radar," *Electronics Letters*, vol. 22, pp. 466-467, 1986.

[54] Bouchard, M., Gingras, D., de Villers, Y., and Potvin, D., "High Resolution Spectrum Estimation of FMCW Radar Signals," *In IEEE Seventh Workshop on Statistical Signal and Array Processing*, pp. 421-424, 1994.

[55] Shrestha, S. M. and Arai, I., "High resolution image reconstruction by GPR using MUSIC and SAR processing method for landmine detection," *In Proceedings of the IEEE International Geoscience and Remote Sensing Symposium (IGARSS '03)*, vol. 4, pp. 2921-2923 vol.4, 2003.

[56] Shrestha, S. M., Arai, I., Miwa, T., and Tomizawa, Y., "Signal processing of ground penetrating radar using super resolution technique," *In 2001 IEEE Radar Conference*, Atlanta, GA pp. 300-305, 2001.

[57] Prabhu, K. M. M. and Bagan, K. B., "Resolution capability of nonlinear spectral-estimation methods for short data lengths," *IEE Proceedings F Radar and Signal Processing*, vol. 136, pp. 135-142, 1989.

[58] Marple, S. L., *Digital spectral analysis with applications*. Englewood Cliffs, N.J.: Prentice-Hall, 1987.

[59] Burdic, W. S., *Radar signal analysis*. Englewood Cliffs, N.J.: Prentice-Hall, 1968.

[60] Olver, A. D. and Cuthbert, L. G., "FMCW Radar for Hidden Object Detection," *IEE Proceedings-F Radar and Signal Processing*, vol. 135, pp. 354-361, 1988.

[61] Farmer, G. A., Cuthbert, L. G., Olver, A. D., and Botros, A. Z., "Distinguishing between Types of Hidden Objects Using an FMCW Radar," *Electronics Letters*, vol. 20, pp. 824-825, 1984.

[62] Looney, C. G., *Pattern recognition using neural networks : theory and algorithms for engineers and scientists*. New York ; Oxford: Oxford University Press, 1997.

[63] Hyoung-sun, Y. and Chi-chih, C., "Neural detection for buried pipe using fully polarimetric GPR," *In Proceedings of the Tenth International Conference on Ground Penetrating Radar (GPR 2004)*. vol. 1, pp. 303-306, 2004.

[64] Gamba, P. and Lossani, S., "Neural detection of pipe signatures in ground penetrating radar images," *IEEE Transactions on Geoscience and Remote Sensing*, vol. 38, pp. 790-797, 2000.

[65] Yang, L., Zhenghe, F., Yanhong, X., and Jingyu, H., "A neural network algorithm for signal processing of LFMCW or IFSCW system," *In Asia Pacific Microwave Conference*, vol. 3, pp. 900-903 vol.3, 1999.

[66] Olver, A. D., Cuthbert, L. G., Nicolaides, M., and Carr, A. G., "Portable FMCW radar for locating buried pipes," *In IEE Radar 82 Conference*, vol. 216, pp. 413-418, 1982.

[67] Porat, B., *A course in digital signal processing*. New York ; Chichester: John Wiley, 1997.

[68] Denniss, P. and Gibbs, S. E., "Solid-State Linear FM/CW RADAR Systems - Their Promise and Their Problems," *In 1974 S-MTT International Microwave Symposium Digest*, vol. 74, pp. 340-342, 1974.

[69] Wang Dong, J., Hu, X., and Ruan Wen, J., "Analysis of the influence of the FM non-linearity on the range resolution of LFMCW radar," *In 1999 Asia Pacific Microwave Conference*, vol. 3, pp. 714-717 vol.3, 1999.

[70] Xu Dong, L., Zhen Rong, W., and Ming Hua, X., "A solution for the nonlinearity of LFM-CW system," *In Proceedings of the 2nd International Conference on Microwave and Millimeter Wave Technology (ICMMT 2000)*, pp. 650-653, 2000.

[71] Fuchs, J., Ward, K. D., Tulin, M. P., and York, R. A., "Simple techniques to correct for VCO nonlinearities in short range FMCW radars," *In IEEE MTT-S International Microwave Symposium Digest*, vol. 2, pp. 1175-1178, 1996.

[72] Kang, B. K., Kwon, H. J., Mheen, B. K., Yoo, H. J., and Kim, Y. H., "Nonlinearity compensation circuit for voltage-controlled oscillator operating in linear frequency sweep mode," *IEEE Microwave and Guided Wave Letters, [see also IEEE Microwave and Wireless Components Letters]*, vol. 10, pp. 537-539, 2000.

[73] Cooley, J. W. and Tukey, J. W., "An algorithm for the machine calculation of complex Fourier series," *Math Computing*, vol. 9, pp. 297–301, 1965.

[74] Chan, S. C. and Ho, K. L., "On indexing the prime factor fast Fourier transform algorithm," *IEEE Transactions on Circuits and Systems*, vol. 38, pp. 951-953, 1991.

[75] Bruun, G., "z-transform DFT filters and FFT's," *IEEE Transactions on Acoustics, Speech, and Signal Processing* vol. 26, pp. 56-63, 1978.

[76] Rader, C. M., "Discrete Fourier transforms when the number of data samples is prime," *Proceedings of the IEEE*, vol. 56, pp. 1107-1108, 1968.

[77] Adams, J. W., "A new optimal window [signal processing]," *IEEE Transactions on Signal Processing*, vol. 39, pp. 1753-1769, 1991.

[78] Jaskula, M., "New windows family based on modified Legendre polynomials," *In 19th IEEE Instrumentation and Measurement Technology Conference*, vol. 1, pp. 553-556 vol.1, 2002.

[79] Harris, F. J., "On the use of windows for harmonic analysis with the discrete Fourier transform," *Proceedings of the IEEE*, vol. 66, pp. 51-83, 1978.

[80] Cadzow, J. A., *Foundations of digital signal processing and data analysis*. New York: Macmillan, 1987.

[81] Dolph, C. L., "A Current Distribution for Broadside Arrays Which Optimizes the Relationship between Beam Width and Side-Lobe Level," *Proceedings of the IRE*, vol. 34, pp. 335-348, 1946.

[82] Kuo, F. F.-k. and Kaiser, J. F., *System analysis by digital computer.* New York ; London: Wiley, 1966.

[83] Kaiser, J. and Schafer, R., "On the use of the I0-sinh window for spectrum analysis," *IEEE Transactions on Acoustics, Speech, and Signal Processing* vol. 28, pp. 105-107, 1980.

[84] Saramaki, T., "A class of window functions with nearly minimum sidelobe energy for designing FIR filters," *In IEEE International Symposium on Circuits and Systems*, Portland, OR, vol. 1, pp. 359-362, 1989.

[85] Fung, T., Sarkar, T., and Weiner, D., "A novel window for harmonic analysis," *IEEE Transactions on Acoustics, Speech, and Signal Processing*, vol. 29, pp. 177-188, 1981.

[86] Hanna, M. T., "Windows with rapidly decaying sidelobes and steerable sidelobe dips," *IEEE Transactions on Signal Processing*, vol. 42, pp. 2037-2044, 1994.

[87] Zhong, J., Han, Z., and Lu, W., "Design of windows with steerable sidelobe dips," *IEEE Transactions on Signal Processing*, vol. 40, pp. 1452-1459, 1992.

[88] Jan, J. C., *Digital signal filtering, analysis and restoration.* London: Institution of Electrical Engineers, 2000.

[89] Matlab Version 6.5.0.180913a Release 13 (2002). The MathWorks, Inc.

[90] Kong, F.-N. and By, T. L., "Performance of a GPR system which uses step frequency signals," *Journal of Applied Geophysics*, vol. 33, pp. 15-26, 1995.

[91] Lightning 3700 Family Vector Network Analyzers (2003). [Online] http://www.eu.anritsu.com/files/11410-00248rb.pdf (accessed 01/05/2006).

[92] Maida, A. W., Pennock, S. R., and Shepherd, P. R., "Detection and Resolution Enhancement of Closely Spaced Targets in Ground Penetrating Radar," *In Proceedings of the Eleventh International Conference on Ground Penetrating Radar (GPR 2006).* vol. 1, 2006.

[93] Maida, A., Pennock, S., and Shepherd, P., "Improving ground penetrating radar signal analysis through FFT superimposition," *In 2005 IEEE Antennas and Propagation Society International Symposium*, vol. 4B, pp. 118-121, 2005.

[94] Maida A. W, Shepherd P. R, and R, P. S., "Fourier and Eigen Analysis Based Spectral Estimation for Ground Penetrating Radar," *In British National Symposium of URSI*, University of Bath, UK, 2004.

[95] Maida, A. W., Pennock, S. R., and Shepherd, P. R., "Modelling Soil Attenuation Effects in Ground Penetrating Radar Systems," *In Postgraduate Research in Electronics, Photonics, Communications and Software Conference (PREP 2004)*, University of Hertfordshire, UK., 2004.

Appendix

This section contains a list of presentations given at various conferences related this research project. The abstracts for the presentations are also attached of the end of this thesis.

1. Oral Presentations
    a. "Detection and Resolution Enhancement of Closely Spaced Targets in Ground Penetrating Radar" presented at the 11th International Conference on Ground Penetrating Radar, Ohio State University, Columbus Ohio, USA.19-22 June 2006 [92].

    b. "Improving Ground Penetrating Radar Signal Analysis through FFT Superimposition" presented at the IEEE AP-S International Symposium Omni Shoreham Hotel, Washington DC, USA. 3-8 July 2005 [93].

2. Poster Presentations
    a. "Fourier and Eigen Analysis Based Spectral Estimation for Ground Penetrating Radar" presented at the URSI National Symposium, University of Bath, UK. 5-6 July 2004 [94].

    b. "Modelling Soil Attenuation Effects in Ground Penetrating Radar Systems" presented at Postgraduate Research in Electronics, Photonics, Communications and Software Conference, University of Hertfordshire, UK. 5-7 April 2004 [95].

MODELLING SOIL ATTENUATION EFFECTS IN GROUND PENETRATING RADAR SYSTEMS

A W Maida, S R Pennock, P R Shepherd. Dept. of Electronic and Electrical Engineering, University of Bath, UK.

Key words to describe the work: Frequency Modulated Continuous Wave (FM-CW), Ground penetrating radar (GPR), Buried Objects, Utility lines.

Key Results: The results show how the extent to which frequency dependent material attenuation loss affect can affect the performance of an FM-CW GPR.

How does the work advance the state-of-the-art?: Identifying and understanding performance limiting factors will aid the development of future signal processing to enhance target detection in FMCW GPR systems.

Motivation (problems addressed): Under unfavourable conditions the performance of the FM-CW radar can be severely degraded. Conventional signal processing techniques are not always suited to such situations

1.Introduction

Ground Penetrating Radar (GPR) is a non-destructive electromagnetic technique used for the detection of objects beneath the ground or within an opaque structure. Over the years GPR has found use in numerous fields such as civil engineering, archaeology, geophysics and remote sensing. More recently GPR has been used by construction workers and utility company maintenance personnel to help prevent third party damage to existing buried utility lines while carrying out their work in areas where there is insufficient information on the location of buried utility lines. When designing a GPR system the use of high frequencies is required for high resolution. At the same time, the maximum depth that the electromagnetic waves can penetrate in a given lossy medium drops with increasing frequency due to propagation losses. Therefore depending on the intended system use it is necessary to reach a compromise between resolution requirements and depth of penetration when choosing operating frequencies. For applications such as buried utility line detection, the required penetration depth is usually within a metre or two, hence permitting the use of high frequencies to achieve high resolution. The FM-CW GPR is particularly suited for this type of GPR application. The theory of FMCW radars is well known and can be found in [1] and [2].

2.Attenuation in the propagating medium

The GPR response is a function of the electromagnetic properties: dielectric permittivity ε_c, magnetic permeability μ_c and electrical conductivity σ_c of the propagation medium. For most lossy media encountered in GPR applications, the effect of magnetic permeability is usually negligible. On the other hand the dielectric permittivity is a complex value and a function of angular frequency ω:

$$\varepsilon_c = \varepsilon' - j\varepsilon'' \equiv \varepsilon - j\frac{\sigma_c}{\omega} \tag{1}$$

The real part is the permittivity of the material, which is a measure of the material's electric field storage capacity while the imaginary part of the dielectric permittivity is related to the electrical conductivity (σ_c) of the material. The permittivity and conductivity determine the material attenuation factor α of the medium, as shown in Eq.2.

$$\alpha = \omega\left[\frac{\mu\varepsilon'}{2}\left(\sqrt{1+\left(\frac{\varepsilon''}{\varepsilon'}\right)}-1\right)\right]^{1/2} \tag{2}$$

The material attenuation loss, which is determined by the attenuation factor, is one of the major limiting factors on the depth penetration of an FM-CW GPR. The material attenuation loss for can range from 10-600dB/m at 1GHz [1]. Hence even small

penetration depths could be difficult to achieve in certain soils. In this paper results of an investigation of the effect of the material attenuation loss on the systems ability to detect targets are presented. The results are based on simulation of an FM-CW GPR.

3.Simulation

The simulation is based on an analytical model of an FM-CW system. Ignoring the other losses associated with the received signal, the receiver output, known as the beat signal, is given as (3) where N targets are present:

$$S_b(t)=\sum_{i=1}^{N} AA_i' Cos\left[2\pi\left(M\tau_i t + f_o\tau_i - \frac{M}{2}\tau_i^2\right)\right] \quad (3)$$

In Eq (3) τ_i is the delay to the ith target, M is the modulation rate, f_o is the centre of the frequency sweep and $A_i' = e^{-2\alpha r}$ is the material attenuation loss for the ith target at range r. The frequencies ($f_{bi} = M\tau_i$) that make up the beat signal are dependent on the delay τ_i and hence the target range. Identifying these beats frequencies can be done by identifying the peaks of the Fourier transform of the beat signal with respect to the frequency sweep time T_s:

$$S_b(f)=\sum_{i=1}^{N} \frac{AA_i' T_s}{2} e^{2\pi f_o \tau_i} Sinc[\pi(f - f_{bi})T_s] \quad (4)$$

4.Results

The beat signal of an FM-CW radar system operating in the 1-2GHz range, with a sweep time of 5ms is modelled. Fig. 1. shows the target scenario being simulated. In Fig. 2(a), the computed spectrum of the receiver output is shown when the medium is lossless (i.e. $\sigma_c = 0$). The three distinct peaks in the spectrum correspond to the three targets. In Fig. 2(b) the output spectrum is shown when $\sigma_c = .002S/m$. In this case only the nearest two targets can be seen clearly. This is because the reflected wave due to the third target is absorbed by the medium and is too weak to be detected due to masking by sidelobes of the nearer targets. In Fig. 2(c) $\sigma_c = .005S/m$, here only the nearest target can be detected. The waves reflected by the other two targets have been absorbed by the medium

5.Conclusion

The receiver output of an FMCW GPR has been simulated. The simulation results have shown how the material attenuation loss affects the systems performance. Results show that as electrical conductivity of the medium increases, the system's ability to detect the presence of targets is degraded. The results also show the sensitivity of the FM-CW GPR to a slight change of the medium's conductivity from 0.002S/m when two the targets could be detected to 0.003S/m when only the nearest target could be detected.

6.References

[1] Daniels, D. J.: Surface Penetrating Radar (IEE Radar, Sonar, Navigation and Avionics, 1996)

[2] Yamaguchi, Y., Mitsumoto, M., Sengoku, M., Abe, T.: Synthetic aperture FM-CW radar applied to the detection of objects buried in snowpack. IEEE Trans on Geoscience and Remote Sensing, Vol 32,1994, Pages: 11-18.

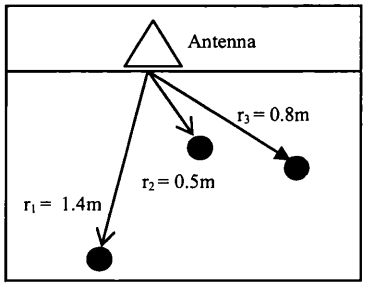

Fig. 1. Simulated Scenario: 3 Targets in soil with relative permitivity $\varepsilon_r = 8$ at 100MHz

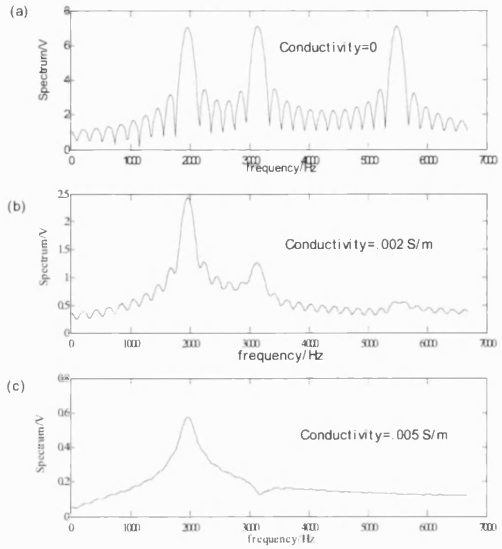

Fig. 2. The simulated spectrum of the receiver output of an FM-CW radar for the target scenario in Fig. 1. for different conductivities. (a) Conductivity =0 (b) Conductivity $= 10^{-2}$ S/m (c) Conductivity = 10^{-1}S/m

FOURIER AND EIGEN ANALYSIS BASED SPECTRAL ESTIMATION FOR GROUND PENETRATING RADAR

A W Maida, S R Pennock, P R Shepherd
Department of Electrical and Electronic Engineering, University of Bath, UK

Abstract

Underground Utility lines and other buried objects sometimes pose serious problems when excavation or construction is carried out in and around their vicinity. Considerable research has been carried out into the use of Frequency Modulated Continuous Waveform (FM-CW) Ground Penetrating Radar (GPR) for locating buried utility lines.

Despite its inherent resolution limitations, most conventional FM-CW radars use the computationally efficient and unsupervised Fast Fourier Transform (FFT) for spectral analysis of the radar beat signal. Ideally, each maximum in the beat signal spectrum corresponds to a reflecting target, but high media attenuation rates means weaker target reflections are often shadowed by stronger target reflections. Spectral estimation techniques based on eigen analysis such as the Multiple Signal Classification (MUSIC) algorithm though more complex and require strict supervision (i.e. an accurate model order selection) have been shown to provide up to three times improved resolution over FFT.

FM-CW radar signals contain clutter noise and non-linearity effects usually at very low SNR (signal to noise ratio). This makes standard MUSIC model order selection based on comparing the relative magnitudes of eigen values of the eigen decomposition of the data autocorrelation matrix unsuitable.

In this work we highlight the need for different approach to model order selection and propose a mean square error approach. In addition we have compared the performance of the MUSIC algorithm with FFT on simulated GPR data and real GPR data. In particular we have looked at the resolution capability and accuracy of each method. We have also investigated the effects of windowing on the resolution of both the MUSIC algorithm and FFT.

Improving Ground Penetrating Radar Signal Analysis through FFT Superimposition

Aminu Maida*, Stephen Pennock, and Peter Shepherd
Dept of Electrical & Electrical Engineering, University of Bath, Bath, UK
http://www.bath.ac.uk/elec-eng/tsar

This paper deals with the signal analysis problem encountered with Ground Penetrating Radar (GPR) applications that use the Fast Fourier Transform (FFT). A technique for improved signal analysis based on superimposing multiple FFT analyses from the same data is presented. Results from applying the technique are seen to reduce the side lobes with minimal increase in main lobe width.

Introduction

Ground Penetrating Radar (GPR) signal processing often relies on Fast Fourier Transform (FFT) spectrum analysis to identify and resolve targets. The FFT is a well known and extensively used spectral analysis technique which, while computationally efficient, does have its limitations. In particular there is the problem in distinguishing the side lobes of a target and the main lobe of a weaker target. In Frequency Modulated Continuous Waveform (FM-CW) GPR applications signals experience frequency dependent attenuation and side lobes of stronger frequency components can easily result in false frequency detections [1]. Window functions [2] can be used to reduce side lobes at the expense of the widths of the main lobe and therefore resolution capability. We propose a signal processing technique for side lobe reduction whereby multiple analyses of the same data are superimposed and the resultant FFT spectrum averaged.

Signal Processing Model

For a sine wave of finite duration, τ, with frequency ω_0 (Eqn 1), its corresponding Fourier Transform is a Sinc function described by Eqn 2

$$s(t) = A\,Sin(\omega_0 t) \times rect\left\{\frac{t}{\tau} - \frac{\tau}{2}\right\} \tag{1}$$

$$S(f) = \exp(-j\omega\tau)\frac{\tau}{2}A\left\{Sinc\left[\frac{\omega+\omega_0}{2\pi}\tau\right] + Sinc\left[\frac{\omega-\omega_0}{2\pi}\tau\right]\right\} \tag{2}$$

The main lobe position is always determined by the signal frequency whereas the positions of the side lobes are determined by the duration of the signal, occurring at intervals of $1/\tau$ from the centre of the main lobe. The technique we propose involves breaking this first side lobe in the spectrum of the original signal into smaller equal duration side lobes by superimposing FFT spectra from truncated versions of the original signal. To break a side lobe into N smaller

side lobes we would require *N-1* truncated versions of the signals. Each signal will have a duration such that the first zero crossing from the main lobe in its FFT spectrum will occur at a certain position within the first side lobe of the FFT spectrum of the original signal. These positions will be evenly spaced so that the resulting side lobes are of equal widths. For *N* smaller side lobes the spacing is given by

$$\Delta = \frac{1}{N} \tag{3}$$

It follows that *N-1* truncated versions of the original signal are required with durations:

$$\tau_i = \tau_0 \frac{1}{1+\Delta i} \text{ , for } i = 0..N-1 \tag{4}$$

Where τ_i is the duration of the i^{th} truncated signal and τ_0 is the duration of the original signal

Superimposition is then followed by averaging over the width of two resulting side lobes, i.e. 2Δ

Eqn's 5 to 10 describe the signal processing steps. The first step involves normalizing the original signal and its truncated version, as the finite duration of the signals and sampling affects the spectra by introducing scaling factors. Eqn 2 has shown the complex factor introduced due to the finite duration of the signal whereas Eqn's 5 and 6 describe the factor introduced in the spectrum due to sampling. The resulting normalized signal is given in Eqn 7, Eqn 8 describes the superimposition part of the technique and Eqn 9 describes a second normalization step which is required to maintain relative magnitudes between frequency components with unequal strengths after superimposition. The averaging is done using a moving average filter as described in Eqn 10. The processing technique described is linear; therefore using linear superimposition the technique can be applied to a multi-frequency signal.

$$s(nT) = \sum_{n=-\infty}^{n=+\infty} \delta(t-nT)s(t) \tag{5}$$

$$S(k) = \frac{1}{T} \sum_{n=-\infty}^{n=+\infty} \delta\left(\omega - \frac{2\pi kn}{NT}\right) S(\omega) \tag{6}$$

$$S_i(\omega) = \frac{A_i \tau_i}{2T} \exp\left(\frac{-j\omega\tau_i}{2}\right)\left\{Sinc\left[\frac{\omega+\omega_0}{2\pi}\tau_i\right] + Sinc\left[\frac{\omega-\omega_0}{2\pi}\tau_i\right]\right\} \tag{7}$$

$$S'(\omega) = \prod_{i=0}^{n}\left[\frac{2T}{\tau_i}\exp\left(\frac{j\omega\tau_i}{2}\right)S_i(\omega)\right] \tag{8}$$

$$S''(\omega) = \sqrt[n]{|S'(\omega)|} \times \angle S'(\omega) \tag{9}$$

$$\overline{S}_k = \frac{1}{m} \sum_{i=k-m}^{k} S_i'' \tag{10}$$

Where

τ_0 is the duration of the original signal

$\tau_i : i > 0$ is the duration of the i^{th} truncated

T is the sampling period

N is the number of points used in the FFT algorithm

$S'(\omega)$ is the superimposed signal

$S''(\omega)$ is the normalized superimposed signal ready for averaging

S_i'' is the i^{th} sample of the normalized superimposed signal , $S''(\omega)$

$\overline{S}_k$ is the k^{th} average of the last m samples of S_i''

Results

We present the results of applying the technique to simulated and measured data. In both cases the first side lobes from the main lobe were broken into two, therefore only one truncated version of data was required with length two-thirds of the original data according to Eqn's 3 and 4.

The simulated data is a sampled signal consisting of two unequal strength frequencies at 4 kHz and 4.3 kHz. Fig.1 shows the results of the superimposition technique spectrum being compared to Bartlett Windowed [2] version of the signal spectrum using a FFT with 4096 points. The Bartlett window fails to resolve the two frequencies and so suffers from a clear loss in resolution, whereas the superimposition technique clearly identifies the two signals. It can also be seen in Fig.1 that the first side lobes in the superimposition plot are about 35dB from their respective main lobes. This represent about a 10dB improvement from using the Bartlett window in terms of side lobe levels but without the loss in resolution.

As a representation of a GPR system, measured data was taken by setting up a vector network analyzer with horn antennas on both input and output ports. Two metal targets were then placed within a space approximately $0.25m^3$ bounded by RF absorbing material. The forward frequency response then measured the bistatic reflection of the metal targets over the frequency range 8GHz to 12.5GHz. The Inverse Fourier Transform (IFFT) using 4096 points was then used to calculate the corresponding impulse response and hence target position.

Fig.2 shows the results of the IFFT impulse response, the superimposition technique impulse response and a Bartlett windowed version of the impulse response. Both the superimposition and window techniques show considerable side lobe reduction from the using the IFFT alone. Again the superimposition technique maintains a resolution similar to that of the original IFFT

impulse response whereas the Bartlett windowed version suffers from a loss in resolution. Also the pulse position on the windowed version is shifted from its original position in the IFFT impulse response, leading to false identification of target position, which is not the case in the superimposition impulse response.

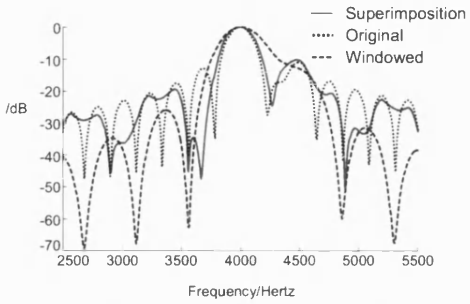

Fig. 1.FFT Spectra of Simulated Data

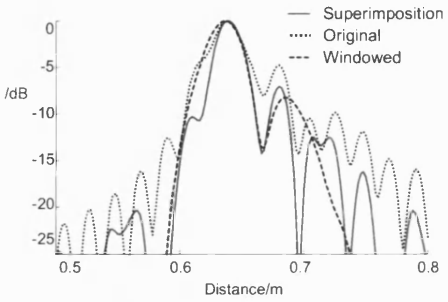

Fig. 2 IFFT Impulse Responses of Measured Data

Conclusion

A signal processing technique for improving FFT based analysis has been presented. The technique is based on superimposing multiple FFT analyses of the same signal followed by averaging. Applying the technique to simulated and measured data has shown minimal resolution loss, significant side lobe reduction and no distortion of peak positions from the original spectrum.

References:

[1] Daniels, D. J.: Surface Penetrating Radar (IEE Radar, Sonar, Navigation and Avionics, 1996)

[2] Porat ,B.: A Course in Digital Signal Processing (John Wiley and Sons, 1996)

11th International Conference on Ground Penetrating Radar, June 19-22, 2006, Columbus Ohio, USA

Detection and Resolution Enhancement of Closely Spaced Targets in Ground Penetrating Radar

Aminu W. Maida, Stephen R. Pennock, and Peter R. Shepherd
Dep't of Electrical and Electronic Engineering, University of Bath.
Bath, UK.
A.W.Maida@bath.ac.uk, S.R.Pennock@bath.ac.uk, P.R.Shepherd@bath.ac.uk

Abstract - **This paper deals with the signal analysis problems encountered with Frequency Modulated Ground Penetrating Radar (GPR) systems that use signal processing based on the Fast Fourier Transform (FFT). A technique for improved signal analysis based on superimposing and averaging multiple FFT analyses from the same data is presented. The technique aims to improve FFT signal analysis by reducing side lobe levels without broadening the main lobes hence maintaining resolution. Results from applying the technique to simulated GPR data have shown the ability to detect targets otherwise undetectable through standard FFT analysis, at the same time providing significant side lobe reduction and minimal loss in resolution. Also the technique has been applied to experimental data from a representation of a GPR system and again showed improved target detection capabilities, minimal resolution loss, significant side lobe reduction and minimal error in position detection. The technique is also shown to have negligible computational requirements.**

I. INTRODUCTION

Ground Penetrating Radar (GPR) systems using a Frequency Modulated Continuous Waveform (FMCW) are often used for buried utility location [1]. The FMCW signal provides the necessary bandwidth to distinguish the normally closely located buried utility lines. However the use of high frequency signals in GPR systems is often restricted by the depth resolution requirements of the system [2, 3]. In media such as soils, signal attenuation tends to be high and increases rapidly with frequency [4, 5] hence limiting the depth of signal penetration. In most cases utility lines are buried within a metre or two of the ground which is normally still within the penetration limits of an FMCW signal.

Typically FMCW radar systems rely on the Fast Fourier Transform (FFT) for signal analysis [2, 6]. The FFT while computationally efficient does present some challenges. Firstly the resolution of the FFT spectrum of a given signal is controlled by the frequency the signal was sampled at and the duration of the signal. Also there is the problem of spectral leakage which introduces error in both the frequency amplitude and positions. The affected frequency components, rather than appearing as sharp lines at their true frequencies, appear as a spectrum of frequencies around the true frequency positions. These effects tend to be worst when detecting weak frequency components in the presence of a nearby stronger frequency component. The combination of high frequency dependent attenuation in soils and spectral leakage could result in a situation whereby components related to a strong target masks a nearby weaker target or appears as a false target.

In cases where the signal sampling frequency or duration cannot be changed to improve FFT resolution, zero padding [7] can be applied to match the signal duration to the FFT resolution, whereas effects of spectral leakage can be reduced to an extent by applying window functions (or apodization functions) [8]. However the use of window functions comes at the expense of an increased main lobe width, therefore degrading resolution capability and introducing error.

In this paper we propose a technique for side lobe reduction and improving resolution of frequencies in an FFT spectrum, particularly those of closely located and unequal strength signals. The technique is based on superimposing multiple FFT analyses of the same data followed by averaging. A variation of the technique also sees the use of window functions to further suppress side lobes.

Although more complex high resolution techniques based on Eigen analysis e.g. MUSIC [9] and parametric modelling e.g. bandwidth extrapolation [10] provide better resolution than the FFT such methods are generally not suitable for GPR signal analysis. In the case of the MUSIC algorithm it requires supervision in the form of an estimate of the number of targets present to separate the noise subspace from the signal subspace which makes it suitable for situations where the noise levels and the levels of the wanted frequencies are sufficiently separate. GPR signals tend to contain high levels of clutter of sometimes the same order of magnitude as the targets and due to high attenuation rates in soils, even closely located targets could differ significantly in strength, which makes the

MUSIC algorithm less suitable for GPR signal processing. For parametric modelling based spectral estimation, an optimal number of model coefficients have to be chosen as too few could result in a poor spectrum and too many could lead to instability and false peaks [11].The techniques proposed in this paper require no form of supervision or modelling, the increase in complexity only comes from an increase in the number of FFT calculations and array multiplications.

II. PROPOSED TECHNIQUE

2.1 Side lobes in an FFT Spectrum

Figure 1 shows the FFT magnitude spectrum of 2 signals of the same frequency but different durations.

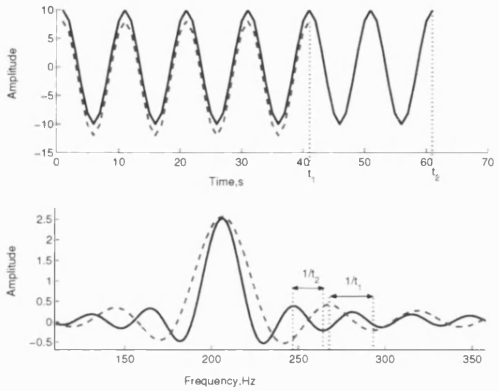

Figure 1. FFT Magnitude Spectrum of Signals of Same Frequency but with Different Durations

The main lobe position is always determined by the signal frequency whereas the width of the main lobe and hence positions of the side lobes are determined by t_i i =1, 2; the duration of the signal. The side lobes occur at intervals of $1/t_i$, from the centre of the main lobe, meaning that by altering the duration of the signals the positioning zero crossings in the spectrum could be controlled without altering the position of the main lobe. The dependence of the positioning of the zero crossings in an FFT spectrum on signal duration forms the basis of the signal processing technique proposed in the paper.

2.2 Algorithm

The technique we propose involves breaking successive side lobes in the FFT spectrum of the original signal into equal duration side lobes by superimposing the FFT spectrum of the original signal with FFT spectra of the same signal but with different main lobe widths.

For a sine wave of finite duration, τ_0 and frequency ω_0 (1), its corresponding Fourier Transform is a Sinc(x) function (Sin [πx]/ πx) described by (2)

$$s_0(t) = A\sin(\omega_0 t)\times rect\left\{\frac{t}{\tau_0}-\frac{\tau_0}{2}\right\} \tag{1}$$

$$S(\omega) = \exp(-j\omega\tau_0)\frac{A\tau_0}{2}\left[Sinc\left(\frac{\omega+\omega_0}{2\pi}\tau_0\right)+Sinc\left(\frac{\omega-\omega_0}{2\pi}\tau_0\right)\right] \tag{2}$$

The signal duration is chosen such that the zero crossings of the main lobe coincide with the midpoint of the side lobe being targeted.

The increased width main lobe spectrum can be derived from either truncating the original data, applying a window function to the original data or a combination of both truncation and windowing. To target the i^{th} side lobe using truncation, the fraction of the original data used is

$$k_i = \frac{2}{2i+1} \tag{3}$$

Applying a window function prior to FFT calculation will stretch the spectrum's main lobe by a factor of 2 [12]; therefore allowing a smaller truncation ratio to be used to achieve the same effect but with less of the original data discarded. Also there is the additional benefit of side lobe suppression provided by the window function. To target the i^{th} side lobe using the combination of windowing and truncation the data is truncated (before applying the window function) by

$$k_i = \frac{4}{2i+1} \tag{4}$$

The next step in the algorithm is to superimpose the resulting spectra followed by averaging over the width of two resulting side lobes i.e. $2/\tau_0$. Successive side lobes in the resulting superimposed spectrum will have a phase pattern of ρ, $\rho + \pi$, ρ, $\rho + \pi$, ρ and so on where ρ is the first order linear equation:

$$\rho(\omega) = -\omega\tau_i \tag{5}$$

Hence averaging over the width of 2 side lobes of the resulting superimposed spectrum will have a cancellation effect over the side lobes with minimal distortion to the main lobe.

Equations (6) to (11) describe the signal processing steps. The first step is to truncate/window the data as required (shown in (6)) and calculate the spectrum of each of the data sets (shown in (7)). This is followed by superimposing the spectrums as described by (8) . Equation (9) describes the normalisation of the resulting superimposed spectrum which is required so as to remove the complex scaling factors, exp($-j\omega\tau_i$) introduced by the Fourier transform process in (7) and to maintain relative magnitudes between frequency components with unequal strengths after superimposi-

tion. Finally the averaging is done via convolution as described by (10) using the filter described by (11). The processing technique described is linear; therefore using linear superimposition the technique can be applied to a multi-frequency signal.

$$s_i(t) = s_0(t) \times rect\left\{\frac{t}{\tau_i} - \frac{\tau_i}{2}\right\} \quad (6)$$

Where $\tau_i = k_i \tau_0$, k_i is either (3) or (4) and $s_o(t)$ is (1)

$$S_i(\omega) = \exp(-j\omega\tau_i)\frac{A\tau_i}{2}\left[Sinc\left(\frac{\omega+\omega_0}{2\pi}\tau_i\right) + Sinc\left(\frac{\omega-\omega_0}{2\pi}\tau_i\right)\right] \quad (7)$$

$$S'(\omega) = \prod_{i=0}^{n} S_i(\omega) \quad (8)$$

Where n is the index for the spectra of the truncated data sets with $n = 0$ representing the spectrum of the original signal.

$$S''(\omega) = \sqrt[n]{|S'(\omega)|} \times \exp\{j \times \angle S'(\omega)\} \times \prod_{i=0}^{n} \frac{1}{\tau_i} \exp(j\omega\tau_i) \quad (9)$$

$$S'''(\omega) = S''(\omega) * G(\omega) \equiv \int_0^{\omega} S''(\varphi) G(\omega - \varphi)\, d\varphi \quad (10)$$

$$G(\omega) = \frac{1}{\tau_0} rect\{\omega\tau_0\} \quad (11)$$

In the next section we present the results of applying the technique, each result presented is made up of an Original trace which refers to data processing with just the FFT, the Superimposition trace which refers to data processing using the technique described in this section and the Windowed trace which refers to data processing with a window function applied prior to the FFT being applied.

III. RESULTS & DISCUSSION

Results of applying the technique to simulated data and measured data from a vector network analyser are presented. In all cases unless mentioned, the first three side lobes from the main lobe were targeted, requiring 3 truncated/windowed versions of the original data. Also in all cases a 4096 point FFT/IFFT was used. Table 1 shows details of the truncation/windowing used to target the first three side lobes. The results are also compared to results of FFT processing in conjunction with windowing.

Table 1. Data Truncation Ratios and Type of Window used to Target Side lobes

Targeted side lobe	Truncation ratio	Window used
1st	2/3	None
2nd	4/5	Hann Window
3rd	4/7	Hann window

3.1 Simulation Results

The simulated data is for an FMCW GPR beat spectrum. The first simulation case represents a situation where there are two targets of unequal strengths, 20 and 1 relative to each other, at depths of 0.5m and 0.5375m giving beat frequencies of 4 kHz and 4.3 kHz. Figure 2 shows the results of the superimposition technique spectrum being compared to a Hann windowed [8] version of the signal spectrum. The FFT and Hann windowed spectra both fail to clearly detect the presence of 2 targets and so suffer from a clear loss in resolution, whereas the superimposition technique clearly identifies the two targets. It can also be seen in Figure 2 that the first side lobes in the superimposition plot are about 30 dB below their respective main lobes. This represents about a 15 dB improvement from using the original FFT spectrum

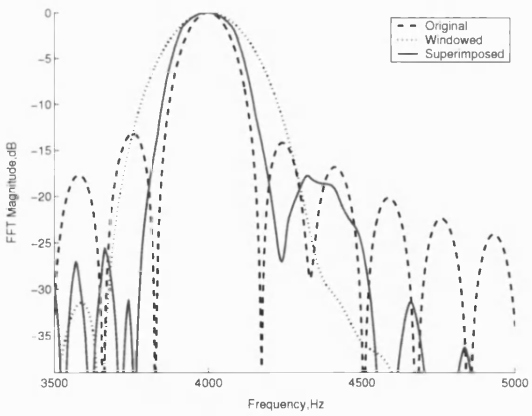

Figure 2. Beat Signal Spectrum for Simulation Case with 2 Closely Spaced Targets whose individual responses are centred at 4 kHz and 4.3 kHz

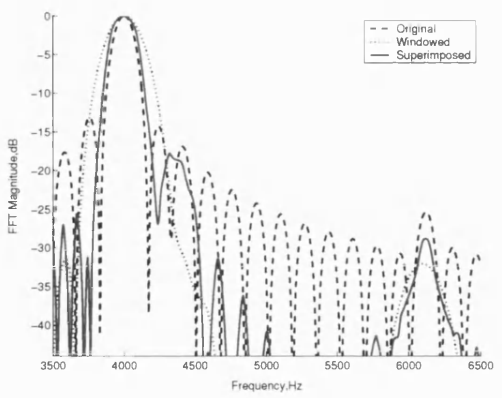

Figure 3. Beat Signal Spectrum for Simulation Case with 2 Closely Spaced Targets (4 kHz, 4.3 kHz) and a Deeper Weaker Target (6.1 kHz)

In Figure 3 we consider the case of the same 2 closely spaced targets and a deeper weaker single target with relative strength of 0.5 at a depth of 0.7625m giving a beat frequency of 6.1 kHz. Clearly windowing enhances the deeper target response but is failing to resolve apart the two closely spaced targets. Also even though the superimposition technique was set-up to optimise the performance around the first 3 side lobes, it still resolves all the 3 targets. Also, in not broadening the response from the deep target the accuracy of its position is not compromised.

3.2 Network Analyser Results

As a representation of a GPR system, measured data was taken by setting up a vector network analyser with horn antennas on both input and output ports. The forward frequency response then measured the bistatic reflection of the metal targets over the frequency range 8GHz to 12.5GHz. The Inverse Fourier Transform (IFFT) was then used to calculate the corresponding impulse response and hence target position. The distance shown in the results represents the total distance from the transmitter to the target and from the target back to the receiver.

Figure 5 shows the impulse response of an air filled 40mm plastic pipe as setup in Figure 4. In all cases two targets are resolved representing the front and back sides of the pipe with the superimposition technique providing the best resolution. Note in using the Hann window the apparent position of the targets is compromised. Figure 6 shows the impulse response of the same 40mm diameter plastic pipe (Figure 4) filled with water, it is now expected that the back side of the pipe will appear as a weaker target due to signal attenuation caused by the reflection losses at the air-water interfaces. The IFFT alone and applying windowing fails to resolve the two sides of the pipe whereas the superimposition technique clearly resolves the two sides of the pipe.

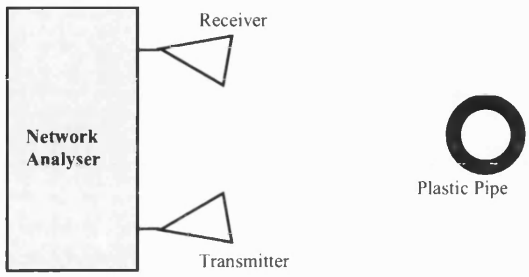

Figure 4 Measurement Setup with Plastic Pipe

Figure 8 shows the impulse response from the measurement setup in Figure 7 where a 10mm diameter cast iron rod is placed directly in front of a 40mm diameter air filled plastic pipe. The impulse response should indicate the presence of 3 targets due to the reflection off the cast iron rod and two reflections from the front and back sides of the pipe. However only the presence of the cast iron rod is clearly indicated with a single strong peak with the high lobes around the strong peak suggesting the presence of other targets. As shown in Figure 8 applying windowing degrades resolution and appears to have merged the smaller lobes into a single target, whereas applying the superimposition techniques clearly resolves the 3 targets as expected.

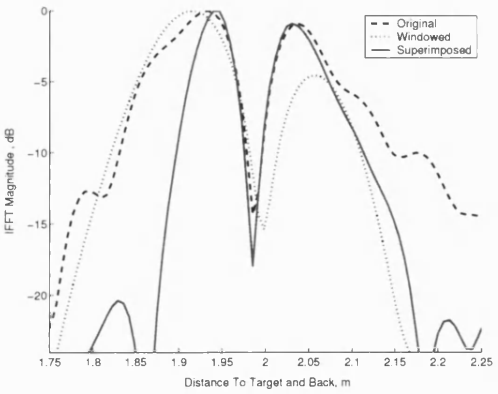

Figure 5 IFFT Impulse Response of Bistatic Reflection off Air Filled Plastic Pipe in Figure 4

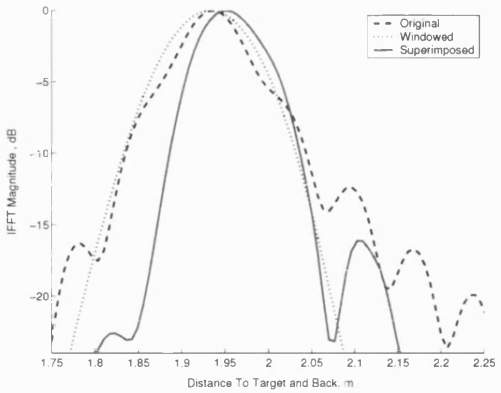

Figure 6 IFFT Impulse Response of Bistatic Reflection off Water Filled Plastic Pipe in Figure 4

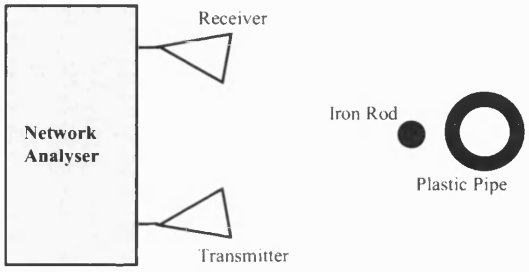

Figure 7 Measurement Setup with an Iron Rod in front of a Plastic Pipe

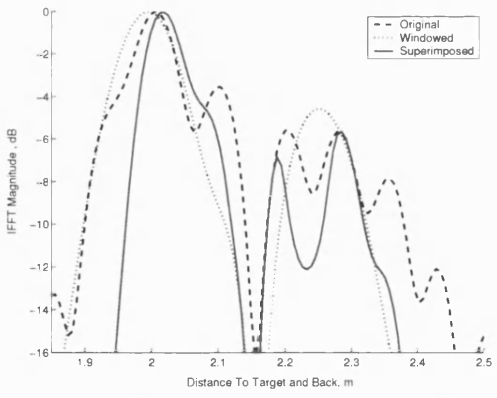

Figure 8 IFFT Impulse Response of Bistatic Reflection off Cast Iron Rod and Air Filled Plastic Pipe in Figure 7

3.3 Complexity

Table 2. Operations and Timing Values for Superimposition Technique

Targeted side lobes	No of FFT operations	No of Array Multiplications	Average run time(ms)
FFT only	1	0	0.85
1st only	5	1	4.2
1st & 2nd	6	2	5
1st, 2nd & 3rd	7	3	6.1

The technique presented requires no form of special hardware or computation as it makes use of standard FFT and filtering techniques. The increase in complexity comes from the increase in the number of FFT operations and array multiplications. Assuming the Filtering is carried out using an equivalent series of FFT/IFFT and array multiplications. When N Side lobes are targeted the operations required are as follows:

- N +1 FFT operations
- N array multiplications for superimposition
- 2 FFT operations and 1 IFFT operation for averaging

Table 2 gives details of the required operations for a few variations of the technique as well as an idea of the average run times of the technique using a 4096 point FFT written in Matlab, run on an AMD Athlon 1.8 GHz Desktop PC with 512MB of RAM.

IV. CONCLUSION

A signal processing technique for improving FFT based analysis has been presented. The technique is based on superimposing multiple FFT analyses of the same signal followed by averaging.

Applying the technique to simulated data has shown significant side lobe reduction and the ability to detect a frequency component in the vicinity of a stronger frequency that could otherwise not be detected by the FFT alone or in conjunction with windowing. The simulation also showed that the technique maintains a resolution similar to that of the FFT. Applying the techniques to measured data again showed improved target detection capabilities, minimal resolution loss, significant side lobe reduction and minimal error in position detection.

In addition applying the technique to both simulated and measured data has shown a lesser loss in resolution than when a window function (or apodization

function) is used to suppress side lobes while achieving similar levels of side lobe reduction.

Also while the technique appears to take about 7 times longer to run (bearing in mind this is unoptimised software running on a desktop PC) when targeting 3 side lobes, the actual computation time of 6.1ms is still negligible.

ACKNOWLEDGEMENTS

The Authors would like to thank the Petroleum Technology Development Fund in Nigeria, for their continued sponsorship that has enabled this work to be carried out.

REFERENCES

[1] A. D. Olver and L. G. Cuthbert, "FMCW Radar for Hidden Object Detection," *IEE Proceedings-F Radar and Signal Processing*, vol. 135, pp. 354-361, 1988.

[2] D. J. Daniels, *Ground penetrating radar*, 2nd ed. London: Institution of Electrical Engineers, 2004.

[3] L. Lanbo and Z. Lieyuan, "GPR signal analysis: can we get deep-penetration and high-resolution simultaneously?," presented at Tenth International Conference on Ground Penetrating Radar, 2004.

[4] M. T. Hallikainen, F. T. Ulaby, M. C. Dobson, M. A. Elrayes, and L. K. Wu, "Microwave Dielectric Behavior of Wet Soil .1. Empirical-Models and Experimental-Observations," *IEEE Transactions on Geoscience and Remote Sensing*, vol. 23, pp. 25-34, 1985.

[5] S. Lambot, E. C. Slob, I. van den Bosch, B. Stockbroeckx, and M. Vanclooster, "Modeling of ground-penetrating Radar for accurate characterization of subsurface electric properties," *IEEE Transactions on Geoscience and Remote Sensing*, vol. 42, pp. 2555-2568, 2004.

[6] Y. Yamaguchi, M. Mitsumoto, M. Sengoku, and T. Abe, "Synthetic aperture FM-CW radar applied to the detection of objects buried in snowpack," *IEEE Transactions on Geoscience and Remote Sensing,* , vol. 32, pp. 11-18, 1994.

[7] J. A. Cadzow, *Foundations of digital signal processing and data analysis*. New York: Macmillan, 1987.

[8] F. J. Harris, "On the use of windows for harmonic analysis with the discrete Fourier transform," *Proceedings of the IEEE*, vol. 66, pp. 51-83, 1978.

[9] M. Bouchard, D. Gingras, Y. de Villers, and D. Potvin, "High Resolution Spectrum Estimation of FMCW Radar Signals," presented at IEEE Seventh Workshop on Statistical Signal and Array Processing, 1994.

[10] T. G. Moore, B. W. Zuerndorfer, and E. C. Burt, "Enhanced Imagery Using Spectral-Estimation-Based Techniques," *Lincoln Laboratory Journal*, vol. 10, pp. 171 - 186, 1997.

[11] K. M. M. Prabhu and K. B. Bagan, "Resolution capability of nonlinear spectral-estimation methods for short data lengths," *Radar and Signal Processing , IEE Proceedings F*, vol. 136, pp. 135-142, 1989.

[12] B. Porat, *A course in digital signal processing*. New York ; Chichester: John Wiley, 1997.